SPECTRAL MESH SEGMENTATION

by

Rong Liu

M. Sc., Beijing University of Aeronautics and Astronautics, 2003

B. Sc., Beijing University of Aeronautics and Astronautics, 2000

a Thesis submitted in partial fulfillment
of the requirements for the degree of
Doctor of Philosophy
in the School
of
Computing Science

APPROVAL

Name:	Rong Liu
Degree:	Doctor of Philosophy
Title of Thesis:	Spectral Mesh Segmentation
Examining Committee:	Dr. Arthur Kirkpatrick Chair

Dr. Hao Zhang, *Senior Supervisor*,
Assistant Professor, School of Computing Science
Simon Fraser University

Dr. Torsten Möller, *Supervisor*,
Associate Professor, School of Computing Science
Simon Fraser University

Dr. Ghassan Hamarneh, *Supervisor*,
Assistant Professor, School of Computing Science
Simon Fraser University

Dr. Mirza Beg, *SFU Examiner*,
Assistant Professor, School of Engineering Science
Simon Fraser University

Dr. Karan Singh, *External Examiner*,
Associate Professor, Department of Computer Science, University of Toronto

Date Approved: March 20, 2009

Abstract

Polygonal meshes are ubiquitous in geometric modeling. They are widely used in many applications, such as computer games, computer-aided design, animation, and visualization. One of the important problems in mesh processing and analysis is segmentation, where the goal is to partition a mesh into segments to suit the particular application at hand. In this thesis we study structural-level mesh segmentation, which seeks to decompose a given 3D shape into parts according to human intuition. We take the spectral approach to mesh segmentation. In essence, we encode the domain knowledge of our problems into appropriately-defined matrices and use their eigen-structures to derive optimal low-dimensional Euclidean embeddings to facilitate geometric analysis. In order to build the domain knowledge suitable for structural-level segmentation, we develop a surface metric which captures part information through a volumetric consideration. With such a part-aware metric, we design a spectral clustering algorithm to extract the parts of a mesh, essentially solving a global optimization problem approximately. The inherent complexity of this approach is reduced through subsampling, where the sampling scheme we employ is based on the part-aware metric and a practical sampling quality measure. Finally, we introduce a segmentability measure and a salience-driven line search to compute shape parts recursively. Such a combination further improves the autonomy and quality of our mesh segmentation algorithm.

Keywords: shape part; segmentation; spectral technique; salience

To my family

“Destiny is not a matter of chance,
it is a matter of choice;
it is not a thing to be waited for,
it is a thing to be achieved.”

— *William Jennings Bryan*

Acknowledgments

My deepest gratitude goes to my senior supervisor, Dr. Hao Zhang. It is he who introduced me to this field, and taught me every single ingredient about being a good researcher, from coming up with novel ideas all the way to writing good academic papers. Without his help and support, I would not have reached this step. What he has taught me through his everlasting enthusiasm and rigorous attitude in pursuing elegant solutions to challenging problems will continue to ever guide me in my future endeavors. I would also like to extend my sincere thanks to the Chair and my committee members, Dr. Kirkpatrick, Dr. Möller, Dr. Hamarneh, Dr. Beg, and Dr. Singh, who have read my thesis and given me invaluable suggestions for improving my thesis.

It is my great pleasure and honor to study in the GrUVi lab at Simon Fraser University, where I have learned tremendously from my fellow colleagues and the time spent with them is always enjoyable and fruitful. I can only name a few of them due to the limited space. Andrea is such a Matlab guru and he even insists his Matlab code renders better than my renderer programmed in C++ with OpenGL; Matt never lets me beat him easily at the foosball table unless he is drunk; I admire Oliver so much for his unparalleled resistance to bitterness as he never drinks regular coffee rather than espresso when we go to the café on campus in afternoons; Ramsay is so knowledgeable and he always gives insightful answers to my questions more than I asked for. I cherish the days I spent with all GrUVites.

I cannot thank my family enough for their unconditional support and endless love. My parents always stand beside me; in their mind, I would probably never grow up. I got to know my wife nineteen years ago when we were secondary school classmates. I still remember the first time we talked to each other in vivid detail, and our little Brice is already two years and three months old now. What a wonderful journey! All of you have defined my life and this thesis is dedicated to you.

Contents

List of Figures

Chapter 1

Introduction

With the rapid advances in computer hardware and geometry acquisition devices, meshes, as a means to represent 3D surface shapes, are becoming ubiquitous in computer graphics. Accordingly, mesh processing and analysis has become an important research field. As image segmentation is to image analysis, mesh segmentation is of primary importance to numerous applications in mesh processing and analysis. In fact, segmentation itself has been intensively studied as an important operation for generic data analysis. The goal of segmentation is to identify from a given data set homogeneous groups with similar characteristics to facilitate solving the problem at hand. We will see that mesh segmentation can operate at three different conceptual levels, and the characteristics of the resulting segments at each level are also application-dependent.

Mesh segmentation has received a great deal of attention in recent years. However, the research work involved in this topic is still far from mature (the first survey paper by Shamir [111] emerged in 2006), especially when the segmentation comes to extract higher order information from a given shape. In this thesis, we work on a particular mesh segmentation problem, which is to decompose a mesh shape into its constituent parts that are intuitive to human beings.

1.1 Mesh Segmentation

1.1.1 Problem Definition

We work on triangle meshes in this thesis. According to the definition by Praun et al. [101], a triangle mesh $\mathcal{M}$ is a pair $(\mathcal{T}, \mathcal{K})$. $\mathcal{T}$ is a set of t point positions, i.e., $\mathcal{T} = \{v_i \in \mathbb{R}^3 \mid 1 \leq i \leq t\}$, and $\mathcal{K}$ is an abstract simplicial complex that contains all the topological (adjacency) information. The complex $\mathcal{K}$ is a set of subsets of $\{1, \ldots, t\}$. These subsets come in three types: vertices $\{i\}$, edges $\{i, j\}$, and faces $\{i, j, k\}$, which are referred to as mesh primitives. We denote the sets of vertices, edges, and faces of $\mathcal{M}$ by $\mathcal{V}$, $\mathcal{E}$, and $\mathcal{F}$, respectively. In Figure 1.1(a), a triangle mesh representing a hand is shown.

With $\mathcal{M}^{\mathcal{P}}$ being one of the mesh primitive sets ($\mathcal{V}$, $\mathcal{E}$, or $\mathcal{F}$), mesh segmentation can be viewed as an operation

$$\mathcal{M}^{\mathcal{P}} \mapsto \{\mathcal{M}_1^{\mathcal{P}}, \mathcal{M}_2^{\mathcal{P}}, ..., \mathcal{M}_k^{\mathcal{P}}\},$$

where $\bigcup_{i=1}^{k} \mathcal{M}_i^{\mathcal{P}} = \mathcal{M}^{\mathcal{P}}$ and $\mathcal{M}_i^{\mathcal{P}} \bigcap \mathcal{M}_{j,j \neq i}^{\mathcal{P}} = \emptyset$. In practice, it is common to segment by faces since faces provide a natural watertight coverage to a mesh surface. It is worth mentioning that typical applications would require that primitives in each subset $\mathcal{M}_i^{\mathcal{P}}$ form a single connected region on the mesh surface. Note also that the segmentation mentioned above is applied to the surface of a mesh. It is possible to apply segmentation to the volume enclosed by a mesh as well. For example, the works in [79, 130] compute a set of simple solids, i.e., solid ellipsoids, as an alternative to the original mesh volume. Although these solids may overlap, their union approximates the mesh volume well. This is in particular useful for applications involving geometry queries, such as collision detection. In our work, however, we are only interested in surface segmentation.

Mesh segmentation can operate at three different conceptual levels: *geometric level*, *structural level*, and *functional level*, as illustrated in Figure 1.1(b, c, d). The segments generated at the latter levels reveal higher order abstraction of shapes. The first two levels are purely based on the geometry of an input shape, while function-level segmentation requires prior knowledge to understand the object represented by a shape. For geometric-level and structural-level segmentations, a similar classification is previously made by Shamir [111] as surface-type and part-type segmentations, respectively. We discuss each segmentation level in the following.

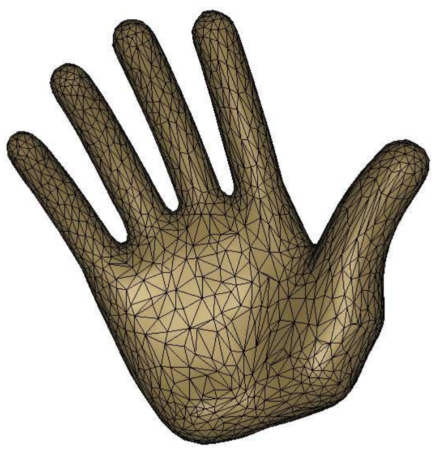

(a) triangle mesh of a hand model

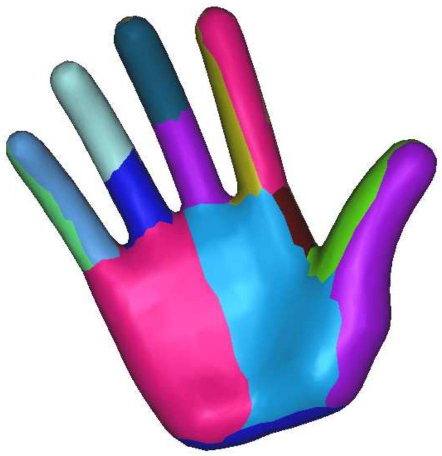

(b) geometric-level

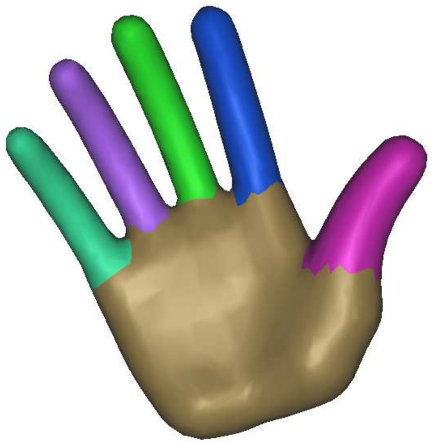

(c) structural-level

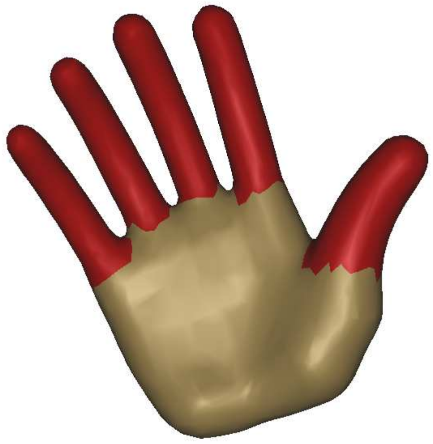

(d) functional-level

Figure 1.1: A triangle mesh of a hand model (a) and its segmentations at three levels: geometric-level segmentation (b) with each patch being nearly planar and as compact as possible; structural-level segmentation (c) that decomposes the shape into its constituent parts according to human intuition; and functional-level segmentation (d) that partitions the hand into two components — the fingers as a whole and the palm — with respect to the anatomical property of the hand.

1.1.2 Geometric-level Segmentation

Meshes are normally given with only geometry (vertex coordinates) and connectivity (face adjacency) information. At the geometric level, a shape is partitioned into segments that possess certain simple surface geometric properties, such as planarity [25] and convexity [23], or into segments that can be approximated by certain parametric surfaces, e.g. hyperbolic or parabolic surfaces. The segments do not necessarily correspond to the shape's constituent parts as higher order information; they are simply connected homogeneous regions with similar geometric properties. Geometric-level segmentation extracts the information of a shape at the lowest level.

Figure 1.1(b) shows a geometric-level segmentation result on the hand model. As we can see in this particular case, the segments are approximately planar patches that are compact and the structural information of the hand is not revealed properly.

1.1.3 Structural-level Segmentation

Similar to segmentation at the geometric level, structural-level segmentation is also purely geometry-based. However, structural-level segments reveal the structure of a given shape. As the structure of a shape is typically characterized by its constituent parts, segmentation at this level strives to decompose a shape into its parts. Note that our notion of parts is generic by referring to the meaningful components of a shape that are intuitive to human beings. Figure 1.1(c) exemplifies a segmentation on the hand model at structural level. Compared to geometric-level segments, the five fingers and the palm, which correspond to the intuitive parts of the hand, are obtained and the structure of the hand shape is revealed.

The concept of a part intuitive to human perception is by no means clearly defined. How humans perceive parts and how to measure the strength (salience) of parts have long been studied in psychology and cognition [50, 128]. Despite the absence of a clear definition for shape parts, the geometry processing community has adopted the *minima rule* [51] for part characterization:

> All negative minima of the principal curvatures (along their associated lines of curvature) form boundaries between parts.

The minima rule gives a constructive way to compute parts: mesh segmentation algorithms may delineate parts by explicitly forming their boundaries from surface regions with negative minimum principal curvatures [69, 76]. Alternatively, algorithms can also cluster mesh faces into groups by incorporating measures reflecting the minima rule implicitly via considerations of concavity [59]. Since a part is typically convex, it is possible to extract parts by fitting simple convex geometric primitives, e.g., ellipsoids and cylinders [119, 134], or by computing convex volumetric regions directly [6, 61]. In addition, techniques are also designed to find certain specific structures, such as tubular regions [43, 89].

It is worth emphasizing that when we say a part is intuitive to human perception at the structural level, we emphasize on the intuition based only on the geometry of a shape. Human intuition about a part could be affected by other higher order information of the object a shape represents; such parts are at the functional level which is described next. We are only interested in the structural-level segmentation in this thesis.

1.1.4 Functional-level Segmentation

At the structural level, it is the geometry of a shape that is recognized and the segments produced are in accordance with the shape's structure. Functional-level segmentation considers not only a shape itself, but also the object the shape represents. Note that we draw a clear distinction between an object and its shape. To apply function-level segmentation, an algorithm needs to understand the functional properties of an object, which in general are not encoded in the geometry, hence requiring prior knowledge. Segments produced at this level reflect the functional information of objects based on a specific application context.

Figure 1.1 (d) shows one possible functional segmentation of the hand model. The hand is divided into two segments, the five fingers as a whole and the palm. Obviously, the segmentation result in this case follows a functional abstraction of the hand, while the structural information of the hand shape is not respected. As another example of functional-level segmentation, one may see the engine body and the pipes attached to it under the hood of a car as a single intuitive part. We believe this intuition about a part, the entire engine, has a lot to do with the notion of an engine and how the engine is contrasted with its surroundings under the hood. For structural-level segmentation, however, we do not demand our algorithm to understand the pipes are sub-parts of the engine; instead, it is deemed appropriate to segment the engine into its main body and the pipes, since such a segmentation is natural based on the engine's shape only.

Clearly, functional-level mesh segmentation requires algorithms to understand the object behind an input mesh. This is possible by incorporating prior knowledge using a template or via training. Similar works for images have been studied, such as in template-based segmentation [16, 46, 85] and image labeling [49, 136]. However, to the best of our knowledge, such segmentation algorithms for meshes do not exist. This could be in part due to the lack of a systematic mesh database with segmentation information, which is necessary for training.

1.2 Applications

A common application of mesh segmentation is *parameterization*, which in turn is useful to many other applications [114], e.g., detail mapping, mesh editing, and remeshing. Take texture atlas generation as an example. Since it is in general impossible to parameterize a mesh surface onto an image plane without stretching, the problem is essentially how to minimize the stretching of a parameterization. To this end, a mesh surface is partitioned into approximately developable patches, which can be parameterized individually with less stretching. Developable surfaces have zero Gaussian curvature everywhere; typical examples include planes, cones, and cylinders. Segmentation for parameterization applications [56, 72, 107, 108, 121, 145] is at a geometric level in general.

Mesh segmentation is also commonly practiced in *reverse engineering*, where the goal is to recover the parametric surfaces from a digitalized shape. This is particularly useful for CAD models, as CAD software usually only deals with parametric surfaces. Primitive fitting [54] is a popular strategy for this purpose. Simari and Singh [119], and Wu and Kobbelt [134] utilize the variational approach [25] to approximate surfaces with planes, spheres, cylinders, rolling-ball blend patches, and ellipsoids. This approach is extended by Yan et al. [139] to incorporate general quadric surfaces. To speed up the processing, hierarchical primitive fitting is adopted by Attene et al. [4]. Except for primitive fitting, other techniques such as slippage [41] and curvature tensor analysis [68] are also utilized, based on the observation that surface patches with similar slippage or curvature tend to form a single parametric surface. Depending on the types of the fitting primitives, such segmentations may sit at a geometric or a structural level. For example, if ellipsoids are used, the resulting segments are likely to correspond to intuitive parts.

Animation makes use of mesh segmentation as an important auxiliary operation as well. In order to generate a high quality deformation sequence of an articulated shape, it is beneficial to represent the shape via its skeleton, because the skeleton can be animated easily and the surface is then reconstructed from the deformed skeleton. Due to the strong connection between the parts of a shape and its skeleton, quite a few skeletonization algorithms [59, 76, 110] are segmentation-based. Once the parts of an articulated shape are segmented out, skeletons can be readily constructed from these parts. Another example where mesh segmentation comes handy is *morphing* [116, 148]. To enhance the quality of morphing, both the source mesh and the target mesh are segmented into compatible parts, and morphing is carried out between the matched pairs. Collision detection, a necessary operation in a number of applications including *gaming* and *physical simulation*, could also benefit from mesh segmentation. As shown in [40, 74], meaningful segments would help build a well structured hierarchical bounding volume tree that is crucial to the efficiency of collision detection. As the above applications usually need to have the resulting segments reflect the structure of a shape, these segmentations are at a structural level.

Mesh coding is another area where segmentation is useful, from several aspects. From the computational complexity perspective, partitioning a surface into segments helps reduce the overhead in a divide-and-conquer manner. In the work by Karni and Gotsman [58], a surface is decomposed into multiple patches and encoded separately, avoiding the eigenvalue decomposition of an otherwise large matrix. Coding mesh patches separately is also error-resilient and space-efficient; Yan et al. [140] show that carefully designed segmentation algorithms are capable of producing patches suitable for efficient coding and robust against patch corruption. To further optimize the transmission over a bandwidth-limited channel, e.g., wireless network, mesh patches are deliberately constructed in the coding stage. During transmission, only the patches visible to end users are transmitted or transmitted with higher priority. The experiments in [45, 141] attest to the effectiveness of this strategy. Different from the above works, time-dependent geometry coding is studied by Lengyel [71], in which mesh vertices are clustered into groups with similar trajectories along the time axis so that they can be encoded in a local coordinate system. Segmentations are all at a geometric-level for these applications except for the last one, in which the mesh vertices with similar trajectories often form a rigid structural part of a shape.

Last but not least, mesh segmentation also plays an important role in *shape modeling* and *shape recognition*. One example shape modeling task is to model objects by parts. The observation herein is that objects can be classified into categories with similar part structures; therefore similar parts can be reused to allow for efficient reconstruction of new models with high details. In order to obtain reusable parts from shapes, both semi-automatic [39, 55] and automatic [61] segmentation techniques are proposed. Shape recognition is a hard problem in general. As lower geometric information, e.g., curvatures, is not sufficient to manifest higher order semantic information about a shape, higher level information needs to be extracted to recognize the shape better. To this end, algorithms often make use of the parts of a shape and their topological relations. Such an example is from shape retrieval [31, 110, 148], in which the signature of a shape is calculated based on the features and the relations between its structural parts. In fact, researches in psychology and cognition [15, 50, 51] have long shown that shape parts have a profound impact on the way human beings recognize and understand shapes. Although related studies on this topic are primarily cast on image data [2, 57, 62, 67, 105, 117], 3D shape representation with structural information and its application has received much attention [1]. We believe mesh segmentation is indeed an indispensable ingredient in this promising area and deserves long-term study.

1.3 Contributions

The difficulty of structural-level segmentation lies in the fact that the notion of parts in a shape is not well-defined. In this thesis, we propose several ideas to address this problem. Some of these ideas, including the part-aware metric, segmentability, and salience-driven cut search, not only lead to quantitative measures for characterizing parts, but also suggest constructive means to compute them. Our algorithms have been demonstrated to produce high quality segmentation results. We elaborate our contributions as follows.

A novel metric to capture part information In order to apply spectral clustering to mesh segmentation, we need a distance metric that is able to capture the part information of a shape. Designing a part-aware metric on mesh surfaces is non-trivial since the parts are yet to be found. In practice, one is supposed to utilize the metric to facilitate segmentation. Therefore, the realization of an effective metric should be conceptually simple, at least not more complicated than implementing a third party segmentation algorithm and using the resulting parts to help build the metric. We design such a metric based on the characteristics of how visible regions change for points within shapes and across part boundaries. To date, our metric is the only one that is specifically designed to capture part information. It is demonstrated to outperform existing metrics [30, 59, 66] that have been utilized for mesh segmentation. Note that our part-aware metric is also useful for a variety of other applications in geometry processing.

Application of spectral clustering to mesh segmentation We for the first time apply spectral clustering to mesh segmentation, effectively and efficiently. Spectral clustering is a popular clustering algorithm studied in machine learning. Resorting to the part-aware metric, we design yet another variant of spectral clustering for structural-level segmentation. To make our algorithm effective in practice, we address several problems of spectral clustering within the context of mesh segmentation. For efficiency, we make use of sub-sampling and the Nyström method [10] to reduce the complexity involved in pairwise distance computation and eigenvalue decomposition. We provide a geometric interpretation to the Nyström method and reach a measure for its approximation quality. From this, practical sampling schemes are suggested. Since our algorithm transforms the part-aware distances into an Euclidean embedding and finds an approximate solution to a global optimization problem, it is able to produce high quality segmentation results. This segmentation algorithm is efficient, operating in a k-way partition manner, where k is the number of segments input by users.

Segmentability- and salience-driven segmentation via spectral embedding We further improve our segmentation algorithm by enhancing its autonomy and quality. The improved algorithm segments through recursive 2-way cuts. The current mesh piece is only segmented when it has a sufficiently large *segmentability* score. The segmentability measure is derived by spectral-embedding a mesh piece into 2D, in which its part information is better revealed and readily quantified. Unlike the previous algorithm where users need to specify k for each input model, the improved algorithm enjoys a higher autonomy with a fixed segmentability threshold that is model-independent. Meanwhile, we apply salience to enhance segmentation quality. Salience is an important concept studied in psychology to measure the strength of a part and it is closely related to how humans perceive parts. Although salience has been previously used for mesh segmentation, it is only used in post-processing, probably due to the difficulty of incorporating it into the initial search for parts. We found a solution to this by carefully arranging mesh faces into a sequence which can be considered as derived through a 1D spectral embedding. Since the cut is only sought along the sequence, the search space for parts is substantially reduced. As a result, we can afford to integrate salience into the search procedure. As the face sequence preserves the meaningful cuts and salience is exploited early on, this algorithm achieves superior segmentation quality.

1.4 Thesis Organization

The reminder of the thesis is organized into six chapters. In Chapter 2, we review mesh segmentation techniques and spectral clustering. The part-aware metric is developed in Chapter 3. Using this metric, we design a k-way mesh segmentation algorithm using spectral clustering in Chapter 4. Chapter 5 studies and applies sub-sampling to this segmentation algorithm to reduce its complexity. Next, Chapter 6 improves upon the k-way segmentation algorithm via recursive 2-way cuts based on segmentability and salience. We conclude our work and point out future directions in Chapter 7.

Chapter 2

Background and Related Work

This chapter presents a review of the related literature. In order to understand mesh segmentation better, we first highlight certain differences between mesh segmentation and image segmentation in Section 2.1. After this, we review some existing mesh segmentation techniques in Section 2.2. Section 2.3 discusses spectral clustering briefly.

2.1 Mesh Segmentation vs. Image Segmentation

Segmentation has been studied extensively on image data. Image segmentation is of fundamental importance in many fields including computer vision, medical imaging, and video coding [3]. A tremendous amount of work has been conducted in the last several decades. A recent search in *EI Compendex* showed a total of 9154 records of papers with "image segmentation" in title from the year of 1970 to 2008. Before we discuss the differences between mesh segmentation and image segmentation, we briefly discuss image segmentation first. Interested readers are referred to the surveys in [47, 95, 99] for more details.

It is commonly practiced in computer vision to segment images along the boundaries of the objects in a scene. Boundaries between objects are often detected in regions with dramatic intensity changes, say by the Canny edge detector [20]. However, color images with abundant textures and patterns easily produce many spurious edges, which do not correspond to real object boundaries. To tackle this problem, statistical methods are applied to select only salient edges and connect them into continuous boundaries [103, 133]. Another approach to detecting meaningful boundaries is through supervised learning. Such an example is in [84], where the authors make use of ground truth images with manually-marked boundaries to train a classifier. Posterior probabilities of test image pixels on boundaries are calculated via the trained classifier. In addition, it is also possible to segment images via pixel grouping, where image pixels are clustered into regions directly without forming explicit boundaries. Both the spectral technique [115] and the statistical technique [127] fall into this category.

Image segmentation is also an indispensable step in medical image analysis. Before anatomical structures captured in images by, e.g., computer tomography (CT) and magnetic resonance imaging (MRI), can be analyzed, they must be segmented out from their surroundings. This is known as the delineation of anatomical structures. One popular technique for this is deformable models. Boundary-based deformable models [63, 86] use a parametric contour, which evolves on images to reduce its energy until a local minimum is reached. As an energy functional encodes the desired properties of both the contour and the target positions, the delineated boundary is often of higher quality. To better incorporate prior knowledge, template-based deformable models [16, 46, 85] are developed as an alternative. Template deformable models are programmed to assume the generic shape of the target structure, which amounts to encoding prior knowledge. Meanwhile, they are also allowed to deform moderately to accommodate the slight differences from multiple instances of the structure.

Mesh segmentation has certainly benefited from the research achievements of image segmentation. In fact, as one of the early mesh segmentation techniques, the watershed algorithm by Mangan and Whitaker [82] is extended from its counterpart in image segmentation. Meanwhile, mesh segmentation is also a quite different topic from image segmentation; their differences can be understood from several perspectives as follows.

In terms of the types of information contained in the data, images have intensity and spatial information. These two types of information are different stimuli to human perception and they play different roles in deriving segmentation results. Roughly speaking, an image segment is typically a spatially continuous region with similar intensities or patterns (textures) [8, 96]. For mesh segmentation, however, current research is only concerned with the shape of a mesh, i.e., a spatial information. Any other information, if any, such as color and texture, is discarded.

One may view a 2D image as a mesh by virtually lifting its pixels vertically, where the elevation of each pixel is determined by its intensity. However, unlike the pixels of an image, the vertices of a mesh have irregular connectivity in general. For this reason, meshes lack a global canonical parameterization. This may prevent certain useful techniques from being used for meshes, such as the Fourier Transform. Essentially, meshes are 2D manifolds embedded in 3D and their dimensionality is atypical.

Mesh segmentation is a relatively new research topic in contrast to image segmentation. Due to their differences, techniques for image segmentation cannot be trivially extended to mesh segmentation. So far, mesh segmentation has not seen the use of certain advanced techniques, including supervised clustering. This is in part due to the absence of a systematic mesh database with segmentation information for training purposes.

2.2 Segmentation Techniques

Mesh segmentation algorithms can be categorized via many criteria. In this section, we review some existing algorithms based on their characteristics and how much user intervention they require.

2.2.1 Bottom-up and Top-down

If a mesh segmentation algorithm seeks segments using global information, e.g., by computing a (approximate) solution to a global optimization problem, we call it top-down. On the other hand, if an algorithm finds segments using only local information, e.g., via a greedy approach, we call it bottom-up. In the bottom-up category, final segments are typically formed by grouping smaller ones, for example, starting from individual faces. The segmentation procedure is often guided by a cost function, which is minimized locally in a greedy manner. Bottom-up approaches are usually efficient. However, they are subject to local minima and over-segmentation. Top-down approaches address these problems by working in the opposite direction: segments are obtained by decomposing a mesh into pieces, through either a simultaneous k-way cut, or a sequence of cuts (typically 2-way cut) in a hierarchical manner. Since top-down approaches optimize segmentation using more global information than bottom-up approaches, they tend to achieve better results, but usually with a higher computational cost.

Bottom-up and top-down only roughly characterize the properties of existing mesh segmentation techniques. In the following, we further split them into seven sub-categories and discuss their characteristics, pros, and cons briefly. Note that the categorization is neither perfectly disjoint nor complete; we only investigate some popular techniques and try to classify them according to their most prominent characteristics. Readers are referred to [5, 111] for more detailed coverage.

Region growing is a bottom-up approach, in which a segment is formed by growing a continuous surface region until the regulatory constraints fail. In *sequential* region growing [68, 82, 102, 146, 147, 148], the next region starts to grow after the previous one cannot grow any more. This process iterates until the entire surface is covered. In *simultaneous* region growing [55, 72, 94, 137, 144], multiple regions are seeded and grown simultaneously: the immediate region to grow is always the one with the smallest growing cost. The asymptotic complexity for sequential growing is typically $O(n)$ (n is the face count) since each mesh face is visited only once, while simultaneous growing usually sees a complexity of $O(n \log n)$ due to the maintenance of a global priority queue. At a higher complexity, simultaneous growing often offers better segmentation quality because of its fine-tuned growing order with smaller granularity. Region growing methods are fast and the framework is generic. By applying different growing constraints, region growing methods are capable of achieving both geometric-level and structural-level segmentations. As bottom-up approaches, however, region growing methods are susceptible to local minima.

Region merging methods [4, 40, 41, 113] start out by partitioning an entire mesh surface into patches, each typically containing a single face initially, and recursively merge neighboring patches. Similar to simultaneous region growing, the merging order is also guided by a priority queue. As an example, Garland et al. [40] combine three error metrics to prioritize all current possible merges, ensuring that each resulting segment is compact, nearly planar, and has consistent face normals. It is worth mentioning one recent work [6] based on region merging for computing convex parts, which works on volumes rather than on surfaces. The algorithm decomposes the volume enclosed by a mesh into tetrahedra; neighboring solids (initially consisting of a single tetrahedron) are then merged recursively. Unlike surface-based convexity measures, the convexity measure for solids enjoys higher accuracy. The most significant advantage of the region merging framework is its ability to create a segmentation hierarchy and this is important to applications involving spatial queries. Region merging is also bottom-up, and its small merging cardinality, usually 2 (merging only two adjacent patches each time), may deteriorate the segmentation quality.

Variational approaches [25, 56, 59, 61, 65, 98, 116, 119, 134, 139] are probably the most popular technique for mesh segmentation, which essentially solve the K-means clustering problem [80] using Lloyd's algorithm [78]. In short, Lloyd's algorithm finds an approximation (a local minimum) to the global optimal solution by alternating two operations, element assignment and proxy fitting, until convergence. In the element assignment operation each mesh face is assigned to the cluster whose proxy is closest to this face; in the proxy fitting operation each proxy is refined to better fit, according to a chosen metric, the member faces of its associated cluster. For example, if the goal is to partition a surface into planar patches, a proxy should be the best fitting plane of its cluster. In practice, proxies often converge with high rate. A variational method is top-down as all clustering elements are examined simultaneously to optimize for a cost function. However, k, the number of desired segments is non-trivial to infer from input data and is usually given by users.

Boundary formation [69, 75, 92] methods seek to delineate segments explicitly with their boundaries. In contrast, techniques mentioned above all construct segments by grouping mesh primitives. A segment boundary is a closed contour typically formed by a sequence of mesh edges. Such contours are either formed by connecting broken feature lines from concave regions as in [69, 92] or computed as a graph cycle with minimum weight as in [75]. Boundary formation methods are top-down. As segment boundaries are formed explicitly, it is easier to make them clean and smooth. Due to the obliviousness to the interior of the resulting segments, however, boundary formation approaches have only been used for structural-level segmentation. In addition, this method is subject to featureless regions where intuitive part boundaries are supposed to cross. Completing broken contours through such regions is challenging.

Statistical approaches [30, 42, 64] are gaining increasing attention recently. Lai et al. [64] model the distance between faces using random walks. Each edge of a triangle face is associated with a probability describing how likely a random walk moves across this edge to the neighboring face. The algorithm allows users select to (or automatically select) several seed faces to represent the desirable parts of an input mesh. Each face is clustered into the part of a seed face if a random walk starting from the face has the highest probability of reaching this seed face. The whole modeling process is reduced to solving a sparse linear system. For structural-level segmentation, the probabilities assigned to edges are related to local concavities. The algorithm proposed by de Goes et al. [30] is in the same vein, by modeling diffusion distance on surfaces. Golovinskiy and Funkhouser propose a randomized approach [42]. Roughly speaking, the idea is to apply several popular segmentation algorithms with different or random initial settings for a large number of times. Each particular execution produces a set of boundary edges. With the results from all executions, the algorithm computes a probability of each edge being on a part boundary. A concrete segmentation is computed based on such probabilities. Statistical approaches, especially the first two algorithms based on random walks and diffusion distance, are in general top-down techniques. Also they have been empirically shown to be robust against noise. Statistical approaches are so far only applied to structural-level segmentation.

Topology-driven approaches [7, 74, 104, 126, 135] are top-down segmentation techniques, which utilize shape skeletons. Note that the skeleton herein refers to a 1D curve that roughly lies inside a shape and reflects its structure. Shape skeletons are suggestive of shape parts. Think of an articulated shape, such as a human being, whose skeleton can be divided into sections at the critical points, e.g., branch points, with resulting sections corresponding to the intuitive parts, i.e., torso, limbs, and head. That being said, topology-driven approaches are in general divided into three steps: extract skeleton, identify critical points, and associate skeleton sections with shape parts. Since the topology of the skeleton is pose-invariant to the articulation of a shape, topology-driven approaches are invariant to poses. However, robust skeleton extraction and critical points identification are both non-trivial. Meanwhile, only structural-level segmentation is possible through this technique.

Symmetry-driven approaches are based on the observation that both natural and man-made objects are usually symmetric to a certain degree [73], either globally or partially. It is then rational to exploit symmetry information for segmentation. Simari et al. [118] propose to partition a mesh iteratively using weighted principal component analysis to find extrinsic reflectional symmetries. In each iteration, a subregion of the current mesh piece is extracted and partitioned into two by a plane if the subregion is symmetric with respect to the plane. Podolak et al. [100] introduce Planar-Reflective Symmetry Transform to compute major local symmetric planes of a shape and such planes are used to simultaneously segment the shape into self-symmetric parts. Different from the above two algorithms, Mitra et al. [87] detect surface regions that are invariant up to rigid transformations and scaling. This is achieved through a voting scheme in a transformation space. Symmetry-driven segmentation is useful to many applications, including mesh coding, shape retrieval, and

Technique	Strategies	Level	Pros / Cons
Region Growing	B	G, S	efficient, generic / prone to local optimum
Region Merging	B	G, S	hierarchical result / prone to local optimum
Variational Approach	T	G, S	better approximation to global optimum / unknown number of clusters
Boundary Formation	T	S	clean and smooth boundary / challenging to complete broken boundaries over featureless regions
Statistical Approach	T	S	mathematically sound, resistant to noise / unknown number of clusters
Topology-driven Approach	T	S	pose-invariance / non-trivial skeleton extraction and critical points identification
Symmetry-driven Approach	T	S	informative segments / only extrinsic symmetry so far, not necessarily structural parts

Figure 2.1: Highlights of various segmentation algorithms. B: bottom-up, T: top-down, G: geometric-level, S: structural-level.

remeshing. The segments obtained by symmetry-driven approaches are typically informative about the structure of a shape. However, depending on a shape's symmetry structure, such segments may not necessarily correspond to the intuitive parts of the shape as in the structural-level segmentation. In addition, current symmetry-driven approaches handle only extrinsic symmetries, but not intrinsic ones. For example, a bent left arm would not be considered symmetric with respect to a straight right arm.

Figure 2.1 highlights the properties of the segmentation algorithms mentioned above.

2.2.2 User Intervention

We can also classify mesh segmentation algorithms based on the degree of user intervention. In this thesis, we adopt three classes: *automatic*, *semi-automatic*, and *manual*.

In our classification, an automatic segmentation algorithm simply needs users to feed a mesh and the segments are produced automatically. Note that we do allow automatic algorithms to have free parameters, such as threshold values. Users can fine-tune these parameters in order to suit different input models. We consider parameter setting as a robustness issue, rather than an autonomy issue. We mention one special parameter, the number of segments. The number of segments is directly related to segmentation output and it is highly model-dependent. The variational approaches mentioned above are good examples where the number of segments is needed. Of course, it is ideal to have an automatic algorithm perform robustly on all kinds of meshes with a fixed set of parameters. Unfortunately, this is difficult, especially for the structural-level segmentation. The majority of the available mesh segmentation algorithms, e.g., [40, 61, 76, 82, 93], are automatic.

For semi-automatic algorithms [55, 144], users are usually required to provide direct assistance for segmentation, such as drawing sketches on a mesh to indicate desired segments. Take the work by Ji et al. [55] for example. Users must first provide one stroke on the background part and the other on the foreground part of a given mesh. Then a region growing approach is executed to identify the two corresponding parts, as in an automatic algorithm. In order to achieve better segmentation results, users may want to make the two strokes longer and place them in parallel to the desired boundary. The algorithm developed by Lee et al. [69] also allows for direct user assistance. Semi-automatic algorithms strike the balance between autonomy and user assistance. They are in general capable of obtaining higher segmentation quality than automatic algorithms.

If an algorithm requires a significant amount of segmentation information from users, we consider it manual. For example, users may be asked to sketch the boundaries between all desirable segments, while the algorithm only helps connect nearby broken boundary sketches and smooth them. Conceptually, manual segmentation is more a tool than an algorithm. To the best of our knowledge, there is not a systematic manual segmentation tool yet. However, such a tool could be useful, especially when it comes to building a segmentation benchmark for structural-level mesh segmentation. Generating ground-truth segmented models could involve a large amount of strenuous and tedious work; having a handy segmentation tool should greatly improve the efficiency.

2.3 Spectral Clustering

In this section, we briefly review spectral clustering that has inspired our work. Spectral clustering refers to any partitioning algorithm that utilizes eigenvectors (and eigenvalues) of an appropriately defined matrix which captures the domain knowledge. Spectral clustering has its root in spectral graph theory [24, 35] and has seen a tremendous amount of work [9, 18, 37, 90, 97, 143] over the past decade. Spectral clustering can work either in 2-way, i.e., clustering data into two groups (recursively), or in k-way, i.e., clustering data into k groups simultaneously. Interested readers are referred to a recent survey [36] for details.

2.3.1 Classical Examples

Given a set of data points $\mathcal{Z} = \{z_i\}$, $|\mathcal{Z}| = n$, and an affinity matrix $W \in \mathbb{R}^{n\times n}$, where W_{ij} encodes the relation between z_i and z_j, clustering the data points in $\mathcal{Z}$ can be viewed as a graph partitioning problem, in which $\mathcal{Z}$ is the set of graph nodes and W_{ij} defines the weight of edge (i, j). Note that in different algorithms, W may be modeled to describe either the *similarities* or the *dissimilarities* between data: if similarity (dissimilarity) is modeled, a larger W_{ij} implies a more similar (dissimilar) pair of points.

Assuming that W encodes similarity information, the goal in the first example is to partition the graph nodes into two well-separated sets $\mathcal{Z}_1$ and $\mathcal{Z}_2$ such that

$$Cut(\mathcal{Z}_1, \mathcal{Z}_2) = \sum_{z_i\in\mathcal{Z}_1,\, z_j\in\mathcal{Z}_2} W_{ij}$$

is minimized. Denote by $\mathbf{v}$ the membership indicator vector ($\mathbf{v}^{(i)} = -1$, if $z_i \in \mathcal{Z}_1$, and $\mathbf{v}^{(i)} = 1$, if $z_i \in \mathcal{Z}_2$; note that $\mathbf{v}^{(i)}$ represents the i-th entry of $\mathbf{v}$), we have

$$Cut(\mathcal{Z}_1, \mathcal{Z}_2) = \frac{1}{4}\sum_{i,j} W_{ij}(\mathbf{v}^{(i)} - \mathbf{v}^{(j)})^2 = \frac{1}{2}\mathbf{v}^T(D-W)\mathbf{v},$$

where $D = \mathrm{diag}(D_{00}, \ldots, D_{nn})$ is a diagonal matrix whose diagonals are row sums of W, i.e., $D_{ii} = \sum_{z_j\in\mathcal{Z}} W_{ij}$. By relaxing the entries in $\mathbf{v}$ from discrete values to continuous values, subject to the constraint $\|\mathbf{v}\|_2 = 1$, it can be shown that the minimum value of $Cut(\mathcal{Z}_1, \mathcal{Z}_2)$ is achieved when $\mathbf{v}$ is the eigenvector of $D - W$ that corresponds to the smallest eigenvalue. However, since $D - W$ has the smallest eigenvalue 0 and its corresponding eigenvector is a constant vector, $\mathbf{v}$ is taken as the second smallest eigenvector to avoid the trivial solution. Due to the relaxation, the eventual clustering is $\mathcal{Z}_1 = \{z_i|\mathbf{v}^{(i)} < 0\}$, $\mathcal{Z}_2 = \{z_i|\mathbf{v}^{(i)} \geq 0\}$. This result is shown in [35]. For simplicity, we will from now on refer to an eigenvector as large or small based on its corresponding eigenvalue, i.e., the largest eigenvector refers to the eigenvector with the largest eigenvalue.

As the *Cut* measure undesirably favors small sets of isolated nodes, *Normalized Cut* is proposed in [115] to deal with this problem. For Normalized Cut, the quality measure is

$$NCut(\mathcal{Z}_1, \mathcal{Z}_2) = Cut(\mathcal{Z}_1, \mathcal{Z}_2)\Big(\frac{1}{Vol(\mathcal{Z}_1)} + \frac{1}{Vol(\mathcal{Z}_2)}\Big),$$

1. Build an affinity matrix W, set its diagonals to 0, and process $W \leftarrow D^{-\frac{1}{2}} W D^{-\frac{1}{2}}$.
2. Compute the eigenvalue decomposition $W = V \Lambda V^T$, where $V = \mathrm{diag}(\lambda_1, \lambda_2, \ldots, \lambda_n)$ and $\lambda_1 \geq \lambda_2 \geq \ldots \geq \lambda_n$, select the largest k eigenvectors from V and stack them into the columns of matrix U, i.e. $U = [V_1|V_2|\ldots|V_k]$.
3. Normalize each row of U, i.e., $U_{ij} \leftarrow U_{ij}/\|U_{i.}\|$.
4. Considering the rows of U as the Euclidean-embeddings of $\mathcal{Z}$, i.e., the i-th row is the embedding of z_i, cluster $\mathcal{Z}$ into k clusters.

Figure 2.2: NJW spectral clustering algorithm.

where $Vol(\mathcal{Z}_i) = \sum_{z_j \in \mathcal{Z}_i} D_{jj}$. D_{jj} measures the "degree" of z_j and $Vol(\mathcal{Z}_i)$ is the "volume" of $\mathcal{Z}_i$. Since $NCut$ is normalized by the volume of each cluster, the clustering result no longer favors small clusters as Cut does. Unfortunately, computing the optimal solution that minimizes $NCut$ is NP-complete; therefore, the authors suggest to find an approximate solution by computing the second smallest eigenvector of the generalized eigenvalue problem

$$(D - W)\mathbf{v} = \lambda D \mathbf{v},$$

and thresholding this eigenvector to derive the final cut.

Both spectral clustering algorithms mentioned above have clearly defined quality functions to optimize for. On the other hand, some spectral clustering algorithms are only empirically demonstrated or loosely proved to be able to discern the meaningful clustering structures present in a given data set. Such an example is the NJW algorithm by Ng, Jordan and Weiss [90], which runs as in Figure 2.2. The rationale behind this algorithm is revealed by considering the ideal case, in which the inter-cluster points have zero similarities (infinite distances). Without loss of generality, we assume that the points from the same cluster are numbered continuously; hence the affinity matrix W is block-diagonal. If there are k such ideal clusters, it is able to show that the embedded points (rows of U) from the same cluster would be mapped to a single point on the unit sphere. Essentially, there are k distinct points from k mutually orthogonal directions, which is easy to cluster. In reality when the inter-cluster affinities are non-zero, it can be viewed that a perturbation is added to W. It is shown that if W is still almost block diagonal and the size of each cluster and the degree of each node do not vary much, similar properties are still expected.

1. Build an affinity matrix W, which models the relations (similarities or dissimilarities) between each pair of data points in $\mathcal{Z}$. W is subject to further processing.
2. Compute the eigenvalue decomposition $W = V\Lambda V^T$, and use the eigenvalues and the eigenvectors to obtain an Euclidean embedding of $\mathcal{Z}$.
3. Cluster the embedded data points.

Figure 2.3: Standard paradigm of spectral clustering.

2.3.2 Generic Paradigm

A typical spectral clustering algorithm is comprised of three steps as shown in Figure 2.3. The first step builds an affinity matrix W that models the relationships among the data points in $\mathcal{Z}$. The information encoded in W reflects the domain knowledge about the problem at hand. In the second step, the eigenvectors (and eigenvalues) of W are used to derive an Euclidean embedding of $\mathcal{Z}$; this embedding is typically called spectral embedding. Spectral embedding per se has been studied intensively, in the context of manifold learning and dimension reduction. Famous examples include Local Linear Embedding [106], Isomap [125], and Laplacian Eigenmap [11]. They all share the common feature of utilizing local information to capture curved manifolds embedded in higher dimensional ambient space. In the last step, the actual clustering operation is applied to the embeddings. There are a variety of ways to implement the clustering, including the popular K-means algorithm [78]. The affinities in W determine the spectral embedding, and hence influence the quality of the clustering result. Therefore, it is crucial to compute meaningful affinities using the domain knowledge about the problem at hand. Spectral embedding transforms the affinity information in W into an Euclidean embedding, usually with low dimensionality, and the subsequent clustering operation is readily implemented.

Spectral clustering techniques are diverse and a universal spectral clustering algorithm that performs well on all kinds of data does not exist. There are several difficult questions related to spectral clustering, such as how to choose the right kernel width for building the affinity matrix W and how to cluster in the spectral embedding space [37, 83]. In the subsequent chapters, we design spectral clustering algorithms suitable for the purpose of mesh segmentation; various related problems are solved within our application context.

Chapter 3

Part-aware Metric

3.1 Overview

Since we apply spectral clustering to mesh segmentation and a crucial prerequisite for applying spectral clustering is to encode the domain knowledge of the problem at hand in an affinity matrix, in our application, we need a metric to prescribe distances between the faces of a given mesh. In this chapter, we only develop such a metric. How to use the metric to define an affinity matrix for spectral clustering is left to the next chapter.

The distances between mesh faces prescribed by our metric should be suitable for structural-level segmentation. In other words, we want distances between the faces from the same part to be small, while distances between the faces from different parts to be large. However, defining such a distance measure is challenging, since the concept of a "part" is not well-defined. Moreover, the distance measure should be simple to compute yet effective for the subsequent segmentation task; we shall not run a third party segmentation algorithm to find the parts of a mesh first and then compute distances between the faces accordingly.

In this chapter, we derive three distance measures: *geodesic*, *angular*, and *VSI* distances, in Section 3.2, Section 3.3, and Section 3.4, respectively. The VSI distance is most effective in encoding part information, and the other two complement the VSI distance in different scenarios. The resulting part-aware metric, described in Section 3.5, is a combination of the three. Since our part-aware metric is of generic interest, we show its use in several non-segmentation geometry processing applications in Section 3.6. A summary is given in Section 3.7. In subsequent chapters, we show how the metric is used for mesh segmentation.

3.2 Geodesic Distance

Consider two faces on a mesh surface. In general, they tend to belong to different parts if they are geodesically far apart and vice versa. This is in accordance with the Gestalt principle of proximity [88] about perception. Therefore, the first distance measure we employ is the geodesic distance between faces.

Computing accurate geodesic distances [122] on surfaces is quite involved and not necessary for our purpose. Instead, we make use of the dual graph of a mesh to derive approximate geodesic distances between faces. A mesh dual graph, $\tilde{G}$, is constructed by representing the faces of a mesh by nodes and connecting the nodes whose corresponding faces share a common edge. This is illustrated in Figure 3.1(a).

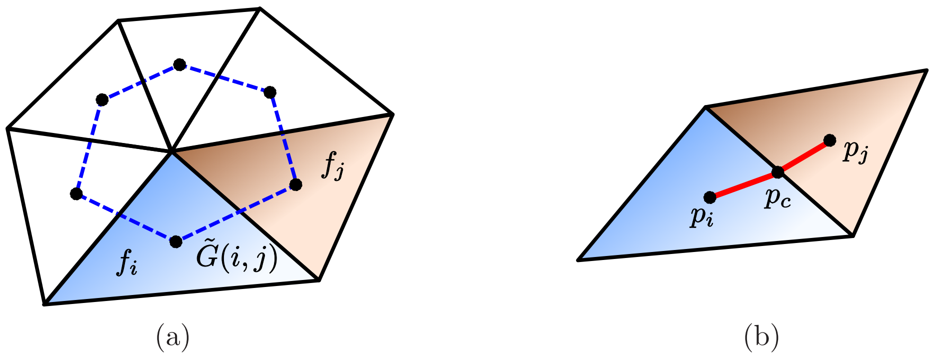

Figure 3.1: Mesh dual graph and approximate geodesic weight between adjacent faces. In (a), the dashed blue lines are the edges of the dual graph $\tilde{G}$; $\tilde{G}(i,j)$ denotes the edge incident to faces f_i and f_j. (b) shows how the weight of $\tilde{G}(i,j)$ is computed.

$\tilde{G}$ stores the connectivity information of the faces. Note that for a triangle mesh without boundary, $\tilde{G}$ is a graph whose nodes all have degree 3. Given an edge $\tilde{G}(i,j)$, we denote by p_c the middle point of the common edge shared by f_i and f_j, and by p_i and p_j the centroids of f_i and f_j, respectively. The weight of $\tilde{G}(i,j)$ is defined as

$$\text{weight}\left(\tilde{G}(i,j)\right) = ||p_i - p_c|| + ||p_j - p_c||. \tag{3.1}$$

This is shown in Figure 3.1(b).

With the edge weights defined, the geodesic distance between any two faces is approximated by the shortest graph distance between their corresponding nodes in $\tilde{G}$. From now on, we refer to the dual graph with geodesic edge weights as $\tilde{G}_g$.

Note that in general, geodesic distance alone does not reflect part structure robustly, which can be seen from Figure 3.2(a). Nonetheless, geodesic distance is important in some part-related applications (see Section 3.6). Even for mesh segmentation, it can be exploited to improve segmentation quality. We shall see such examples in Chapter 4 and Chapter 6.

3.3 Angular Distance

Angular distance is similarly obtained through another mesh dual graph $\tilde{G}_a$. $\tilde{G}_a$ has the same structure with $\tilde{G}_g$, but with different edge weights. Given two adjacent faces f_i and f_j with normals n_i and n_j, respectively, the weight of edge $\tilde{G}_a(i,j)$ is defined as

$$\text{weight}\left(\tilde{G}_a(i,j)\right) = \begin{cases} \text{acos}(n_i \cdot n_j)/\pi & \text{if } f_i \text{ and } f_j \text{ form a concave dihedral angle,} \\ \epsilon & \text{if } f_i \text{ and } f_j \text{ form a convex dihedral angle.} \end{cases} \tag{3.2}$$

We set $\epsilon = 0.001$ to emphasize concave angles: the more concave a region is, the larger the weights are. This is roughly in accordance with the minima rule (Section 1.1.3). With $\tilde{G}_a$, the angular distance between any two faces is their shortest graph distance in $\tilde{G}_a$.

Figure 3.2 shows a geodesic distance field and an angular distance field on a dolphin model. As we can see from this example, the geodesic distance fails to induce large distances across the concave boundary regions between the body and the fins/beaks, while the angular distance manifests large distance jumps across those regions. Note that in this thesis, we color plot scalar fields by linearly interpolating the hue values in the HSL color space; bluish colors indicate small field values and reddish colors indicate large field values. Since we are not interested in the exact values of a distance field but its relative variations across a mesh surface, we do not show color bars in such figures.

Although it reflects the parts of a shape when concave regions are present, angular distance suffers from what we call the *leakage* problem. This is caused by defining edge weights using only local surface properties. Figure 3.3 contrasts a geodesic distance field with an angular distance field on a synthetic “snake” model to illustrate this problem. From Figure 3.3(b), we see that although a concave region separates the left vertical part from the horizontal part, the concave region itself does not form a closed loop between the two parts. Therefore the shortest path between the two parts goes through the flat region to avoid the concave region, as indicated by the magenta curve. As a result, the angular distance field

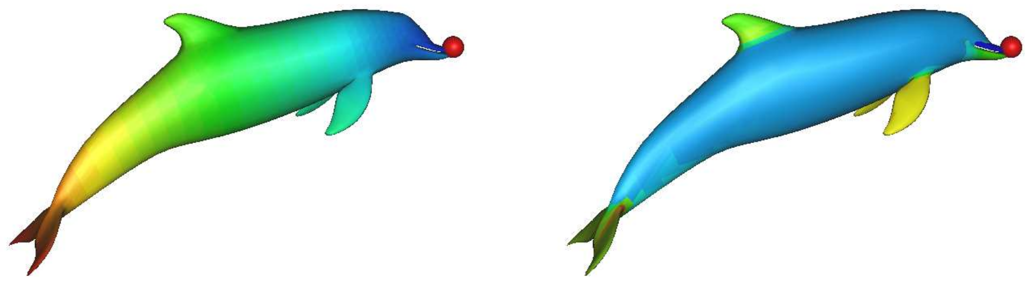

(a) geodesic distance field (b) angular distance field

Figure 3.2: Example geodesic and angular distance fields on a dolphin model, where the red sphere indicates the source face. From the angular distance field, we see large distance jumps across the concave regions between the parts; this phenomenon is not observed from the geodesic distance field.

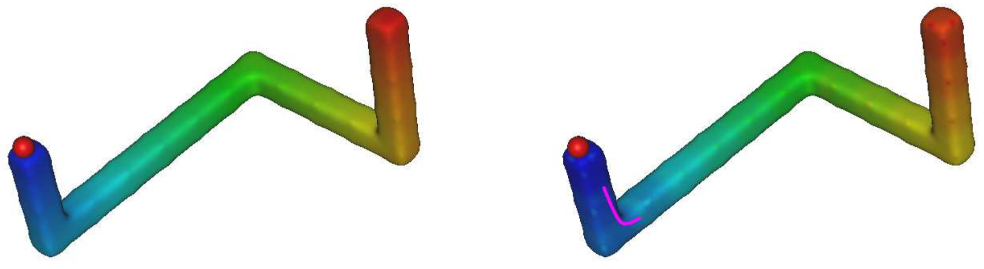

(a) geodesic distance field (b) angular distance field

Figure 3.3: Example geodesic and angular distance fields on a snake model. We see that the angular distance field is not sufficiently different from the geodesic distance field due to the leakage problem. The red sphere indicates the source face.

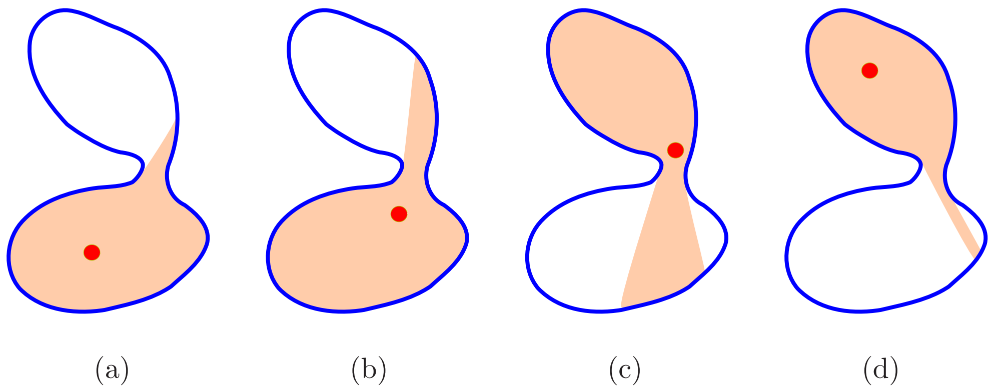

Figure 3.4: Visible regions of a point (red dot) as it travels inside a shape. Comparing (a) and (b), or (c) and (d), we see the shape of visible regions are similar when the point stays in the same part. There is a large change in the shape of the visible region as the point crosses the part boundary, as shown in (b) and (c).

looks almost the same with the angular distance field, failing to reflect the part structure of the snake model.

3.4 VSI Distance

In retrospect, although separation between parts inevitably involves concavity, to capture it one is not restricted to surface measurement. The inherent limitation of surface measurement can be addressed from a more global and volumetric view for part analysis. This leads to the realization that shape concavity can be manifested inside the shape's volume via occlusion or visibility considerations.

Specifically, we examine a 3D object from within its enclosed volume and measure the visibility of the object surface from appropriately chosen reference points in the volume. Unlike a “part”, a visible region is clearly defined. Since parts are generally convex, the visible regions from within a part remain stable or change only gradually while moving inside the part. In contrast, when moving across a part boundary to another part, the visible region undergoes large change due to the concave regions separating the two parts. Such a property is exemplified in Figure 3.4. In this section, we exploit this idea and develop a robust part-aware distance measure based on the difference of visible regions.

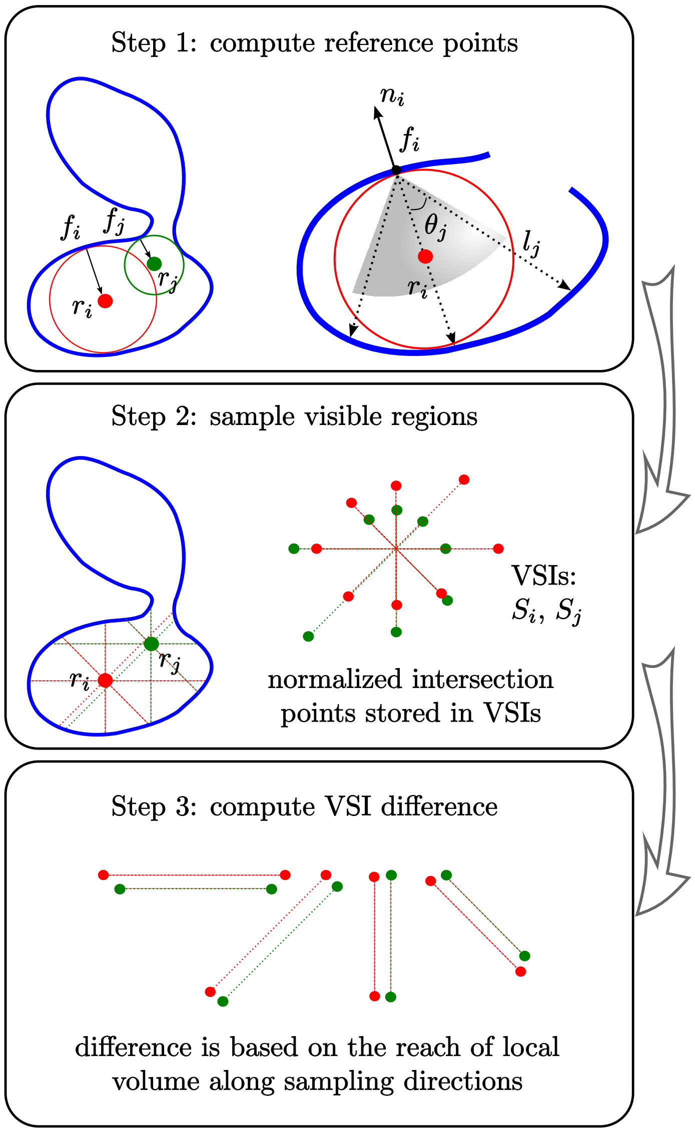
Step 1: compute reference points
n_i
f_i
f_j
r_i
r_j
θ_j
l_j
Step 2: sample visible regions
VSIs:
S_i, S_j
normalized intersection points stored in VSIs
Step 3: compute VSI difference
difference is based on the reach of local volume along sampling directions

Figure 3.5: Three steps to compute VSI distance. In step 1, two example faces (suppose they are adjacent), f_i and f_j are mapped to their reference points r_i and r_j. In step 2, the visible regions at r_i and r_j are sampled and stored in their VSIs, S_i and S_j. In step 3, S_i and S_j are used to derive the distance between f_i and f_j in graph $\tilde{G}_v$.

3.4.1 Algorithm Overview

Our algorithm to define VSI distance is divided into three steps, which are briefly depicted in Figure 3.5. In the first step, we map each face on a surface to its reference point inside the shape, from which the visible region is measured. We do not capture visible regions from the surface, which may offer significantly different perspectives. Mapping faces to reference points helps alleviate problems of computing visible regions from the surface due to surface noise.

In the second step, we express the visible region of a reference point via a surface attribute, called *Volumetric Shape Image* (VSI). To characterize visible regions so that their differences can be measured effectively, merely using their volumes is insufficient. We need a more descriptive signature. A straightforward approach is to compute the actual visible regions and examine how much they overlap. However, a visible region, generally a complex 3D polyhedron, is expensive to compute. We instead resort to a sampling approach: from a reference point, multiple rays are shot out; then the normalized intersection points between the rays and the surface form the signature, VSI.

In the third step, we compute the distance between two adjacent faces by comparing their VSIs. The distances between adjacent faces form the edge weights of another dual graph $\tilde{G}_v$, which is called a VSI graph and has the same connectivity with $\tilde{G}_g$ and $\tilde{G}_a$. Similar to geodesic and angular distances, the VSI distances between faces are the shortest graph distances in $\tilde{G}_v$.

We elaborate the details of the algorithm in the following sections.

3.4.2 Reference Point Construction

Due to the sensitivity of visible regions to surface noise, reference points should not be close to the mesh surface. We have found mapping surface points onto the medial sheet to be a good choice for reference point construction. Give a point on the surface, its corresponding medial center is the center of the maximal sphere inside the shape and tangent to the surface at the point. To compute the reference point r_i for face f_i, which is the medial center corresponding to the centroid of f_i, we adopt the simple ray-shooting technique of Shapira et al. [112].

Given a face f_i with normal n_i, as shown in Figure 3.5 (step 1), we use a cone with apex at the centroid c_i of f_i and center its axis along $-n_i$. Multiple rays uniformly sampled inside

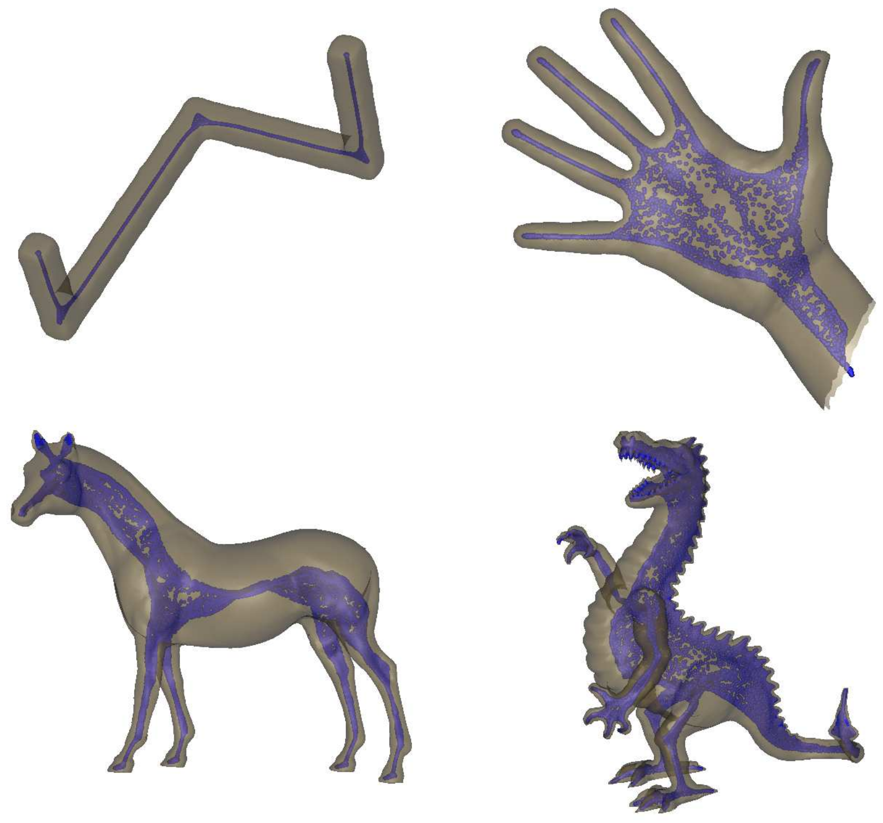

Figure 3.6: Reference points, shown as blue dots, computed for various models.

the cone, including one along $-n_i$, are cast into the shape. Denote by l_j one of the rays, and $\|l_j\|$ its length inside the shape. The approximate diameter of the maximal inscribed sphere touching c_i at the surface is

$$d_i = \text{argmin}_j\{\|l_j\|/\cos\theta_j\},$$

where θ_j is the angle between l_j and $-n_i$. The reference point r_i is the center of that sphere with radius $d_i/2$, namely,

$$r_i = c_i - 0.5 * d_i * n_i.$$

If the local shape is a sphere, all the d_i's are equal to its actual diameter. Due to the way they are constructed, reference points are always inside the shape.

In practice, we set the opening angle of the cone to 80 degrees and cast 16 rays. Note that if the opening angle is too large, some rays (those with large angles to $-n_i$) may hit the surface immediately after being shot out, making the resulting reference points undesirably close to the surface. We have found that our setting achieves quality results with high efficiency. To further improve the robustness of reference points against surface noise and possible poor tessellation quality, the reference points are subject to a Laplacian smoothing over a neighborhood graph. The neighborhood graph connects two reference points if their corresponding faces are adjacent on the mesh, or if the points themselves are close Euclidean neighbors to each other. In very rare cases, a reference point may move outside the mesh surface after the smoothing, which can be detected later on and at that time this reference point is simply moved to its nearest neighbor that stays inside the mesh. Figure 3.6 shows the reference points computed for four models.

It is worth emphasizing that we only compute the medial points roughly as the reference points need not strictly reside on medial sheets. Computing rigorous medial sheets [28, 32] of polygonal shapes is expensive and unnecessary for our purpose.

3.4.3 Volumetric Shape Image (VSI)

We sample the visible regions as seen from the reference points and quantify their differences. From a reference point r_i, we send out m rays uniformly sampled on a Gaussian sphere and collect the intersection points, $s_i^{(j)}$'s, between the rays and the surface. Each intersection point is normalized with respect to its reference point, i.e., $s_i^{(j)} \leftarrow s_i^{(j)} - r_i$. The normalized intersection points are stored in a set $S_i = \{s_i^{(1)}, \ldots, s_i^{(m)}\}$, called the volumetric shape image (VSI) of r_i (or of f_i). A larger m leads to better approximation of visible regions by VSIs, but at a higher complexity. We found that setting $m = 100$ achieves a good trade-off between accuracy and efficiency. Figure 3.5 (step 2) shows two VSIs, S_i (red) of r_i and S_j (green) of r_j. To avoid cluttering in the figure, only 8 sampling rays are drawn.

Since the directions of sampling rays are fixed in a global coordinate system, two VSIs are naturally registered. We may define the difference between two VSIs simply as: $\mathrm{diff}(S_i, S_j) = \frac{1}{m}\sum_{k=1}^{m}\|s_i^{(k)} - s_j^{(k)}\|^2$, which tends to possess large values near boundary regions due to dramatic visible region changes. Albeit meaningful, such a measure fails to accommodate accumulated translation errors. Consider a reference point moving within a large part. Though the slight translation between two adjacent positions generates only a small VSI-difference, such small differences are easily accumulated up along the way. This can be observed from the significant difference between S_i and S_j, as illustrated in Figure 3.5 (step 2), despite that both r_i and r_j are within the same part.

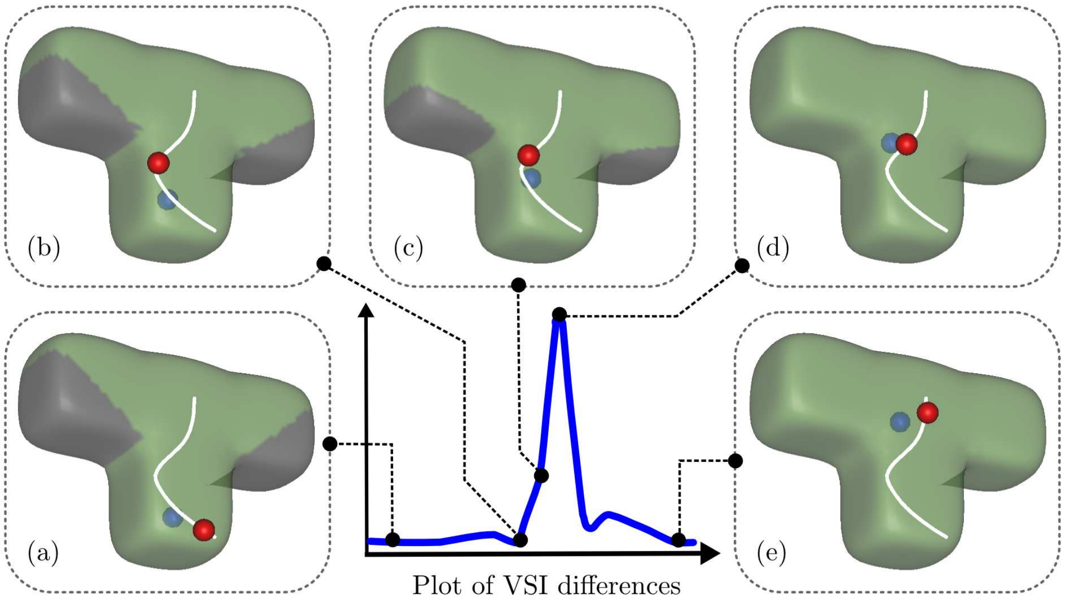

Figure 3.7: Plot (blue curve) of VSI differences as a point (red dot) moves along the white curve on the surface. Visible regions at reference points (blue dots) are in green. (a)-(b): Gradual changes of visible region and VSI (difference ≈ 0) while in the bottom part. (c)-(d): Large change near part boundary. (e): Gradual changes while in the top part.

We have observed that the reach of a local volume along a certain direction, measured from reference points, is in general more stable. Figure 3.5 (step 3) attests to this observation, where we see that the reach of the lower part volume along the four directions are almost the same, though r_i and r_j are distant. To exploit this property, we pick the m sampling rays in opposite directions ($m/2$ ray pairs). Supposing the two intersection points of a ray pair are stored consecutively in S_i, we define the difference between two VSIs as

$$\mathrm{diff}(S_i, S_j) = \frac{1}{\sum_k w_k} \sum_{k=1}^{m/2} w_k \left(l_i^{(k)} - l_j^{(k)} \right)^2, \tag{3.3}$$

where $l^{(k)} = \|s^{(2k-1)} - s^{(2k)}\|$ is the local reach along the k-th direction. Weights w_k's are designed to penalize outliers: since VSI is discrete, not all $(l_i^{(k)} - l_j^{(k)})^2$ may faithfully reflect the difference of the visible regions. To tackle this problem, we fit a Gaussian to the distribution of such values and set

$$w_k = \begin{cases} e^{-(d_k-u)^2/(2\sigma^2)} & \text{if } d_k < u + 2\sigma \\ 0 & \text{else } d_k \geq u + 2\sigma \end{cases}, \tag{3.4}$$

where $d_k = (l_i^{(k)} - l_j^{(k)})^2$, u is the mean, and σ is the standard deviation. Accordingly, values are weighted based on their frequencies. Outliers falling two deviations above the mean are ignored. Figure 3.7 illustrates how diff$(\cdot)$ changes between two adjacent positions when a point travels on the surface of a simple synthetic "T" shape.

With the edge $\tilde{G}_v(i,j)$ of graph $\tilde{G}_v$ weighted by diff(S_i, S_j), VSI distances are simply the shortest graph distances in $\tilde{G}_v$. Two VSI distance fields on the snake model are shown in Figure 3.8. Compared with the geodesic and angular distance fields on the same model in Figure 3.3, VSI distance stays fairly stable within parts, and induces large jumps across part boundaries. More comparative results on natural models are provided in Figure 3.9. Notice how the boundary regions, either between the little finger and the palm, between the horse's front leg and the body, or between the dragon's tail and the body, manifest significant VSI distance changes. From these examples, we see that VSI distance clearly outperforms angular distance with respect to encoding part structures.

Two practical Issues Computational-wise, the most expensive part of constructing $\tilde{G}_v$ is the ray-surface intersection tests required by computing reference points and VSIs. Suppose an input mesh has n faces, computing reference points and VSIs require $16n$ and $100n$ intersection tests, respectively. To speed up the processing, we voxelize the space using an axis-aligned grid and assign each mesh face to the voxels it intersects. In our implementation, we fix the number of voxels to 10^6. According to the extent of an input mesh along each axis, the resolution of the grid along an axis is dynamically modified proportionally. During the ray-surface intersection test, we traverse the voxels along the ray direction for intersection detection. When an input mesh is dense, we further speed up the processing by computing VSIs for only a small set of reference points and interpolating for nearby ones. In our implementation, we compute only 1% of the VSIs and the remaining ones are interpolated. Therefore the total number of ray-surface intersection tests is $16n + 1\% \cdot 100n = 17n$.

Also note that although our discussion has assumed closed meshes so far, VSIs can be computed for open meshes as well, so long as the mesh volume is reasonably well-defined. This is achieved by simply ignoring rays that do not intersect the surface. The hand model in Figure 3.9 is an open mesh.

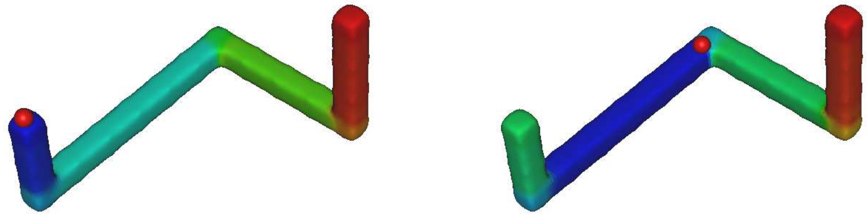

Figure 3.8: Two VSI distance fields on the snake model. Red spheres indicate source faces.

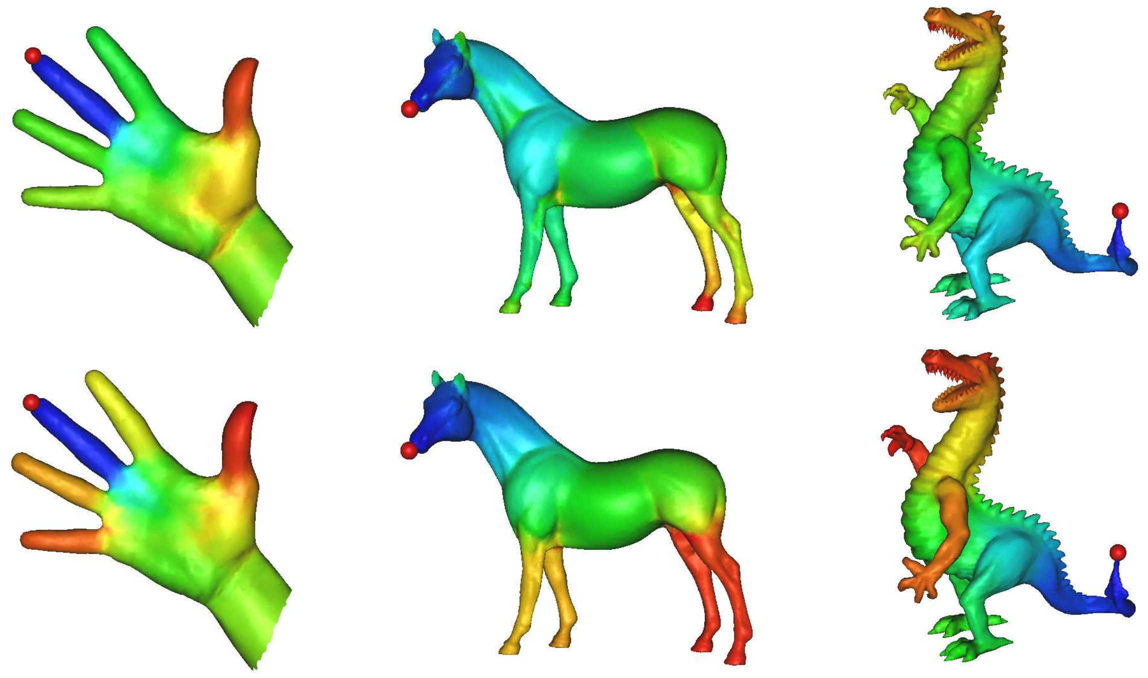

Figure 3.9: Angular distance fields (top row) vs. VSI (bottom row) distance fields on various models. Red spheres indicate source faces.

3.5 Combining Distances

The final part-aware distance we develop is a combination of the geodesic, angular, and VSI distances. In order to derive the combined distance, we blend the three graphs, $\tilde{G}_g$, $\tilde{G}_a$, and $\tilde{G}_v$, i.e.,

$$\tilde{G}_c = \left(\alpha \otimes \tilde{G}_g\right) \oplus \left(\beta \otimes \tilde{G}_a\right) \oplus \left(\gamma \otimes \tilde{G}_v\right), \tag{3.5}$$

where $\alpha + \beta + \gamma = 1$ and $0 \leq \alpha, \beta, \gamma \leq 1$. Operator $\otimes$ multiplies the edge weights of a graph by a scalar, and $\oplus$ blends two graphs by summing up the weights of corresponding edges. The final part-aware metric is defined as the shortest graph distances between the nodes of $\tilde{G}_c$. Note that as the three graphs encode different types of information, their edge weights must be normalized first. To this end, we linearly normalize the edge weights of each graph to $[0, 1]$.

For the part-aware metric, the parameters, α, β and γ, control the relative importance of the three distances, and their setting is application-dependent. For example, in structural-level mesh segmentation, we are primarily interested in a shape's part structure; therefore we should emphasize the VSI distance. For shape registration, however, the importance of geodesic distance ought to be increased, as both the invariance to stretching (merit of VSI distance) and the invariance to pose (merit of geodesic distance) are desired. Note that the edge weights in $\tilde{G}_g$ are biased towards 1 after the normalization, since the majority of the edges or the faces of a mesh typically tend to have similar sizes. However, this is not true for the edge weights in $\tilde{G}_a$ and $\tilde{G}_v$. For this reason, α is typically set to a small value in order for the other two distances to take effect.

3.6 Experimental Results

Complexity Let's first have a look at the expected asymptotic complexity of constructing the graph $\tilde{G}_c$. Given an input mesh $\mathcal{M}$ with n faces, constructing the graphs $\tilde{G}_g$ and $\tilde{G}_a$ involves only local tests and the complexity is $O(n)$. The dominant complexity comes from building $\tilde{G}_v$ where intersections between rays and surface have to be computed. Let's assume that a space partitioning grid is used and the resolution along each dimension is r. The expected number of voxels traversed before a ray hits a face is at most of $O(r)$. Our experiments show that typically only about 3% of the voxels are non-empty; so each non-empty voxel contains about $100n/3r^3$ faces. As a result, each ray-surface intersection test involves a complexity of $O(r + 100n/3r^3)$ in expectation. As per Section 3.4.3, there are $17n$ such tests, making the overall complexity to $O\big(17rn + 1700n^2/3r^3\big)$. Though the theoretical comlexity is quadratic, the constant factor $3r^3$ (3×10^6 in our implementation) is able to reduce the complexity effectively in practice. If an input mesh is huge, we can increase the resolution of the grid accordingly. For example, computing VSIs for the dragon model with 50K faces in Figure 3.6 takes about 15 seconds.

Overview of experiments Although we develop the part-aware metric for mesh segmentation, the metric itself, as a general tool, can be exploited in many other applications as well. In this section, we conduct several experiments to verify the effectiveness of the part-aware metric for some non-segmentation applications, including sampling, registration, and retrieval. We show how this metric is used for segmentation in subsequent chapters.

In the first experiment, our part-aware distance (with emphasis on the VSI distance) is compared with three existing ones to show how the VSI distance helps capture part information. The three distances are the geodesic distance, the geodesic+angular distance [59], and the diffusion distance studied in [30]. Modeled using random walk, the diffusion distance measures the overall connectedness between points over the surface. It considers more global information than the geodesic and angular distances, hence more sensitive to parts in general. However, it is still purely surface-based and does not account for volumetric information explicitly. The iso-contour plots in Figure 3.10 clearly show that only our part-aware metric fully senses the boundary of the bottom part of the "T" shape. This is not surprising because the VSI difference based on visible region changes is not affected by the local flatness, as already shown in Figure 3.7.

Part-aware sampling: The max-min sampling scheme can be used for uniform sampling on a surface. It iteratively places a sample that maximizes the minimum distance, measured by the geodesic metric, from all previously found samples. Beyond uniform sampling, it is often desirable to distribute samples based on certain feature criteria. In typical feature-sensitive remeshing, more samples are placed near high curvature regions, resulting in higher triangle density therein. This can be accomplished using max-min sampling, but with the isophotic metric [66]. Figure 3.11(a) shows a feature-sensitive sampling on the pliers model. When our part-aware metric is applied, the feature regions tend to correspond to part boundaries, even if a boundary region is locally flat (different from feature-sensitive sampling). This is shown in Figure 3.11(b). In this test, we set $\alpha = 0.01$, $\beta = 0$, and

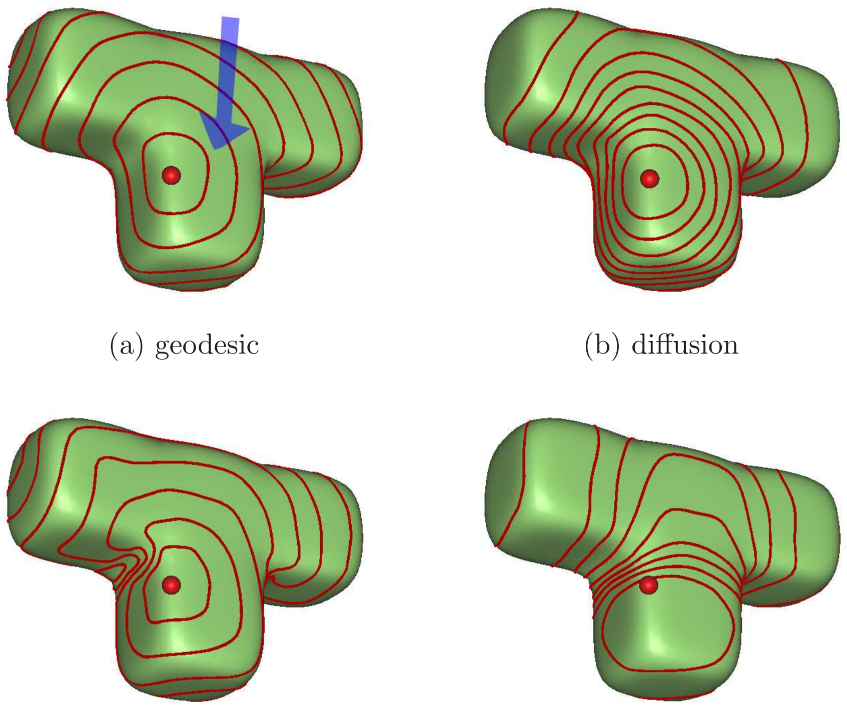

(a) geodesic (b) diffusion

(c) geodesic+angular (d) part-aware

Figure 3.10: Iso-contours for four distance metrics: 10 contours sampled up to the maximum distance from the source (red dot). Both geodesic (a) and diffusion (b) distances are insensitive to the perceived part boundary over the flat region indicated by the arrow. Angular distance (c) senses concavity, but not the part boundary over the flat region. Our part-aware metric (d) senses the whole part boundary.

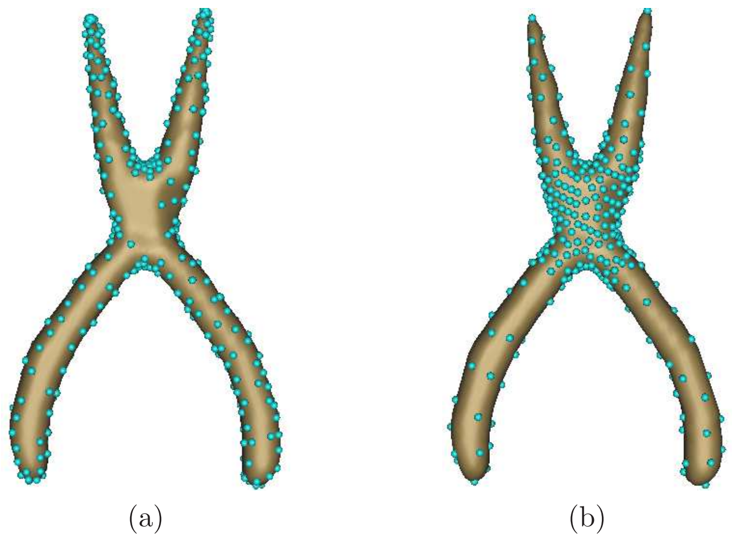

Figure 3.11: Feature-sensitive sampling (a) vs. part-aware sampling (b), where the cyan dots indicate the sample vertices. The sampling rate is 10%.

$\gamma = 0.99$. We emphasize the VSI distance and ignore the angular distance, so that samples would not concentrate in concave regions.

A straightforward use of a part-aware surface tessellation is in neighborhood traversal: a part-aware neighborhood can be traced simply by following topological distances in the mesh graph. Also, more granularities near part boundaries enable more refined deformation behavior over those non-rigid regions. In contrast, having large triangles which cut across part boundaries would be undesirable in this context.

Shape registration: Shape registration or correspondence [21, 53] is another good example where a surface metric can become useful. For such a task, bending-invariance is an important property and it has been successfully addressed [33] by using geodesic distance, which is insensitive to bending. However, stretch-invariance still remains challenging. In this experiment, we investigate how our part-aware metric could potentially improve shape registration. To this end, we consider the spectral correspondence framework [53]. Briefly, we spectrally embed mesh vertices into a Euclidean space and the registration is established by corresponding the embeddings using the iterative closest point algorithm [14].

Figure 3.12 shows the derived embeddings of two Homer models. To focus on stretching, we purposely stretched the left arm and the right leg of one Homer. As stretching changes the geodesic distance between vertices, the resulting embeddings in (b) and (e) using the

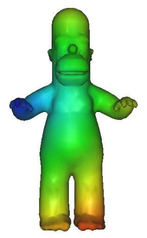
(a) Homer

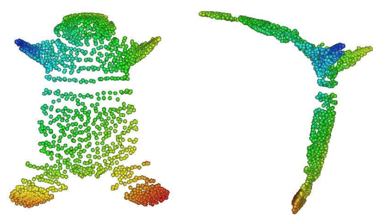
(b) geodesic

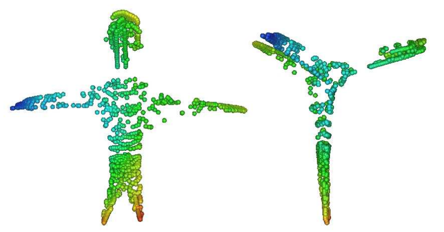
(c) part-aware

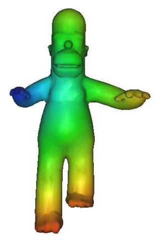
(d) stretched

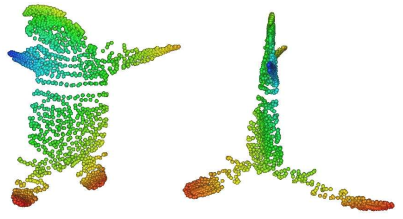
(e) geodesic

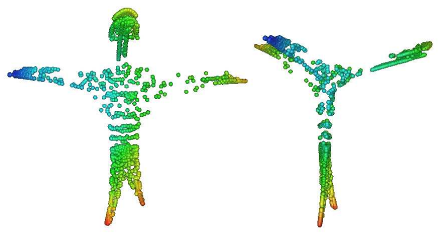
(f) part-aware

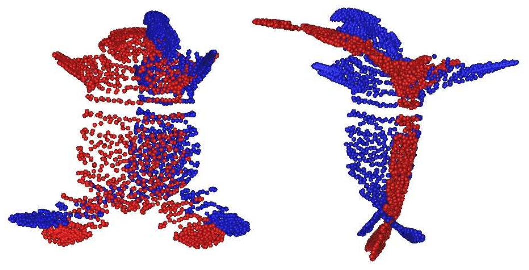
(g) registration of (b) and (e)

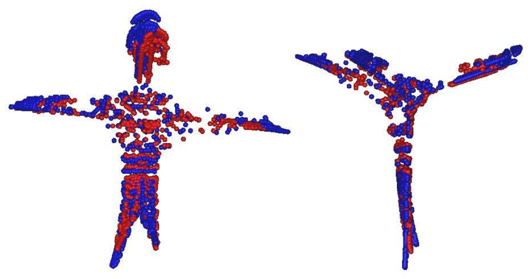
(h) registration of (c) and (f)

Figure 3.12: Spectral embeddings and registration of two Homer models. In the first row, plots (b) and (c) show the embeddings of the original Homer (a) using geodesic and part-aware distances, each of which from two viewing angles. Similarly, the second row is for the stretched Homer (d). The coloring implies the mapping between the original mesh vertices and their embeddings. We see that the embeddings in (c) and (f) are much more similar to each other than those in (b) and (e) (especially for the feet), thanks to the stretch-invariance of VSI distances. This helps the subsequent registration operation, whose results are shown in (g) and (h).

geodesic distance are quite different. In contrast, the VSI distance is more stable against stretching. When it is combined with the geodesic distance, the embeddings in (c) and (f) are made much more similar, facilitating the registration operation in sequel. We set $\alpha = 0.1$, $\gamma = 0$, and $\gamma = 0.9$ and note that this setting places sufficient emphasis on geodesic distances as per the weight distribution in $\tilde{G}_g$ (see Section 3.5).

In practice, we believe that both geodesic and VSI distances should be considered simultaneously for registration, since the former contributes to bending-invariance, while the latter contributes to stretch-invariance. Also, the geodesic distance imposes certain distances between neighboring vertices and keeps them adequately spread-out in the embedding. Their weights may be tuned to strike the balance between the two. It is worth investigating how their weights can be set automatically based on the input data.

Shape retrieval: We also study the potential benefits our metric can offer for shape retrieval. Osada et al. [91] consider using the probability distribution sampled from a shape function as a shape descriptor. It is suggested that the $D2$ shape function, namely the pairwise Euclidean distances between surface points, serves as a good candidate. Geodesic distance shape function is investigated in [81]. Although it is invariant to bending, the probability distribution function of geodesic distances is not sufficiently discriminative in general. We plan to add more discriminating power to this descriptor, while preserving sufficient bending-invariance.

In our experiment, we select ten models shown in Figure 3.13. The first five of them (kangaroo, cat, camel, wolf, and dinopet) are animals with similar part structures, but under different articulation and stretching. In retrieval, the ideal result should be that when using each of these five shapes to query, the other four come on top. We consider three shape functions: geodesic, $D2$, and our part-aware distances. For each sampled shape function, we compute its histogram, which serves as the shape descriptor. During retrieval, the χ-square distances between histograms are used to rank the matches. Figure 3.14 shows the retrieval results using the three shape functions. We see that only our part-aware metric is able to consistently achieve the ideal results for all the five similar shapes. Note that in the last column, we query using the octopus simply for comparison purpose, in which the ideal ranking is hard to judge.

We set $\alpha = 0.02$, $\beta = 0$, and $\gamma = 0.98$, making $\gamma \gg \alpha$ to showcase our goal. From Figure 3.13, we observe that the histograms of geodesic and $D2$ distances stay relatively stable. Contrastingly, the part-aware metric produces more discriminating histograms. Meanwhile,

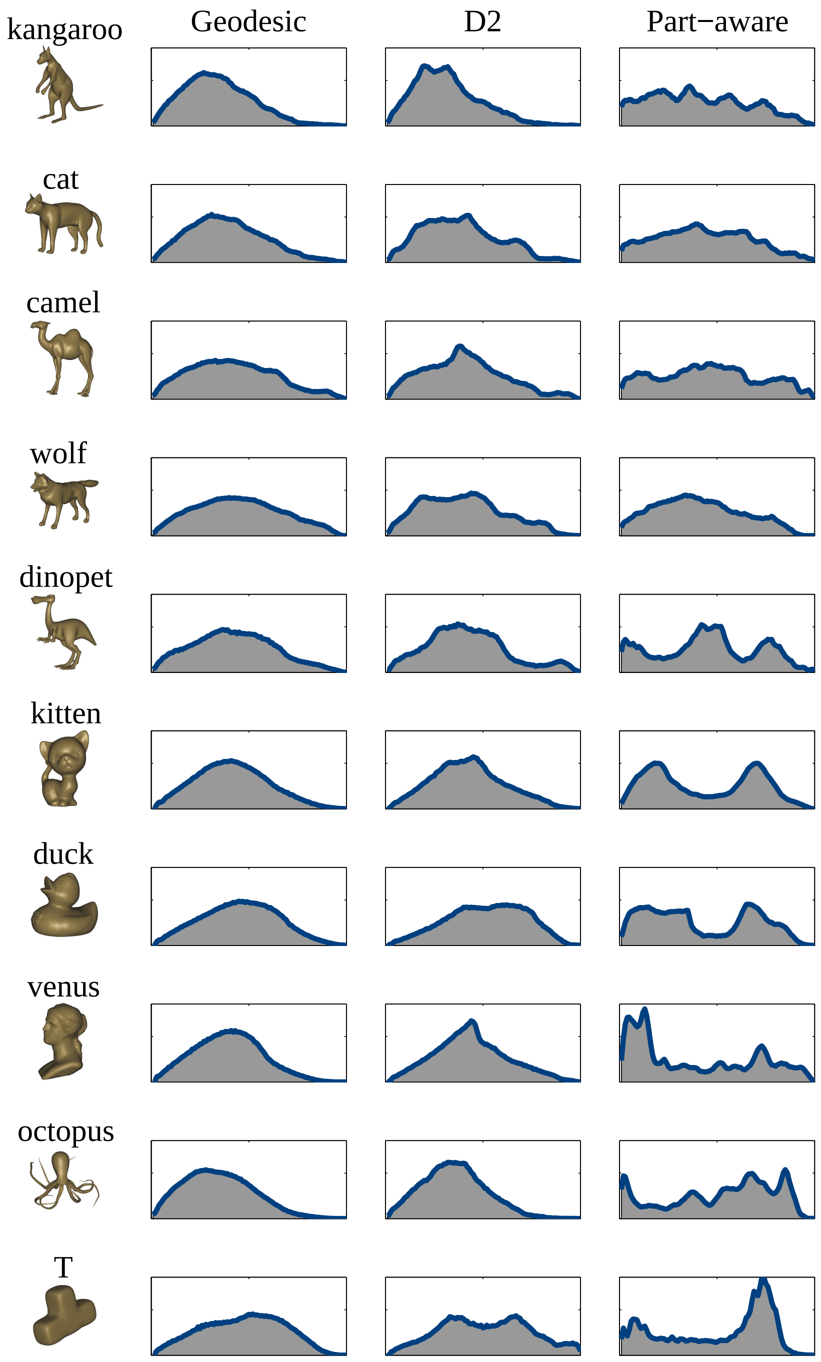

Figure 3.13: Models used for shape retrieval test and their signature histograms. The last three columns show the distance histograms of each model, via geodesic, $D2$, and part-aware distances, respectively.

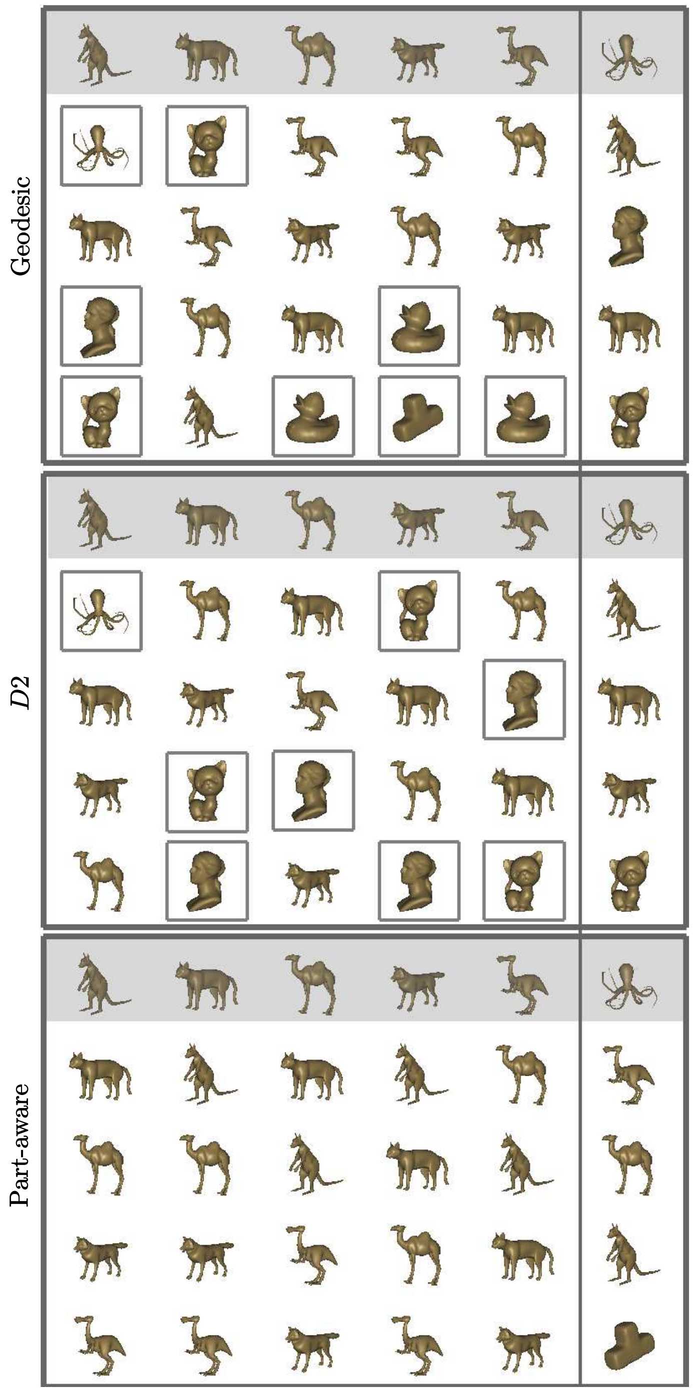

Figure 3.14: Retrieval results using geodesic, $D2$, and part-aware distances. In each block, we run 6 queries and the query shapes sit in the first (shaded) row. In each column, the 4 most similar shapes are shown; the non-optimally retrieved shapes are marked by squares.

due to the geodesic ingredient in the metric, bending invariance is also preserved to a certain extent; this is exemplified by the similarity among the first four histograms in the last column. This experiment highlights an advantage of our metric: by combining geodesic distance and VSI distance, it provides an effective compromise between bending-invariance and discriminating capability. However, this is a rather preliminary test and it is worth expanding the database and investigating more in this issue.

3.7 Summary

A part-aware metric, as a fundamental tool, is not only useful for mesh segmentation, but also of general interest to a variety of geometry analysis and processing tasks. Although isophotic [66] and diffusion [30] distances have been successfully applied to mesh segmentation, the distances themselves do not explicitly take part information into consideration.

In this chapter, we develop a part-aware surface metric specifically for encoding part information. The metric combines three components: geodesic, angular, and VSI distances. Our key observation is that the visible region, of a point inside the shape volume, is sensitive to part boundaries. Such a property is realized into the VSI distance which effectively captures part information, while geodesic and angular distances complement the VSI distance. We compare our metric against existing ones and also apply it to several part-related applications, including shape registration, part-aware sampling, and shape retrieval. The effectiveness of our metric is testified empirically. We make use of this metric for mesh segmentation in the following chapters.

Chapter 4

Segmentation using Spectral Clustering

4.1 Overview

Using the part-aware metric from Chapter 3, we develop a k-way mesh segmentation algorithm based on spectral clustering in this chapter. Figure 4.1 gives the flow of the algorithm.

```
input  : Mesh $\mathcal{M}$, the number of segments $k$.
output: Sub-meshes $\mathcal{O} = \{\mathcal{M}_1, \mathcal{M}_2, ..., \mathcal{M}_k\}$.
begin
    $U \leftarrow$ ComputeEmbedding($\mathcal{M}$) ;             /* Section 4.2 */
    $\mathcal{O} =\leftarrow$ Kmeans($\mathcal{M}$, $U$, $k$) ;   /* Section 4.3 */
end
```

Figure 4.1: Mesh segmentation based on spectral clustering.

Given an input mesh $\mathcal{M}$ and an intended number of segments k from a user, the algorithm first constructs a spectral embedding U (Section 4.2) for the faces of $\mathcal{M}$, using the part-aware metric. We study our spectral embedding algorithm along with several related issues in the light of kernel principal component analysis. With the embedding U at hand, the classical K-means clustering algorithm is readily applied to obtain the segmentation result (Section 4.3). Several questions associated with K-means are also addressed. Experimental results and summary are presented in the last two sections.

4.2 Construction of Spectral Embedding

The spectral embedding for the faces of the input mesh $\mathcal{M}$ is derived from their distances prescribed by the part-aware metric using the algorithm presented in Figure 4.2. There are many spectral embedding algorithms and they all have their own pros and cons. Our embedding algorithm is designed specifically for mesh segmentation, and it is analyzed in the light of kernel principal component analysis [109]. We also address several practical issues that are critical to the effectiveness of the algorithm.

1. Compute a distance matrix G and convert it to an affinity matrix W, where $W_{ij} = e^{-G_{ij}/2\sigma^2}$ and σ is set to the square root of the average of the entries of G.
2. Compute the eigenvalue decomposition $W = V\Lambda V^T$.
3. Let $\Lambda = \text{diag}(\lambda_1, \lambda_2, \ldots, \lambda_n)$ and $\lambda_1 \geq \lambda_2 \geq \ldots \geq \lambda_n$. Supposing λ_r, $1 \leq r \leq n$, is the smallest positive eigenvalue, set $\Lambda' = \text{diag}(\lambda_2, \lambda_3, \ldots, \lambda_r)$, ignoring the largest eigenvalue.
4. Set $U = V_{[2\ldots r]}\Lambda'^{\frac{1}{2}}$, where $V_{[2\ldots r]}$ is the sub-block of U from the second column to the r-th column, inclusive. Then $U_{i\cdot}$ (the i-th row of U) is the embedding, denoted by f_i^e, of face f_i. We denote $\mathcal{F}^e = \{f_i^e\}$.

Figure 4.2: Spectral embedding of mesh faces.

Through this algorithm, the mesh faces are embedded in Euclidean space to facilitate the subsequent clustering operation. Clearly, W encodes the similarities between faces — W_{ij} is inversely (exponentially) proportional to G_{ij} and recall that G_{ij} is the part-aware distance between faces f_i and f_j. In Section 4.2.6, we show that the distance between two embedded faces, f_i^e and f_j^e, is approximately $\sqrt{2 - 2e^{-G_{ij}/2\sigma^2}}$. This implies that if a pair of faces have a large part-aware distance, then their distance in the embedding space is also large. Such a property is the premise for the success of our segmentation algorithm. In the following sections, we study the details of this spectral embedding algorithm.

4.2.1 Affinities

In Section 3.5, we have defined the part-aware distance using the combined graph $\tilde{G}_c$: the distance between two faces is the shortest graph distance between their corresponding nodes in $\tilde{G}_c$. We denote by $G \in \mathbb{R}^{n \times n}$ the distance matrix, where n is the face count of the input mesh $\mathcal{M}$ and G_{ij} is the distance between face f_i and face f_j.

In order to apply spectral clustering, G is first converted to an affinity matrix W. This is typically fulfilled via a kernel function. We choose the exponential kernel function

$$W_{ij} = e^{-G_{ij}/2\sigma^2}. \tag{4.1}$$

σ is called the kernel width, which we discuss how to set in Section 4.2.3. Clearly, W is symmetric, with $0 \leq W_{ij} \leq 1$, and larger distances lead to smaller affinities. We may also use the popular Gaussian kernel [44] instead of the exponential kernel. However, we notice that in practice the exponential kernel tends to produce better segmentation results in our setting, due to its less aggressive attenuation as distance increases.

4.2.2 Analogy to Kernel Principal Component Analysis

In this section, we review kernel principal component analysis (KPCA) [109] and point out how the face embeddings in U (Figure 4.2) relate to KPCA. One can read only the subsequent two paragraphs and the last paragraph of this section to understand the basic idea without knowing the details given in between.

Given a set of points $\mathcal{Z} = \{z_i | z_i \in \mathbb{R}^g\}$, $|\mathcal{Z}| = n$, in Euclidean space, principal component analysis (PCA) [56] computes the eigenvectors of the corresponding covariance matrix $C_{\mathcal{Z}} = \frac{1}{n}\sum_i (z_i - \bar{z})(z_i - \bar{z})^T$, where $\bar{z}$ is the centroid of $\mathcal{Z}$. Such eigenvectors define a new coordinate system whose basis are orthogonal to each other. The leading eigenvectors are the principal directions along which the projections of the points have the largest variations. If the variations along the trailing eigenvectors are sufficiently small, the corresponding dimensions can be discarded without losing too much information of $\mathcal{Z}$, effectively reducing the dimensionality of the data.

KPCA extends PCA by running PCA in a *feature space* $\mathcal{H}$. Conceptually, it first applies to $\mathcal{Z}$ a non-linear mapping $\phi : \mathbb{R}^g \rightarrow \mathcal{H}$. Then PCA is carried out in $\mathcal{H}$ on the point set $\phi(\mathcal{Z}) = \{\phi(z_i) | z_i \in \mathcal{Z}\}$. Since $\mathcal{H}$ can be considered as $\mathbb{R}^h$ [19], where h may be very high, possibly infinite, the non-linear properties of the data points in $\mathcal{Z}$ can be "unfolded" into linear ones. Thus algorithms that work on linear structures, e.g., PCA, can be effectively applied to $\mathcal{Z}$ in $\mathcal{H}$. In practice, the mapping ϕ is never explicitly given; instead it is implicitly specified by the inner products of the points in $\phi(\mathcal{Z})$ that are encoded in a *kernel matrix* $K \in \mathbb{R}^{n \times n}$, where $K_{ij} = \hat{k}(z_i, z_j) = \phi(z_i) \cdot \phi(z_j)$, where $\hat{k}(\cdot)$ is a kernel function, e.g., a Gaussian. Then computations in $\mathcal{H}$ based only on inner products of the data can be efficiently implemented in the original space by replacing inner products with the kernel function $\hat{k}(\cdot)$.

We now review how KPCA is performed. Denoting by $\Phi = [\phi(z_1)|\phi(z_2)|, \dots, |\phi(z_n)]$, then the covariance matrix of $\phi(\mathcal{Z})$, ignoring the normalization by $\frac{1}{n}$, is

$$C_{\phi(\mathcal{Z})} = \Phi\Phi^T = \sum_{i=1}^{n} \phi(z_i)\phi(z_i)^T. \tag{4.2}$$

Note that we assume for now that $\phi(\mathcal{Z})$ is already centered. For the simplicity of notation, in the following we denote $\phi(z_i)$ by φ_i. As we are interested in the eigenvectors of $C_{\phi(\mathcal{Z})}$, we write

$$\rho_m H_m = C_{\phi(\mathcal{Z})} H_m = \sum_{i=1}^{n} (\varphi_i^T H_m)\varphi_i, \tag{4.3}$$

where $\rho_m \geq 0$ is the m-th largest eigenvalue and $H_m \in \mathcal{H} \setminus \{0\}$ is the corresponding eigenvector. Notice that although φ_i may have infinite dimensionality, $C_{\phi(\mathcal{Z})}$ can have at most n positive eigenvalues as there are only n points. From this equation, we see that the principal component H_m can be represented by a linear combination of φ_j,

$$H_m = \sum_{j=1}^{n} \xi^{(j)} \varphi_j, \tag{4.4}$$

with $\xi^{(j)}$ standing for the j-th entry of the coefficient vector ξ. This is an important observation. If we plug H_m into Equation 4.3 and left-multiply both sides by φ^T ($\varphi \in \phi(\mathcal{Z})$), it yields

$$\rho_m \sum_{j=1}^{n} \xi^{(j)} (\varphi \cdot \varphi_j) = \sum_{j=1}^{n} \xi^{(j)} \big(\varphi_j \cdot \sum_{i=1}^{n} \varphi_i\big)(\varphi \cdot \varphi_j), \tag{4.5}$$

or in matrix form

$$\rho_m K \xi = K^2 \xi. \tag{4.6}$$

Since K is symmetric and positive semidefinite, Equation 4.6 is equivalent to

$$\rho_m \xi = K \xi, \tag{4.7}$$

from which we see that ξ is simply an eigenvector of K. Let $\mu_1 \geq \ldots \geq \mu_m \geq \ldots \geq \mu_n \geq 0$ be the eigenvalues of K and $\Xi = [\Xi_1|\Xi_2|\ldots|\Xi_n]$ contains the corresponding eigenvectors, we have $H_m = \sum_j \Xi_m^{(j)} \varphi_j$ from Equation 4.4. Intuitively, the entries of Ξ_m are the coefficients of the linear combination of φ_j's that represents the m-th principal component, H_m, of $\phi(\mathcal{Z})$. Therefore the projection of any point φ_i on H_m is

$$H_m \cdot \varphi_i = \big(\sum_j^n \Xi_m^{(j)} \varphi_j\big) \cdot \varphi_i = \sum_j^n \Xi_m^{(j)} (\varphi_j \cdot \varphi_i) = \sum_j^n \Xi_m^{(j)} K_{ji} = K_{\cdot i}^T \Xi_m = K_{i \cdot} \Xi_m, \tag{4.8}$$

with $K_{\cdot i}$ and $K_{i \cdot}$ being the i-th column and i-th row of K, respectively. If we require H_m to be normalized, it implies

$$1 = H_m \cdot H_m = \sum_j^n \Xi_m^{(j)} \varphi_j \cdot \sum_j^n \Xi_m^{(j)} \varphi_j = \sum_{i,j=1}^n \Xi_m^{(i)} \Xi_m^{(j)} (\varphi_i \cdot \varphi_j) = \Xi_m \cdot K \Xi_m = \mu_m (\Xi_m \cdot \Xi_m). \tag{4.9}$$

Therefore we should normalize $\Xi_m \leftarrow \Xi_m / \sqrt{\mu_m}$ and Equation 4.8 translates into

$$H_m \cdot \varphi_i = K_{i \cdot} \Xi_m / \sqrt{\mu_m} = (\mu_m \Xi_m)_i / \sqrt{\mu_m} = \sqrt{\mu_m} \Xi_m^{(i)}. \tag{4.10}$$

Based on all above discussions, we are able to draw the similarity between KPCA and spectral embedding, which has been previously noted in [13]. Assuming that the affinity matrix W has only non-negative eigenvalues, we denote its eigenvalue decomposition by $W = V \Lambda V^T$ and set $U' = V \Lambda^{\frac{1}{2}}$, namely,

$$U'_{im} = \sqrt{\lambda_m} V_m^{(i)}. \tag{4.11}$$

Notice that the right sides of Equations 4.10 and 4.11 take the same form. Therefore, if we consider W as the kernel matrix K, for the points in $\mathcal{H}$ induced by W, U'_{im} can be viewed as the projection of the i-th point onto the m-th principal component. More specifically, if we assume (a) the points in the feature space $\mathcal{H}$ induced by W are centered, and (b) W is positive semidefinite (since W is symmetric, this implies that all its eigenvalues are non-negative), the rows of U' are essentially the embeddings via KPCA induced by W. Unfortunately, the above two conditions are not guaranteed for the affinity matrix W produced in the first step of our algorithm in Figure 4.2. However, we show in Section 4.2.4 and Section 4.2.5 how our face embeddings in U (Figure 4.2) have already implicitly met these two conditions. Let's recapitulate the property of the embeddings in U in the following observation:

Observation 4.1. *The affinity matrix W induces n points in a high dimensional feature space $\mathcal{H}$. $U_{i \cdot}$ (the i-th row of U) are the embedded coordinates for face f_i in the coordinate system whose basis are the principal components of the induced points in $\mathcal{H}$.*

4.2.3 Kernel Width

The kernel width σ in Equation 4.1 plays an important role in spectral clustering. Automatically setting σ to achieve robust clustering results against all kinds of input data is challenging and manual tuning is typically required, although automatic methods exist [37, 83]. We do not intend to solve this problem in general; instead, we simply find a way to set σ to suit mesh segmentation in our application.

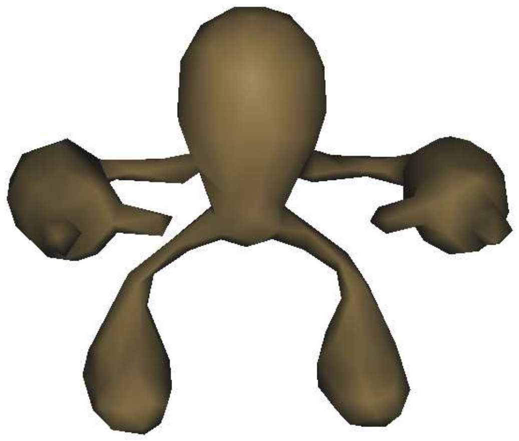

(a) enforcer model

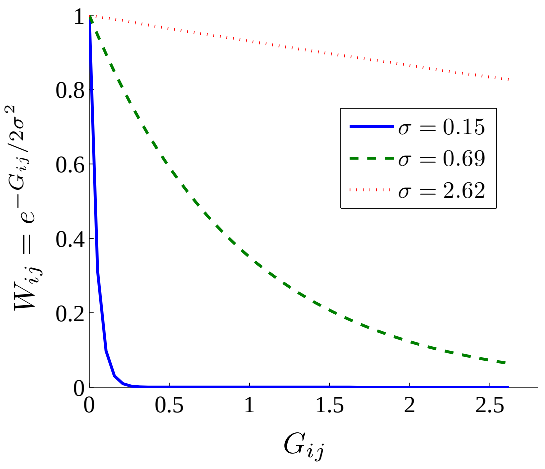

(b) kernel functions with different σ

Figure 4.3: Exponential kernel functions with different kernel widths tested on the enforcer model with 600 faces.

Take the model shown in Figure 4.3(a) for example. We compute the distance matrix G for its faces. The average and maximum distances are 0.48 and 2.62, respectively. We plot in Figure 4.3(b) three kernel functions with different kernel widths. From plot (b), we see that if σ is too large ($\sigma = 2.62$, the maximum distance), W_{ij}'s are squeezed into a narrow band near 1, sacrificing the contrast between different distances. In the extreme case, if $\sigma = \infty$, $W = \mathbf{1}\mathbf{1}^T$ and all the embeddings reduce to a single point. On the other hand, if σ is too small ($\sigma = 0.15$), W_{ij} vanishes too quickly, making all faces far apart in the embedding space unless they are sufficiently close on the surface. When $\sigma = 0$, W turns into an identity matrix, in which case all the embeddings in $\mathcal{H}$ are equally far away from each other.

Either too small or too large, σ produces a face embedding with undesirable distribution, imperiling the segmentation quality. We choose to set σ based on the average distance which provides a good clue for the right scale of σ. More specifically, we set σ to the square root of the average distance in G. For example, the green curve ($\sigma = 0.69$) in plot (b) depicts the kernel function when σ is set in such a way. This way, the function spans the range of affinity values in a more meaningful manner: the changes of G_{ij} gradually contribute less changes to W_{ij} as G_{ij} increases. We have found that such a mapping works well for our application in general.

4.2.4 Affinity Matrix Centering

In Section 4.2.2, one of our assumptions made for W is that the induced point set $\phi(\mathcal{Z})$ in $\mathcal{H}$ is already centered. In practice, however, this assumption does not normally hold. Note also that since the coordinates of $\phi(\mathcal{Z})$ are unknown, it is impossible to center them explicitly. Fortunately, it is shown by Schölkopf et al. [109] that the centering can be implicitly implemented by converting W to $\bar{W}$:

$$\bar{W} = (I - \frac{1}{n}\mathbf{1}\mathbf{1}^T)W(I - \frac{1}{n}\mathbf{1}\mathbf{1}^T). \tag{4.12}$$

The major drawback of computing $\bar{W}$ is the high computational cost when the size of W is large. As we will see in Chapter 5, the full W is also not available for centering due to sub-sampling, which is necessary for handling large meshes. In practice, we make the following observation:

Observation 4.2. *Provided that the kernel width σ is sufficiently large, the eigenvalues and eigenvectors of W well approximate, with a shift, those of $\bar{W}$. Specifically, suppose $\lambda_1 \geq \lambda_2 \geq \ldots$ are the eigenvalues of W and $V_1, V_2, \ldots$ are the corresponding eigenvectors; $\bar{\lambda}_1 \geq \bar{\lambda}_2 \geq \ldots$ are the eigenvalues of $\bar{W}$ and $\bar{V}_1, \bar{V}_2, \ldots$ are the corresponding eigenvectors, we have $\lambda_2 \approx \bar{\lambda}_1, \lambda_3 \approx \bar{\lambda}_2, \ldots$ and $V_2 \approx \bar{V}_1, V_3 \approx \bar{V}_2, \ldots$.*

This observation enables us to avoid the centering operation; we can simply ignore the largest eigenvector of W and use the subsequent eigenvectors. We provide an explanation and an experiment to attest to this observation.

Since $W_{ij} = \phi(z_i)^T\phi(z_j)$ and $W_{ii} = 1$, each $\phi(z_i)$ has unit length in the feature space and W_{ij} is simply the cosine of the angle between vectors $\phi(z_i)$ and $\phi(z_j)$. Geometrically, this implies that given any vector $\phi(z_i)$, $\forall j \neq i, \phi(z_j)$ lies inside a cone, which is rooted at the origin with an opening angle of $2\theta_i$ and its axis along vector $\phi(z_i)$, where θ_i is determined

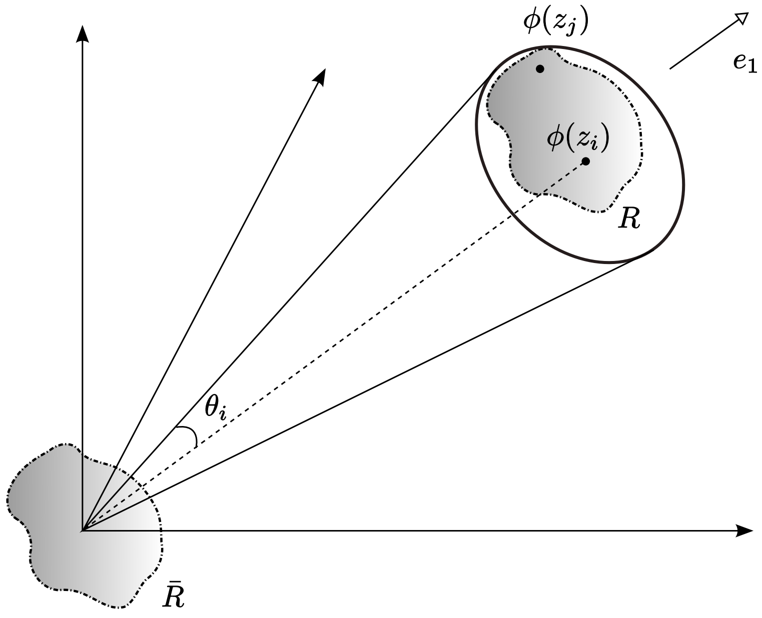

Figure 4.4: Distribution of affinity-implied points in feature space.

by the smallest entry W_{it} of the i-th row of W. If σ is sufficiently large (see Equation 4.1), W_{it} is close to 1 and, accordingly, θ_i is small. Such a configuration is depicted in Figure 4.4. Each point $\phi(z_i)$ is associated with a cone and the *intersection* of these cones gives a region, R, in which all the points lie. In the figure, R is the shaded region enclosed by the dashed curve. Note that the cone and the region R are enlarged for illustration purpose. If $\phi(\mathcal{Z})$ were centered, the region R would have moved to the place indicated by $\bar{R}$.

We show that the principal components of the points in $\bar{R}$ are approximately the same as the principal components of the points in R, only shifted by one position. Recall that $C_{\phi(\mathcal{Z})}$ (Equation 4.2) is the covariance matrix of $\phi(\mathcal{Z})$. Note that now the points are not centered yet. The largest eigenvector $\mathbf{e}_1$ of $C_{\phi(\mathcal{Z})}$ is the vector $\mathbf{p}$ that maximizes the term $\sum_i ||\mathbf{p}^T\phi(z_i)||^2$. Since all $\phi(z_i)$'s have unit length and small angles between each other (suppose σ is sufficiently large), the region R is small and the distance from any point inside R to the origin is about 1. So, $\mathbf{e}_1$ is roughly a constant vector pointing from the origin toward the centroid of R to maximize the variance, as illustrated in Figure 4.4. With the same reasoning, R is "thin" along the direction of $\mathbf{e}_1$. Consequently, the space spanned by $\phi(\mathcal{Z})$ is close to the null space of $\mathbf{e}_1$. The subsequent eigenvectors $\{\mathbf{e}_2, \mathbf{e}_3, \ldots\}$ of $C_{\phi(\mathcal{Z})}$, in the null space of $\mathbf{e}_1$, are then a good approximation to the principal components which characterize the intrinsic distribution of $\phi(\mathcal{Z})$. On the other hand, if $\phi(\mathcal{Z})$ is centered (denoted by $\bar{\phi}(\mathcal{Z})$), R translates to $\bar{R}$. We denote the corresponding centered covariance matrix by $C_{\bar{\phi}(\mathcal{Z})} = \bar{\Phi}\bar{\Phi}^T$, where $\bar{\Phi} = [\bar{\phi}(z_1)|\bar{\phi}(z_2)|, \dots, |\bar{\phi}(z_n)]$, and let $\{\bar{\mathbf{e}}_1, \bar{\mathbf{e}}_2, \dots\}$ be the largest eigenvectors of $C_{\bar{\phi}(\mathcal{Z})}$. Since $\phi(\mathcal{Z})$ and $\bar{\phi}(\mathcal{Z})$ have the same *intrinsic* distribution and are only displaced by a translation, they should have the same principal components and variances, namely we have $\bar{\mathbf{e}}_1 \approx \mathbf{e}_2$, $\bar{\mathbf{e}}_2 \approx \mathbf{e}_3 \dots$ and $\bar{\lambda}_1 \approx \lambda_2$, $\bar{\lambda}_2 \approx \lambda_3 \dots$, where the approximation is exact if the space spanned by $\phi(\mathcal{Z})$ coincides with the null space of $\mathbf{e}_1$.

Finally, we show why V_2, the second largest eigenvector of W, is a good approximation of $\bar{V}_1$, the largest eigenvector of $\bar{W}$. The same relation between succeeding eigenvectors can be similarly proved. Since $\bar{W} = \bar{\Phi}^T\bar{\Phi}$ and $C_{\bar{\phi}(\mathcal{Z})} = \bar{\Phi}\bar{\Phi}^T$, $\bar{W}$ and $C_{\bar{\phi}(\mathcal{Z})}$ have the same eigenvalues and $\bar{\Phi}^T\bar{\mathbf{e}}_1$ is the largest eigenvector of $\bar{W}$, i.e. $\bar{V}_1 = \bar{\Phi}^T\bar{\mathbf{e}}_1$. Similarly, $V_2 = \Phi^T\mathbf{e}_2$. Therefore, we only need to show that $\bar{\Phi}^T\bar{\mathbf{e}}_1 \approx \Phi^T\mathbf{e}_2$. Let us write $\psi = \frac{1}{n}\sum_i \phi(z_i)$, then we have $\Phi^T = \bar{\Phi}^T + \mathbf{1}\psi^T$. It is easy to derive

$$\begin{aligned} \Phi^T\mathbf{e}_2 &= (\bar{\Phi}^T + \mathbf{1}\psi^T)\mathbf{e}_2 \\ &= \bar{\Phi}^T\mathbf{e}_2 + \mathbf{1}\psi^T\mathbf{e}_2 \\ &\approx \bar{\Phi}^T\bar{\mathbf{e}}_1 + \mathbf{0} \\ &= \bar{\Phi}^T\bar{\mathbf{e}}_1. \end{aligned} \tag{4.13}$$

The approximation in Equation 4.13 is because $\bar{\mathbf{e}}_1 \approx \mathbf{e}_2$ (shown above) and $\psi^T\mathbf{e}_2 \approx \mathbf{0}$ ($\psi \approx \mathbf{e}_1$ and $\mathbf{e}_1 \perp \mathbf{e}_2$). This concludes our explanation.

Figure 4.5 provides an experimental comparison between V_2 and $\bar{V}_1$. The kernel matrices W and $\bar{W}$ are computed again from the enforcer model in Figure 4.3. As we can see from the top plot, the approximation quality is high when σ is sufficiently large. From the bottom plot, it is also observed that the slight difference between V_2 and $\bar{V}_1$ is caused by a small translation. This is easily explained with Equation 4.13. Since $\psi^T\mathbf{e}_2 \approx \mathbf{0}$, we have $\mathbf{1}\psi^T\mathbf{e}_2 \approx \epsilon\mathbf{1}$ (ϵ is close to zero), hence the translation. Be aware that a translation between the eigenvectors of W and $\bar{W}$ causes almost no damage to the embedding as the relative positions of the embeddings are preserved.

With this being said, our algorithm can simply make σ sufficiently large and use the eigenvectors/eigenvalues of W except for the first one to derive the spectral embedding U, so that the points in the feature space are implicitly centered. This is why the embedding algorithm in Figure 4.2 ignores the first eigenvector of W. Note that however, we should not make σ arbitrarily large; recall that in Section 4.2.3 we have opted to set σ to the square

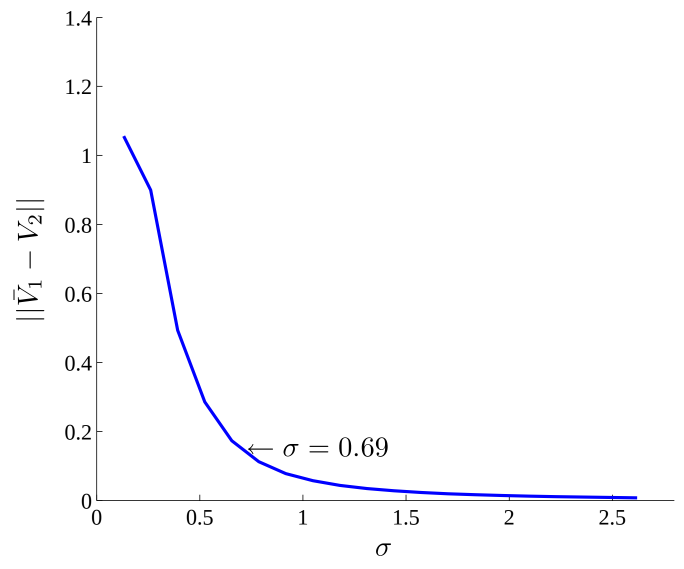

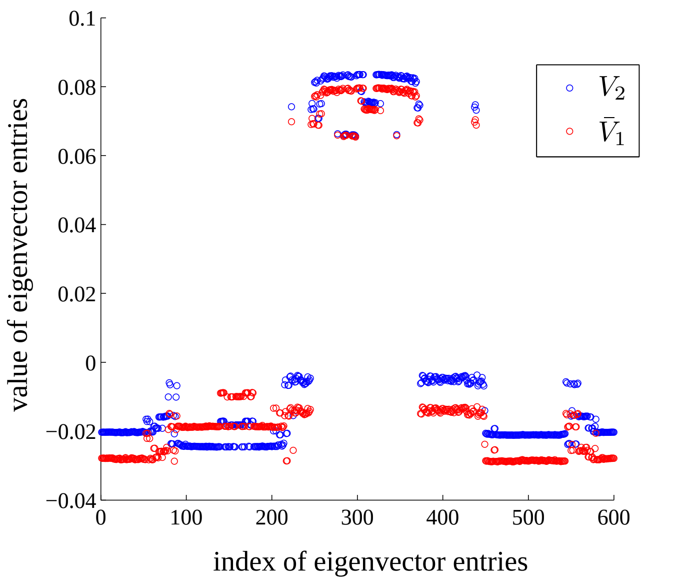

Figure 4.5: Influence of kernel width to the approximation quality for V_2 and $\bar{V}_1$. The top plot shows that $||\bar{V}_1 - V_2||$ decreases quickly while the kernel width σ increases, where $\sigma = 0.69$ is the square root of the average distance in G. The bottom plot shows the two eigenvectors when $\sigma = 0.69$, where $||\bar{V}_1 - V_2|| = 0.15$, $\bar{\lambda}_1 = 90.27$ (the first eigenvalue of $\bar{W}$), and $\lambda_2 = 88.15$ (the second eigenvalue of W). We see that $\bar{\lambda}_1 \approx \lambda_2$ and $\bar{V}_1 \approx V_2$.

root of the average distance. Practically this is sufficiently large for the purpose of avoiding centering W, which has been verified by the empirical example from Figure 4.5.

4.2.5 Positive-Semidefiniteness

In Section 4.2.2, we have also assumed that W is positive semidefinite in order for the KPCA analogy to apply. This is because the kernel matrix K must be positive semidefinite, which is necessary to derive Equation 4.7 and Equation 4.10. This requirement can be explained from another perspective as well. Recall that $K = \Phi^T\Phi$ and $C_{\phi(\mathcal{Z})} = \Phi\Phi^T$. $C_{\phi(\mathcal{Z})}$ is positive semidefinite, since given any vector $x \in \mathcal{H}$, $x^T C_{\phi(\mathcal{Z})} x = x^T \Phi\Phi^T x = (\Phi^T x)^T(\Phi^T x) = \|\Phi^T x\|^2 \geq 0$. In addition, it is easy to prove that K and $C_{\phi(\mathcal{Z})}$ have the same eigenvalues[1]. Therefore K is positive semidefinite.

In reality, however, the W we derive is not guaranteed to be positive semidefinite. Theoretically speaking, we can deal with this problem by converting W to $\hat{W}$ which is positive semidefinite. Let $W = V\Lambda V^T$ be the eigenvalue decomposition, we can also write it as

$$W = \sum_{i=1}^{n} \lambda_i V_i V_i^T, \tag{4.14}$$

where λ_i is the i-th largest eigenvalue and V_i is the corresponding eigenvector. Supposing only the leading r eigenvalues, $\lambda_1, \ldots, \lambda_r$, are greater than 0, we set

$$\hat{W} = \sum_{i=1}^{r} \lambda_i V_i V_i^T, \tag{4.15}$$

which is obviously positive semidefinite. As we are essentially interested in the eigenvalues and eigenvectors of $\hat{W}$, we may simply take the positive eigenvalues of W and their eigenvectors to derive the face embeddings without constructing $\hat{W}$ explicitly. This is reflected in the embedding algorithm in Figure 4.2.

With this approach, we need to make sure that not too much information is lost by discarding the negative eigenvalues and eigenvectors. It is well known in numerical linear algebra that for a symmetric matrix M with eigenvalue decomposition $M = \sum_{i=1}^{n} \hat{\lambda}_i \hat{V}_i \hat{V}_i^T$, where the $\hat{\lambda}_i$'s are the eigenvalues sorted in descending order by their magnitude and $\hat{V}_i$'s are the respective eigenvectors, the best rank r matrix approximating M (in the sense of

[1]For any eigenvalue λ and the corresponding eigenvector v of K, λ and Φv are an eigenvalue and the corresponding eigenvector of $C_{\phi(\mathcal{Z})}$.

the Frobenius norm) is $\sum_{i=1}^{r} \hat{\lambda}_i \hat{V}_i \hat{V}_i^T$. Comparing Equation 4.14 with Equation 4.15, we see that if W has only a few negative eigenvalues with relatively small magnitudes, only a small amount of information will be lost when converting W to $\hat{W}$.

Empirically, the affinity matrix W we produce from the distance matrix G via an exponential kernel is either positive semidefinite or sufficiently close to be, in the sense that the number of negative eigenvalues of W is relatively small and their magnitudes are negligible compared with those of positive eigenvalues. Again let's take the enforcer model as an example, for which W is obtained with the kernel width $\sigma = 0.69$. The eigenvalues of W are $88.15, 75.29, 37.65, 26.40, 6.73, \ldots, 0, \ldots, -0.029, -0.034$; the largest eigenvalue is ignored as W is not centered (see Section 4.2.4). Only 16% of the eigenvalues are negative, which share about 0.15% of the energy of the entire spectrum.

4.2.6 Distance between Embeddings

Let's examine how distances between embedded faces relate to their affinities. Since $\hat{W}$ in Equation 4.15 is strictly positive semidefinite and centering in $\mathcal{H}$ does not affect the distances between embedded faces, we can compute the distance between any two embedded faces $\phi(f_i)$ and $\phi(f_j)$ in $\mathcal{H}$ as

$$\begin{aligned} ||\phi(f_i) - \phi(f_j)|| &= \sqrt{\left(\phi(f_i) - \phi(f_j)\right)^T \left(\phi(f_i) - \phi(f_j)\right)} \\ &= \sqrt{\phi(f_i)^T\phi(f_i) + \phi(f_j)^T\phi(f_j) - 2\phi(f_i)^T\phi(f_j)} \\ &= \sqrt{\hat{W}_{ii} + \hat{W}_{jj} - 2\hat{W}_{ij}} \\ &\approx \sqrt{W_{ii} + W_{jj} - 2W_{ij}} \\ &= \sqrt{1 + 1 - 2W_{ij}} \\ &= \sqrt{2 - 2e^{-G_{ij}/2\sigma^2}}, \end{aligned} \tag{4.16}$$

where the approximation step is due to the fact that W is close to be positive semidefinite as discussed in Section 4.2.5. Through this equation, we observe that the distances between embedded faces are exponentially proportional to their distances in G, and the rank order of distances is preserved as well. Since $U_{i\cdot}$ (Figure 4.2) is the dimensionality-reduced embedding of $\phi(f_i)$ in $\mathcal{H}$ via PCA and PCA embedding does not change the distances between entities, we have

$$\|U_{i\cdot} - U_{j\cdot}\| \approx \sqrt{2 - 2e^{-G_{ij}/2\sigma^2}}. \tag{4.17}$$

We also take the enforcer model to verify Equation 4.17 empirically. To this end, we denote $d^e_{ij} = \|U_{i\cdot} - U_{j\cdot}\|$ and $d^{\mathcal{H}}_{ij} = \sqrt{2 - 2e^{-G_{ij}/2\sigma^2}}$. For any faces f_i and f_j, the discrepancy between d^e_{ij} and $d^{\mathcal{H}}_{ij}$ is defined as $2|d^e_{ij} - d^{\mathcal{H}}_{ij}|/(d^e_{ij} + d^{\mathcal{H}}_{ij})$. Then the average discrepancy over all pairs of faces gives a quantitative estimation about the accuracy of Equation 4.17. For the enforcer model, the average discrepancy is only 1.23%.

4.2.7 Further Discussions

Our spectral embedding algorithm serves to transform the distances encoded in G to Euclidean embeddings of mesh faces for the subsequent K-means clustering operation. Theoretically, it is possible to run a K-means algorithm simply based on G without explicit embeddings, for example, using the method from [59]. Nonetheless, such a method is inefficient and all the entries of G have to be known. When the size of a mesh is large, even computing the entire G itself is already not affordable. In such cases, we show (Chapter 5) how to use only a few rows of G to derive face embeddings. With an Euclidean embedding, K-means can be performed efficiently.

The distances between embedded faces are approximately $\sqrt{2 - 2e^{-G_{ij}/2\sigma^2}}$. A large G_{ij} induces a large embedding distance and vice versa. Note that this distance relation is monotone and non-linear. By setting the kernel width σ and using the eigenvectors appropriately, such a distance relation is accurately enforced by our embedding algorithm. In other words, all the distances encoded in G are consistently reconstructed in the embedding space governed by this relation. Also, the contrast of the distances in G is well preserved (see Section 4.2.3); this is important for achieving high quality segmentation results. On the other hand, if we apply the metric Multi-Dimensional Scaling [27] based on G to derive face embeddings, inferior segmentation results are shown by our experiments. This is because G in general has relatively large negative eigenvalues, which defies the positive semidefinite requirement in order for MDS to apply meaningfully.

4.3 K-means Clustering

So far, we have obtained the spectral embedding $\mathcal{F}^e = \{f^e_i\}^n_{i=1}$ for the faces of the input mesh $\mathcal{M}$. The embedding coordinate for face f_i is denoted by $f^e_i = U_{i\cdot}$, and the dimensionality is at most $n-1$, which is achieved when W is positive definite (note that we discard the first eigenvalue/eigenvector). In the embedding space, the face distances reflect the part-aware

1. Assuming $k \leq r-1$, reduce the dimensionality of $\mathcal{F}^e$ by keeping only the first k columns of U. Recall that r is the number of positive eigenvalues of W (Figure 4.2).
2. Initiate a proxy set $\mathcal{P} = \{p_i\}_{i=1}^k$, where $\mathcal{P} \subset \mathcal{F}^e$. Each p_i represents cluster $\mathcal{F}_i^e$ and all p_i's are mutually farthest apart in the embedding space.
3. *Element assignment*: for each f^e, assign it to the cluster $\mathcal{F}_i^e$, where $i = \text{argmin}_{1 \leq j \leq k} \|f^e - p_j\|$. Namely, a face is assigned to the closest proxy.
4. *Proxy fitting*: refine each proxy p_i to the centroid of cluster $\mathcal{F}_i^e$.
5. Repeat step 3 and step 4 until $\mathcal{P}$ is stable.

Figure 4.6: K-means clustering in embedding space.

distances in G. The next step is to apply K-means clustering to $\mathcal{F}^e$ to obtain the actual segmentation result.

The general framework of a K-means algorithm has been briefed in Section 2.2.1 when variational segmentation approaches are discussed. We formally describe the K-means algorithm for our application in the following.

Given the face embedding $\mathcal{F}^e$, we seek a clustering $\Theta = \{\mathcal{F}_i^e\}_{i=1}^k$, where $\bigcup_{i=1}^k \mathcal{F}_i^e = \mathcal{F}^e$ and $\mathcal{F}_i^e \bigcap \mathcal{F}_{j,j\neq i}^e = \emptyset$, such that the cost function

$$cost\left(\{\mathcal{F}_i^e\}_{i=1}^k\right) = \sum_{i=1}^k \left(\sum_{f_j^e \in \mathcal{F}_i^e} \|f_j^e - \bar{\mathcal{F}}_i^e\| \right) \tag{4.18}$$

is minimized, where k is the number of segments given by a user and $\bar{\mathcal{F}}_i^e$ is the centroid of cluster $\mathcal{F}_i^e$. The term in the bracket on the right side of the equation measures the intra-cluster cost. If every embedding is close to the centroid of its cluster, the cluster is tight and the intra-cluster cost is low. Figure 4.6 demonstrates how the K-means is performed in our algorithm. Intuitively, the algorithm finds an approximate solution (a local minimum) to Equation 4.18 by iteratively reducing intra-cluster costs. In each iteration, a face is assigned to its closest proxy and each proxy is refined to its cluster centroid. These two steps alternate until all the proxies are stable, implying that a local minimum is reached.

When the K-means algorithm converges, each cluster $\mathcal{F}_i^e$ is tight and the distances between the centroids of different clusters are large. Such clusters are likely to correspond to the parts of the input mesh $\mathcal{M}$.

4.3.1 Dimensionality Reduction

The initial embedding of $\mathcal{F}^e$, derived as in Figure 4.2, has a dimensionality of at most $n-1$. As discussed in Section 4.2.5, we may discard those dimensions whose corresponding eigenvalues are non-positive. However, the resulting dimensionality could still be high, especially when n is large. High embedding dimensionality poses two computational bottlenecks: one for the eigenvalue decomposition of W and the other for the K-means clustering.

We reduce the dimensionality of an embedding by dropping the trailing columns of U. According to the analogy to KPCA, this is equivalent to the standard dimensionality reduction via PCA, but carried out in the feature space $\mathcal{H}$. In practice, the embedding dimensionality is reduced rather aggressively — we only keep the first k columns of U. The benefits are twofold. First, as k is typically small (less than 15 as a model usually does not contain too many parts), we only need to compute the first $k+1$ eigenvectors of W. This can be efficiently carried out using the ARPACK [70] package, which is designed to solve large scale eigenvalue problems with capability to compute only leading or trailing eigenvectors. Secondly, discarding the trailing eigenvectors helps get rid of high "frequency" information. This means that the resulting embeddings would attempt to preserve only the distances between prominent clusters, while the distances between intra-cluster points are ignored. This makes the K-means algorithm work more favorably to extract prominent clusters without being distracted by intra-cluster distances.

4.3.2 Proxy Initialization

Our K-means algorithm is subject to local minima, and the clustering result has much to do with the seed proxy set $\mathcal{P}$. Although finding the global optimum for a K-means problem is known to be NP-hard, it is possible to apply certain heuristics to improve the clustering quality. One simple way is to run K-means with random initial proxies for multiple times and choose the result for which Equation 4.18 is minimized. Another way is to randomly select a subset of the original data, run K-means on the selected data, and utilize the preliminary clustering result to initialize the proxies for the final clustering performed on the full data.

However, both methods do not make full use of the information encoded in the embedding. Since we want the resulting clusters to correspond to the mesh parts, it is natural to pick a seed proxy from each part. As our part-aware metric imposes large distances between parts and the distances are well preserved in the embedding space, it implies that the seed proxies are likely to be mutually far apart. Therefore, we adopt a max-min scheme to find such proxies. We select the first two proxies that are farthest away in the embedding space. Then each subsequent proxy is inserted such that it maximizes the smallest distance to the previously chosen proxies. We have found that such a scheme effectively alleviates the local minima problem of our K-means algorithm.

4.3.3 Boundary Enhancement

Nearby faces on a mesh face should be close in the embedding space because we derive distances in G as graph distances, which are continuous. However, faces in each cluster output by the K-means algorithm are not guaranteed to form a single connected region (referred to as a component in this context) on a mesh surface, although in practice they often do. Rarely, few faces along a part boundary might be disconnected from the core region. The boundaries between the parts could also present some local artifacts, including jaggedness or slight deviation from the intended boundary positions. We fix such problems in a post-processing stage.

We adopt a functional optimization framework that considers spatial coherence. This idea is developed by Boykov et al. [17] and used for meshes [112]. Recall that Θ is the clustering result from the K-means algorithm. It can also be considered as a labeling of faces with respect to the converged proxies. Let's denote the converged proxies by $\mathcal{P}'$. Our goal is then to come up with a refined clustering/labeling Θ' with respect to $\mathcal{P}'$ such that the following functional is minimized:

$$E(\Theta') = E_{data}(\Theta') + \mu E_{smooth}(\Theta'). \tag{4.19}$$

$E_{data}(\Theta')$ is designed to respect Θ, and $E_{smooth}(\Theta')$, weighted by μ, is used to enhance part boundaries.

Given a face f_i, suppose it is labeled p_{f_i} in Θ', where $p_{f_i} \in \mathcal{P}'$. We define function

$$h_1(f_i, p_{f_i}) = -\log\left(\frac{1/d(f_i, p_{f_i})}{\sum_{j=1}^{k}\big(1/d(f_i, p_{f_j})\big)}\right),$$

where $d(\cdot)$ denotes the Euclidean distance between the embedding of a face and a proxy. Intuitively, $h_1(\cdot) \in (0, +\infty)$ measures how "bad" it is if f_i is clustered to p_{f_i}. Specifically, if f_i's embedding, f_i^e, is actually closest to p_{f_i} after our K-means clustering, $h_1(f_i, p_{f_i})$ would be small and vice versa. We define $E_{data}(\Theta') = \sum_{i=1}^{n} h_1(f_i, p_{f_i})$; therefore minimizing E_{data} means to honor the overall result from the previous K-means clustering.

The smooth term is defined as $E_{smooth}(\Theta') = \sum_{(f_i,f_j)\in\mathcal{N}} h_2(f_i, f_j, p_{f_i}, p_{f_i})$, where $\mathcal{N}$ is the set of pairs of adjacent faces (sharing a common edge). $E_{smooth}(\Theta')$ is a measure about part boundaries, providing $h_2(\cdot)$ does not vanish only when $p_{f_i} \neq p_{f_j}$. Specifically, we define

$$h_2(f_i, f_j, p_{f_i}, p_{f_i}) = \begin{cases} l(e_{ij})\big(1 - \text{weight}(e_{ij})\big) & p_{f_i} \neq p_{f_j} \\ 0 & p_{f_i} = p_{f_j} \end{cases},$$

where $l(e_{ij})$ is the length of the common edge e_{ij} of f_i and f_j, normalized by the maximum edge length over the entire mesh surface, and weight(e_{ij}) is the mapped angular weight (Section 3.3) of e_{ij}, defined as

$$\text{weight}(e_{ij}) = \log\left(\nu \tilde{G}_a(i,j) + 1\right) / \log(\nu + 1). \tag{4.20}$$

Via this logarithmic mapping [112], with ν controlling the mapping strength, the influences of small angular weights are enhanced. Such a mapping helps improve the boundary quality in our experiments. Intuitively, minimizing $E_{smooth}(\Theta')$ implies to favor a short part boundary consisting of concave edges. In our application, we set $\mu = 0.3$ and $\nu = 10$.

Equation 4.19 is minimized approximately via a minimum graph cut problem [17]. By subjecting Θ to such a smoothing procedure, the refined clustering Θ' induces short boundaries across concave regions. Connected components are also implicitly ensured as short boundaries are preferred; we have never encountered a part with multiple components in our experiments.

4.4 Experimental Results

Complexity Recall that the input mesh $\mathcal{M}$ has n faces. Building the distance matrix G from $\tilde{G}_c$ requires running Dijkstra's algorithm for each node, which has a complexity of $O(n^2 \log n)$. Converting G to W requires $O(n^2)$. Since we only need a small number of leading eigenvalues and eigenvectors, we avoid the high complexity of computing the full eigenvalue decomposition of W, which is $O(n^3)$. Using the ARPACK package [70], the leading eigenvectors are computed by a variant of the Lanczos process called the Implicitly Restarted Lanczos Method. With reasonable accuracy settings suitable for our application, such a method achieves much higher empirical efficiency than constructing G. Since the K-means algorithm converges quickly, its complexity in practice also does not exceed $O(n^2)$. Therefore, the overall complexity of our algorithm is $O(n^2 \log n)$, dominated by the construction of the distance matrix G.

Overview of experiments We demonstrate how the algorithm works on a simple model, and set different numbers of segments to test how it performs. We run another two experiments to show the effectiveness of the VSI-distance. Finally, our algorithm is tested on a number of additional models.

It is worth pointing out that in all our experiments, including those in Section 5.6, the graph $\tilde{G}_c$ is constructed using a fixed set of parameters unless stated otherwise, with $\alpha = 0.01$, $\beta = 0.195$, and $\gamma = 0.795$ (see Section 3.5) to emphasize the VSI distance. The geodesic distance is not completely discarded, since it helps produce smoother part boundaries and prevent undesirably large parts from being formed as well.

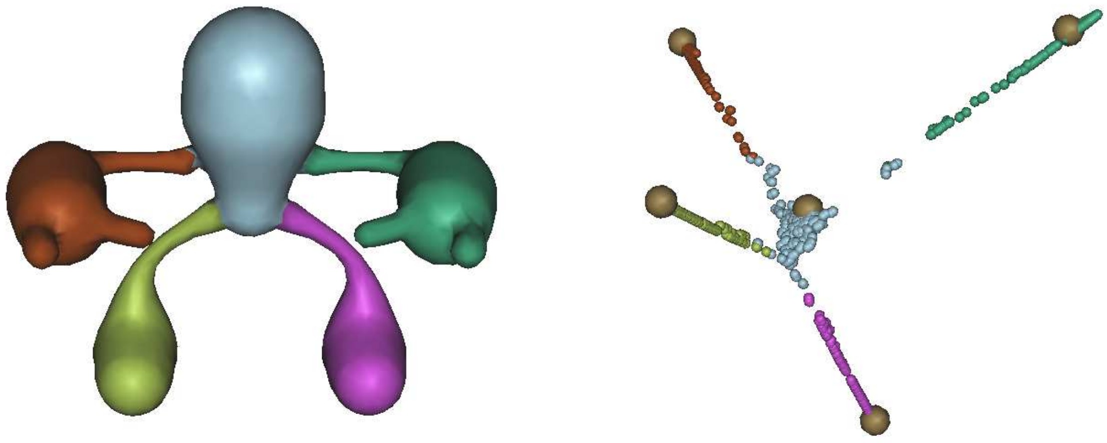

(a) segmentation on the mesh (b) clustering in the embedding space

Figure 4.7: Segmentation result with 5 parts for the enforcer model. In plot (b), the embeddings are rendered using the first three dimensions, where the large spheres indicate the mutually farthest seed proxies for the K-means clustering algorithm.

We first test our algorithm on a enforcer model with 4000 faces, which has a clear part structure. We set $k = 5$. As shown in Figure 4.7 (a), intuitive parts are obtained. In Figure 4.7 (b), the clustering result in the embedding space is given. In the embedding

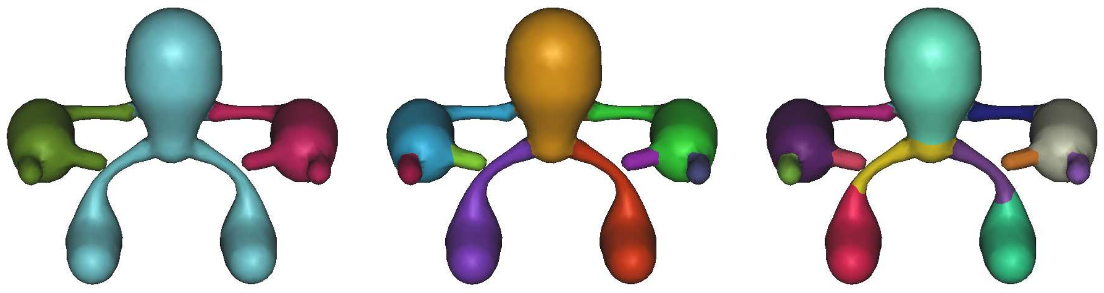
(a) 3 parts (b) 9 parts (b) 13 parts

Figure 4.8: Segmentation results for the enforcer model with different numbers of segments.

space, we see that the points (gray-blue) corresponding to the body sit in the middle of the four limb-parts; this is in accordance with the part-aware distance from the graph $\tilde{G}_c$. The five large brownish spheres mark the seed proxies for the K-means algorithm. They are selected as the embeddings that are mutually farthest apart as described in Section 4.3.2. From this example, we observe that such an initialization scheme does tend to locate proxies from different parts, hence improving the robustness of our K-means clustering.

We also set $k = 3, 9, 13$ for the enforcer model and the segmentation results are shown in Figure 4.8, which are intuitive. Although we did not perform hierarchical decomposition explicitly, by changing the number of segments, we note that the algorithm tends to segment in a hierarchical manner. Having such a hierarchical segmentation property is deemed as a merit of our algorithm.

Figure 4.9 provides a comparative example as to how the distances in $\tilde{G}_c$ are reflected in the embedding, which in turn affects the clustering result. For illustration purpose, we consider two cases: one with the geodesic distance only and the other with our part-aware distance. Plot (a) shows the segmentation on the mesh (from both front and back views) and the clustering in the embedding. Since the geodesic distance does not accurately characterize the parts, the resulting parts straddle across the intended boundaries between the limbs and the body. Plot (b) shows the results obtained via the part-aware distance. Clearly, we see that the parts are tighter and better clustered in the embedding space, hence the better segmentation result on the mesh. Plot (c) illustrates how the boundary enhancement operation (Section 4.3.3) helps fix local artifacts along the part boundaries.

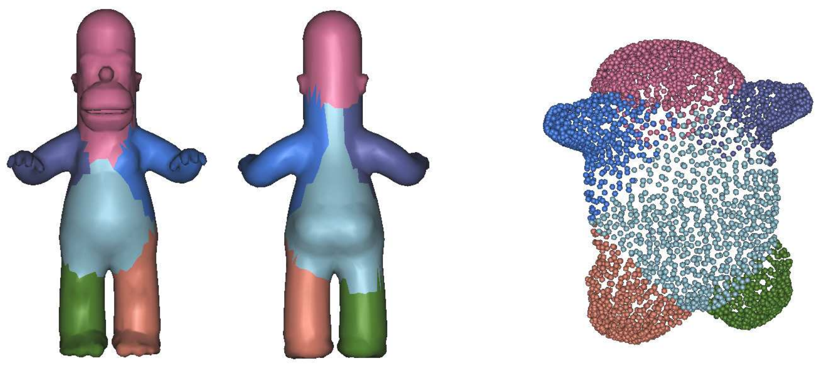
(a) with geodesic distance ($\alpha = 1$, $\beta = 0$, $\gamma = 0$)

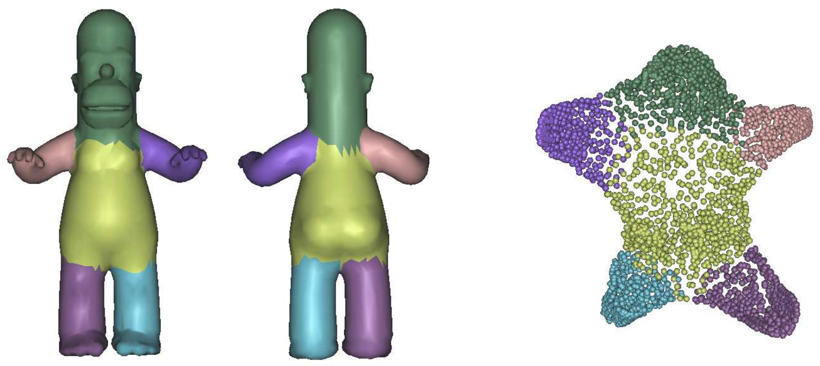
(b) with part-aware distance

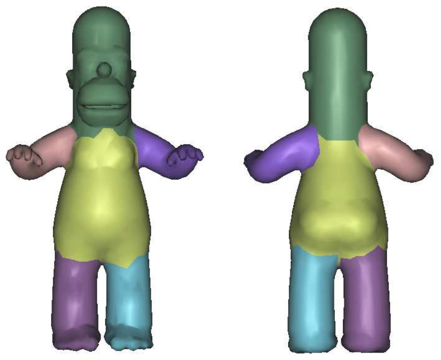
(c) with boundary enhancement

Figure 4.9: Segmentations on the Homer model and respective clusterings in the embeddings. In plot (a), only the geodesic distance is used. Plot (b) shows the result when the part-aware distance is used, and plot (c) illustrates what is achieved after enhancing the boundaries from (b). Note that the embeddings are rendered using the first three dimensions.

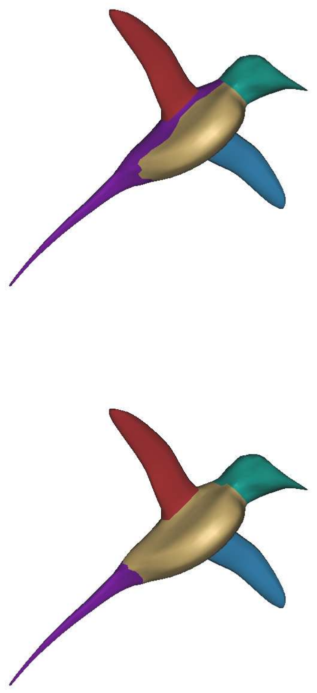
(a) colibri, 5 parts

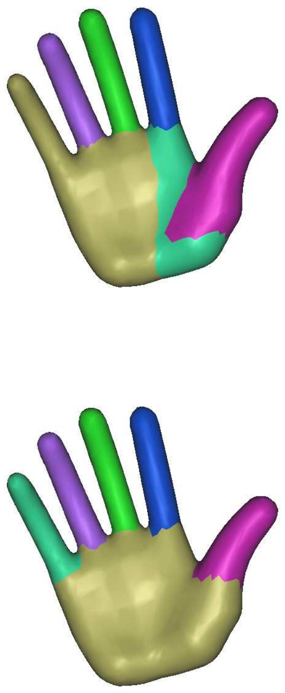
(b) hand, 6 parts

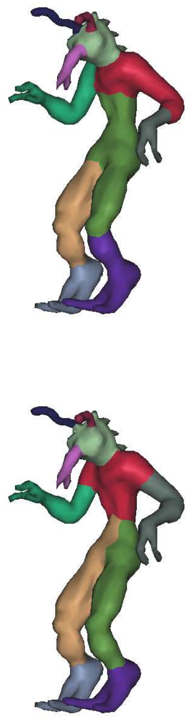
(c) bixo, 11 parts

Figure 4.10: Segmentation results achieved with (bottom row) and without (top row) the VSI distance.

We demonstrate the effectiveness of the VSI distance component in $\tilde{G}_c$ through more tests and the results are presented in Figure 4.10. In this figure, parts in the bottom row are achieved using the pre-set weights for the three distance components, while those in the top row are obtained ignoring the VSI distance ($\alpha = 0.01$, $\beta = 0.99$, $\gamma = 0$). It is clear that when the VSI distance is in place, the parts obtained are of superior quality.

Finally, more segmentation results are given in Figure 4.11, which includes models with genus greater than zero (vase, kitten, and dragon), as well as models with boundaries (heart). Clearly, the segments obtained correspond to the constituent parts of the shapes that are intuitive to human beings; the part boundaries have high quality as well.

Note that in all the above segmentation experiments, we set the dimensionality of face embeddings equal to k; this is discussed in Section 4.3.1. k is the only user-input parameter for this algorithm, and it is model-dependent. All other parameters are either fixed or

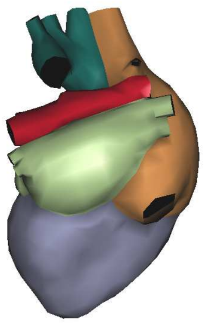
(a) heart, 5 parts

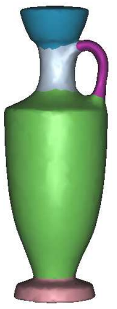
(b) vase, 5 parts

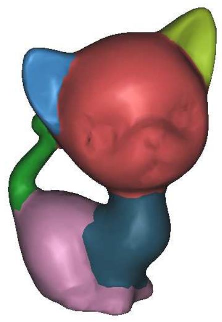
(c) kitten, 6 parts

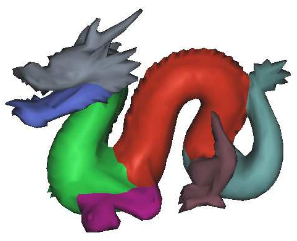
(d) dragon, 7 parts

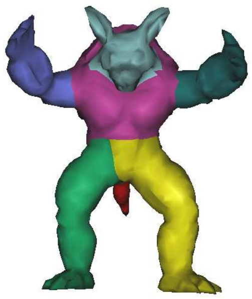
(e) armadillo, 7 parts

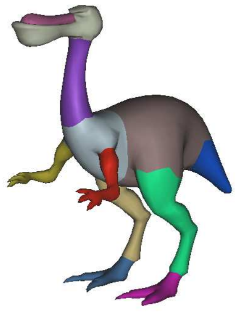
(f) dino-pet, 12 parts

Figure 4.11: Segmentations on a variety of different kinds of models.

automatically determined. Some heuristics [29, 59], including the eigen-gap [90], have been proposed to automatically infer an appropriate k. We notice that such methods are not sufficiently robust in general. Instead, we leave this problem to users.

Due to the super-quadratic complexity involved in the current algorithm, we have so far only been able to deal with meshes with up to a few thousand faces. For this thesis, we test our algorithms on a Windows machine with an AMD Opteron CPU at 2.41GHz and 8GB RAM. Running the algorithm on the vase model (5000 faces) takes about 44 seconds. When mesh size goes up, the computation time will increase rapidly and so will the space required to store the affinity matrix W, which is not sparse. It would be intangible to handle a mesh with hundreds of thousands of faces. We address this problem in the next chapter.

4.5 Summary

Our work in this chapter transforms the part information in the graph $\tilde{G}_c$ to a face embedding via a spectral embedding algorithm specifically designed for mesh segmentation. Resorting to the analogy to KPCA, we justify our algorithm and address several issues important to the effectiveness of the face embedding. The final mesh segmentation result is obtained from the embedding using the standard K-means clustering algorithm. In order to improve its efficiency and quality, we propose methods to reduce the embedding dimensionality, initialize seed proxies, and enhance part boundaries. Experiments have shown that our algorithm is able to extract parts from a shape with high quality.

However, the current algorithm is highly involved, incurring a complexity of $O(n^2 \log n)$. With such a super-quadratic complexity, the algorithm is only able to handle meshes with up to several thousand faces. We address this issue in Chapter 5.

Chapter 5

Sub-sampling

5.1 Overview

The segmentation algorithm based on spectral clustering proposed in Chapter 4 has a high computational cost — $O(n^2 \log n)$. As it is normal to segment meshes with up to hundreds of thousands of faces, we need to reduce its complexity for practical use.

We resort to sub-sampling for this purpose. Briefly, given an input mesh $\mathcal{M}$ with n faces, we first compute a small set of sample faces $\mathcal{F}^s = \{f_{s_i} \mid 1 \leq s_i \leq n, i = 1, \ldots, l\}$, where $l \in [2, n]$ is the sampling size. Then we construct only the corresponding rows of the distance matrix G and the affinity matrix W. As the full W is unknown, we apply the Nyström method to approximate the eigenvectors of W. Afterwards, the construction of the spectral embeddings of the faces and the K-means clustering are similarly conducted. Meanwhile, we provide a geometric interpretation for the Nyström method. This leads to a practical quality measure for a sample set and a farthest-point sampling scheme we use in practice. With sub-sampling, the overall complexity of the segmentation algorithm is reduced to $O(ml^2) + O(l \cdot n \log n)$, where $m = n - l$.

In Section 5.2, we review the Nyström method. Its geometrical interpretation is studied in Section 5.3, through which a quality measure of sub-sampling is derived. With such a quality measure, a farthest-point sampling scheme is suggested in Section 5.4. In Section 5.5 we modify the original segmentation algorithm to integrate sub-sampling. Experimental results and summary are given in the last two sections.

5.2 Nyström Method

The Nyström method is one of the best known approximation schemes for sampling and reconstruction for kernel techniques. It originates from finding numerical solutions of continuous eigenfunction problems [10] and has been applied by Williams and Seeger [132] for providing low-rank approximation to kernel matrices and by Fowlkes et al. [38] for image segmentation.

Consider a partition of a data set $\mathcal{Z}$, $|\mathcal{Z}| = n$, into two disjoint subsets $\mathcal{X}$ and $\mathcal{Y}$, with $|\mathcal{X}| = l$, $|\mathcal{Y}| = m$, respectively. Note that $n = l + m$ and $l \ll m$ in practice. Without loss of generality, we designate the points in $\mathcal{X}$ as samples and write the symmetric kernel matrix $K \in \mathbb{R}^{n\times n}$ for $\mathcal{Z}$ (recall that W can be considered as a kernel matrix) in block form:

$$K = \begin{bmatrix} A & B \\ B^T & C \end{bmatrix}, \tag{5.1}$$

where $A \in \mathbb{R}^{l\times l}$ encodes the affinities between the points in $\mathcal{X}$, $C \in \mathbb{R}^{m\times m}$ encodes the affinities between the points in $\mathcal{Y}$, and $B \in \mathbb{R}^{l\times m}$ encodes the *inter-affinities* between $\mathcal{X}$ and $\mathcal{Y}$. Let $A = E\Delta E^T$ be the eigenvalue decomposition of A, with the largest eigenvectors in the leading columns of E, then the l *leading* eigenvectors of K can be approximated, using the Nyström method, by

$$\tilde{E} = \begin{bmatrix} E \\ B^T E\Delta^{-1} \end{bmatrix}, \tag{5.2}$$

with columns of $\tilde{E}$ containing the approximate eigenvectors. We see that only the sub-block $[A\ B]$ is required to compute $\tilde{E}$. The complexity involved is $O(l^3) + O(ml^2)$, where the first term is for computing the eigenvalue decomposition of A and the second term is for computing $B^T E\Delta^{-1}$. Since $l \ll m$, the complexity is essentially $O(ml^2)$.

With $\tilde{E}$, the reconstructed kernel matrix, $\tilde{K}$, can be computed as

$$\tilde{K} = \tilde{E}\Delta\tilde{E}^T = \begin{bmatrix} A & B \\ B^T & B^T A^{-1} B \end{bmatrix}. \tag{5.3}$$

The quality of the sample set $\mathcal{X}$ can then be quantified by $\|K - \tilde{K}\|_F$. Since $\tilde{K}$ only replaces block C of K with $B^T A^{-1} B$, this quantification is equivalent to $\|C - B^T A^{-1} B\|_F$, the Frobenius norm of the *Schur complement* (FNSC).

Note that the approximated eigenvectors in $\tilde{E}$ are not normalized. Fowlkes et al. [38] have shown how to meaningfully normalize them. However, we have found that such a normalization works less preferably for our application.

The above discussion of the Nyström method has assumed that the sampled rows are at the leading rows of K for the sake of simplicity of presentation. In practice, we can simply permute the sampled rows to the leading rows. Be aware that the respective columns have to be consistently permuted as well to keep K symmetric. After the eigenvectors are computed, their entries are permuted back accordingly to recover the original ordering. This process is done implicitly and it is always assumed in the future that the leading rows of K are the sampled rows.

5.3 Quality Measure

The Nyström method only tells us how to extrapolate the eigenvectors given a subset of rows of the kernel matrix K; it does not specify how to select the rows for better approximation quality. FNSC is impractical for this purpose because C is unknown. In the following, we provide a geometric interpretation for the Nyström method and suggest a function Γ for evaluating the quality of a sample set, which is much more efficient to evaluate.

Following the discussion in Section 4.2.2, we reiterate that K implicitly defines a mapping $\phi(\cdot)$ that maps set $\mathcal{Z}$ to $\phi(\mathcal{Z}) = \{\phi(z_i) | z_i \in \mathcal{Z}\}$ in a high dimensional feature space $\mathcal{H} \in \mathbb{R}^h$. Similarly, we have in the feature space $\phi(\mathcal{X})$ for the sample set $\mathcal{X}$ and $\phi(\mathcal{Y})$ for its complementary set. Suppose $X^{h\times l} = [\phi(x_1)|\phi(x_2)|\dots|\phi(x_l)]$ contains the mapped points of $\phi(\mathcal{X})$, and $Y^{h\times m}$ and $Z^{h\times n}$ are defined similarly. As the entries of K are the inner products of $\phi(\mathcal{Z})$ in $\mathcal{H}$, we have $A = X^TX$, $B = X^TY$ and $C = Y^TY$. It has been shown in Section 5.2 that the Nyström method approximates C with $B^TA^{-1}B$. We now examine the geometric properties associated with this approximation.

Proposition 5.1. *$B^TA^{-1}B$ are the inner products between the points in $\phi(\mathcal{Y})$ after being orthogonally projected into Space$\big(\phi(\mathcal{X})\big)$, the space spanned by the points in $\phi(\mathcal{X})$.*

Proof. Denote by X^+ the pseudo-inverse of X, i.e., $X^+ = (X^TX)^{-1}X^T$. Given any point $\phi(y_i) \in \phi(\mathcal{Y})$, it is well known that $\phi(y_i)$'s orthogonal projection (also its closest point) in Space$\big(\phi(\mathcal{X})\big)$ can be computed as $\phi(y_i)_\perp = (XX^+)\phi(y_i)$. Having $Y_\perp = [\phi(y_1)_\perp|\phi(y_2)_\perp|\dots|\phi(y_m)_\perp] = (XX^+)Y$, we obtain the pairwise inner products of the points in $\phi(\mathcal{Y})$ after they are orthogonally projected into $\text{Space}\big(\phi(\mathcal{X})\big)$ as

$$\begin{aligned}
Y_\perp^T Y_\perp &= (XX^+Y)^T(XX^+Y) \\
&= Y^T(X^+)^T X^T X(X^+Y) \\
&= Y^T\big((X^TX)^{-1}X^T\big)^T X^T X(X^+Y) \\
&= Y^T XX^+Y \\
&= Y^T X\big((X^TX)^{-1}X^T\big)Y \\
&= (X^TY)^T(X^TX)^{-1}(X^TY) \\
&= B^TA^{-1}B
\end{aligned}$$

□

Therefore FNSC $= \|C - B^TA^{-1}B\|_F = \|Y^TY - Y_\perp^TY_\perp\|_F$, and this implies that in general the closer the points in $\phi(\mathcal{Y})$ are to $\text{Space}\big(\phi(\mathcal{X})\big)$ the smaller FNSC is. When $\text{Space}\big(\phi(\mathcal{Y})\big) \subseteq \text{Space}\big(\phi(\mathcal{X})\big)$, we have $Y = Y_\perp$ and $B^TA^{-1}B = Y_\perp^TY_\perp = Y^TY = C$, namely, $B^TA^{-1}B$ reconstructing C exactly. With that said, the scale of FNSC can be reflected by the overall distances from the points in $\phi(\mathcal{Y})$ to $\text{Space}\big(\phi(\mathcal{X})\big)$. In fact, we have

Proposition 5.2. *The trace of $C - B^TA^{-1}B$ is the sum of the squared distances from the points in $\phi(\mathcal{Y})$ to $\text{Space}\big(\phi(\mathcal{X})\big)$.*

Proof. Given a $\phi(y_i) \in \phi(\mathcal{Y})$, the squared distance from $\phi(y_i)$ to $\text{Space}\big(\phi(\mathcal{X})\big)$ is $\|\phi(y_i) - \phi(y_i)_\perp\|_2^2 = \|\phi(y_i) - XX^+\phi(y_i)\|^2$. Then the sum of all the squared distances is

$$\begin{aligned}
\sum_{i=1}^m \|\phi(y_i) - XX^+\phi(y_i)\|^2 &= \sum_{i=1}^m \big(\phi(y_i) - XX^+\phi(y_i)\big)^T\big(\phi(y_i) - XX^+\phi(y_i)\big) \\
&= \sum_{i=1}^m \phi(y_i)^T(I - XX^+)\phi(y_i) \\
&= \sum_{i=1}^m \phi(y_i)^T\phi(y_i) - \sum_{i=1}^m \phi(y_i)^T(XX^+)\phi(y_i) \\
&= \text{tr}(C) - \text{tr}(Y^TXX^+Y) \\
&= \text{tr}\,(C) - \text{tr}(B^TA^{-1}B) \\
&= \text{tr}\,\big(C - B^TA^{-1}B\big)
\end{aligned}$$

where $\text{tr}(\cdot)$ is the matrix trace operator. The second last step is due to the fact $Y^TXX^+Y = B^TA^{-1}B$, which is shown in the proof of Proposition 5.1. □

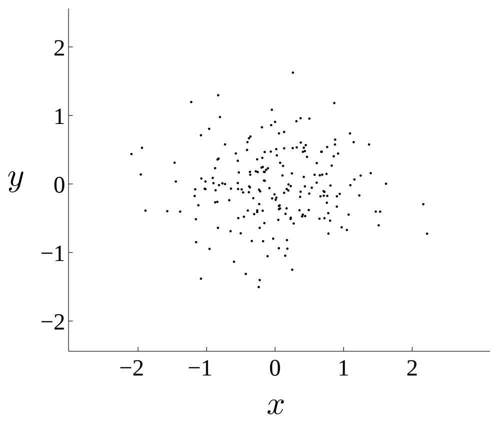

(a) test point set

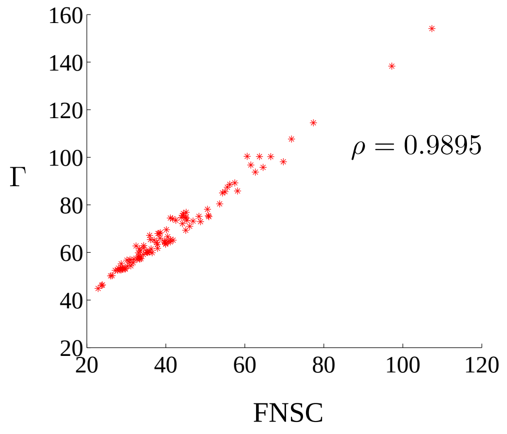

(b) (FNSC, Γ) observations

Figure 5.1: Strong correlation between FNSC and Γ. (a): The point set with a Gaussian distribution, where the variances along x and y axes are 0.76 and 0.54, respectively. (b): Plot of the 100 observations to (FNSC, Γ). The correlation coefficient is $\rho = 0.9895$.

Via Proposition 5.1 and Proposition 5.2, we define function

$$\Gamma \triangleq \mathrm{tr}(C) - \mathrm{tr}(B^T A^{-1} B) \tag{5.4}$$

to measure the quality of a sample set. We have shown that a small Γ would tend to lead to a small FNSC. With Γ, we can evaluate the quality of a sample set without knowing the entire C, which is needed when FNSC is used. Although C is not known, $\mathrm{tr}(C)$ can usually be efficiently computed. In our implementation with equation 4.1, we have $W_{ii} \equiv 1$, in which case, $\mathrm{tr}(C) = m$ is a constant and only $\mathrm{tr}(B^T A^{-1} B)$ matters.

Figures 5.1 verifies the strong correlation between FNSC and Γ. In this experiment, we generate 200 points with a Gaussian distribution, whose deviation along each axis is randomly selected in $(0, 1)$. The corresponding kernel matrix K is constructed using Euclidean distance and an exponential kernel function. We randomly sample only 2 points and the resulting pair (FNSC, Γ) is treated as an observation to their corresponding random variables. We obtain 100 observations and the correlation of the two random variables is 0.9895. Clearly, FNSC and Γ are strongly correlated.

5.4 Sampling Scheme

Given a sampling size, our goal is to find the samples such that Γ is minimized. One possible approach is to add samples iteratively, in a greedy manner: the next sample to add is always the one that minimizes the current Γ. In short, the sampling scheme keeps track of the current affinity matrices A and B. The next sample is selected as the one such that the updated A and B would minimize Γ. Given the updated A and B, the evaluation of Γ has a complexity of $O(ml^2)$. If carried out naively by evaluating Γ against each data point, finding the next sample would cost $O(m^2l^2)$, which is not acceptable. To overcome this, we consider the *best sampling scheme* [120]. Instead of finding the next best sample from all the remaining data points, we only try to find it among the best 1% with probability 95%. Assuming that the columns of B are independent identically-distributed (IID) random variables, we simply need to evaluate Γ on a random sample set of size $\lceil \log(0.01)/\log(0.95) \rceil = 90$, regardless of the data size. The overall complexity for finding l samples with this approach would be $O(90ln\log n) + O(90ml^3)$, where the first term is for computing the geodesic distances from $\tilde{G}_c$ to update A and B. We call this approach Γ-sampling.

Although it achieves low asymptotic complexity, the Γ-sampling scheme is still not sufficiently efficient due to the large constant in its complexity, especially for a dense mesh (n is large). In practice, we use a more efficient farthest-point sampling scheme which is suggested by an observation made on Γ.

In order to minimize Γ, we can aim to maximize $\mathrm{tr}(B^TA^{-1}B)$ as $\mathrm{tr}(C)$ is a constant in our case. Based on the cyclic property of matrix trace, we have

$$\mathrm{tr}(B^TA^{-1}B) = \mathrm{tr}(A^{-1}BB^T) = \mathrm{tr}(A^{-1}\sum_{j=1}^{m} B_jB_j^T). \tag{5.5}$$

With the assumption that the columns of B (B_j's) are random variables with IID distribution, entries of $\sum_{j=1}^{m} B_jB_j^T$ tend to be similar. We have observed such a property in practice, especially when m is large. Therefore we can rewrite $\sum_{j=1}^{m} B_jB_j^T \approx \kappa\mathbf{1}\mathbf{1}^T$, with $\kappa \in (0, m)$ being a fixed value, hence

$$\mathrm{tr}(B^TA^{-1}B) \approx \kappa\mathrm{tr}(A^{-1}\mathbf{1}\mathbf{1}^T) = \kappa\mathbf{1}^T(A^{-1}\mathbf{1}). \tag{5.6}$$

From Equation 5.6, we see that there are two conditions for $\mathrm{tr}(B^TA^{-1}B)$ to attain a large value: (1) a large $\mathbf{1}^T(A^{-1}\mathbf{1})$, and (2) a large κ.

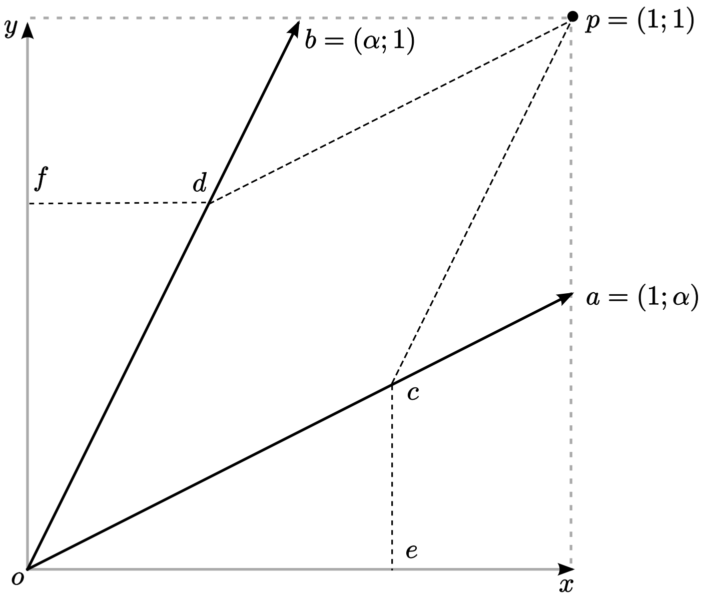

Figure 5.2: The geometric examination of $\mathbf{1}^T(A^{-1}\mathbf{1})$ in $\mathbb{R}^2$. Suppose $A = [1, \alpha; \alpha, 1]$, $0 \leq \alpha \leq 1$, then the columns of A represent the coordinate basis shown as oa and ob. If we write $A^{-1}\mathbf{1} = [s; t]$, s and t can be computed geometrically by drawing lines pd and pc parallel to axes oa and ob, respectively. In other words, $s = |oc|/|oa|$ and $t = |od|/|ob|$. It is easy to see $s = |oc|/|oa| = |oe|/|ox| \leq 1$. Similarly, $t = |od|/|ob| = |of|/|oy| \leq 1$. As a result, $\mathbf{1}^T(A^{-1}\mathbf{1}) = s + t \leq 2$. As oa and ob approach ox and oy, $s + t$ keeps increasing until 2 is reached, at which time oa and ob turn into the canonical basis.

For condition (1), note that the vector $A^{-1}\mathbf{1}$ contains the coefficients of the expansion of $\mathbf{1}$ in the space whose basis are the columns of A, and the diagonals of A are 1 and the off-diagonals are in the range $[0, 1]$. Figure 5.2 shows that, in 2D, $\mathbf{1}^T(A^{-1}\mathbf{1}) \leq l$, where l is the number of samples ($l = 2$ in this case). The equality is achieved when the columns of A are the canonical basis. Since this can be generalized to arbitrary dimension and the canonical basis mean that the off-diagonals of A are zeros, we should select samples such that the affinities (distances) between them are as small (large) as possible.

Condition (2) requires κ to be large. To this end, entries of B should be large, indicating that the distances between the sample faces and the un-sampled faces are small in average. To satisfy condition (1), we have distributed sample faces mutually far apart on a mesh surface. Therefore the average distances from the sample faces to the un-sampled faces tend to converge, making condition (2) much less influential. Our experiments have also verified that the first condition plays the dominant role.

In accordance with condition (1), we propose to sample faces that are mutually farthest away using a max-min strategy as inspired by previous works, e.g., [34]. Given a distance graph $\tilde{G}_c$, the sampling scheme works as in Figure 5.3. Note that step 1 attempts to find the first two samples that are globally farthest apart efficiently. We do not find the exact solution for this since it is expensive.

1. Randomly sample a face f_{s_p} and find the face f_{s_q} that is farthest to f_{s_p}. Switch f_{s_p} and f_{s_q} and repeat this process until both faces stabilize. Then set $f_{s_1} = f_{s_p}$, $f_{s_2} = f_{s_q}$, and $\mathcal{F}^s = \{f_{s_1}, f_{s_2}\}$.
2. Iteratively find the remaining samples. Specifically, select the next sample f_{s_i} as the one that maximizes the minimum distance to the previous samples $f_{s_1}, \ldots, f_{s_{i-1}}$.

Figure 5.3: Farthest-point sampling scheme in max-min fashion.

Since the distances between faces are the graph distances in $\tilde{G}_c$, finding the face farthest to a given one takes $O(n \log n)$ time. In step (2), whenever a new sample face is added, we compute its distances to all the other faces. By maintaining the distances between all the previous sample faces and the un-sampled faces, we can find the next sample face in $O(n)$ time. Since the convergence rate of step (1) is high (usually below 5 iterations), the complexity is dominated by step (2), making the overall complexity of this sampling algorithm $O(l \cdot n \log n)$.

5.5 Modified Segmentation Algorithm

The modified segmentation algorithm based on spectral clustering with sub-sampling is described in Figure 5.4. Overall it is similar to the case without sampling as described in Section 4.2 and Section 4.3. However, it is worth mentioning the following issues.

- Given a sampling size l, the Nyström method tells how to extrapolate l eigenvectors approximately. However, it does not specify which original eigenvectors the extrapolated eigenvectors correspond to. Practically our experiments have shown that the extrapolated eigenvectors correspond to the largest original eigenvectors. Roughly, this can be understood by thinking of the eigenvectors as frequencies of the 2D signal

1. Compute sample face set $\mathcal{F}^s$, $|\mathcal{F}^s| = l$, as in Figure 5.3.
2. Calculate a partial distance matrix G' that contains the rows (corresponding to the samples) of the full distance matrix G. Convert G' to a partial affinity matrix W', where $W'_{ij} = e^{-G'_{ij}/2\sigma^2}$ and σ is the square root of the average of the entries of G'.
3. Compute the l approximate eigenvectors for the affinity matrix W through W' with the Nyström method as in Section 5.2 (W is considered as the kernel matrix K). Denote by $\tilde{E}$ the approximate eigenvectors and Δ the eigenvalues of sub-block A.
4. Supposing all the eigenvalues of A are non-negative, derive the spectral embedding $\tilde{U} = \tilde{E}_{[2...l]}\Delta^{\frac{1}{2}}$.
5. Treat the rows of $\tilde{U}$ as the face embeddings, set the seed proxies as the embeddings of the sample faces in $\mathcal{F}^s$, and run the K-means algorithm.

Figure 5.4: Mesh segmentation based on spectral clustering with sub-sampling.

W [123, 124], where the largest eigenvectors correspond to low frequencies. When sub-sampling, it is the low-frequency information that is reconstructed first. This phenomenon is also observed by Belongie et al. [12].

- For the spectral embedding algorithm in Figure 4.2 without sampling, step (4) scales the eigenvectors ($V_{[2...r]}$) by the square root of the eigenvalues ($\Lambda'^{\frac{1}{2}}$). With sub-sampling, since the Nyström method does not compute the eigenvalues of W, how should we scale the approximate eigenvectors in $\tilde{E}$? It is noticed in [132] that the eigenvalues of W are roughly $\frac{n}{l}$ times of those of A. Therefore we use the eigenvalues of A to scale the approximate eigenvectors in $\tilde{E}$; the uniform scaling factor $\frac{n}{l}$ is ignored without affecting the subsequent clustering.
- We have assumed that the eigenvalues of A are all positive. If not, we can simply ignore the non-positive ones as described in 4.2.5. In fact, we have never encountered such cases in our experiments. Since the eigenvalues of A and W are approximately the same up to a scaling factor ($\frac{n}{l}$) and W always has positive leading eigenvalues (Section 4.2.5), A's eigenvalues are likely to be positive as well.
- In the clustering step, we could find the seed proxies as the embeddings that are mutually farthest away (Section 4.3.2). But as the distances between the embeddings

mimic the distances in $\tilde{G}_c$ (Section 4.2.6) and the faces in sample set $\mathcal{F}^s$ are computed from $\tilde{G}_c$ to be mutually farthest away, we can reuse this information by simply setting the seed proxies as the embeddings of the sample faces. This makes the algorithm more efficient.

Another issue we need to address is how to set l, the number of samples. As discussed in Section 4.3.1, we set the dimensionality of the spectral embedding to k, the number of segments given by a user. When sub-sampling, the number of samples determines the number of eigenvectors in $\tilde{E}$. Therefore, we only need to set $l = k + 1$ in order to obtain enough eigenvectors for embedding (note that the first approximate eigenvector is discarded as it is close to a constant vector). Empirically, such a low sampling rate achieves high segmentation quality while keeping the complexity low.

5.6 Experimental Results

Complexity Since our K-means algorithm has a high convergence rate, the asymptotic complexity of the entire algorithm is dominated by the first three steps in Figure 5.4. According to the analysis in Section 5.2 and Section 5.4, the complexity of our spectral clustering algorithm with sub-sampling is $O(ml^2) + O(l \cdot n \log n)$. In practice, we set $l = k + 1$.

Overview of experiments We have five experiments in this section. The first two experiments test our sampling scheme with the Nyström method in general. The last three experiments demonstrate how the segmentation algorithm with sampling works on meshes.

In our first experiment, we test the performance of the farthest-point sampling method, by measuring the difference between approximate eigenvectors and accurate eigenvectors. For comparison purpose, we also test the Γ-sampling scheme described in Section 5.4. To focus on the effect of sampling only, we consider points in $\mathbb{R}^3$, treating each point as a mesh face and the Euclidean distances between points as the graph distances between faces in $\tilde{G}_c$. We generate a total of 200 point sets and the reported result is the average of the corresponding 200 tests. A point set is produced by a mixture of 10 Gaussian distributions. Each Gaussian distribution has a random size between 30 and 60, with its mean at a random point within a cube of side length 1 and deviations along each dimension randomly picked from (0, 0.1]. Figure 5.5 shows the test results. In plots (a) and (b), we observe that the approximation errors for both the second and the third eigenvectors decrease as the number of samples increases. In fact, this is true for all other eigenvectors as well. Note that in plot (b), the number of samples is at least 3; this is because the Nyström method cannot extrapolate more eigenvectors than the number of samples. Plot (c) shows the average approximation error over all available eigenvectors given a sampling size. Since a larger sampling size is able to extrapolate more trailing eigenvectors and the trailing eigenvectors typically have lower approximation accuracy, we see that the average approximation error for all eigenvectors increases when more samples are used. By this experiment, it is verified that the farthest-point sampling consistently outperforms random sampling. Although it does not perform as well as Γ-sampling, it is more efficient and works well in our experiments.

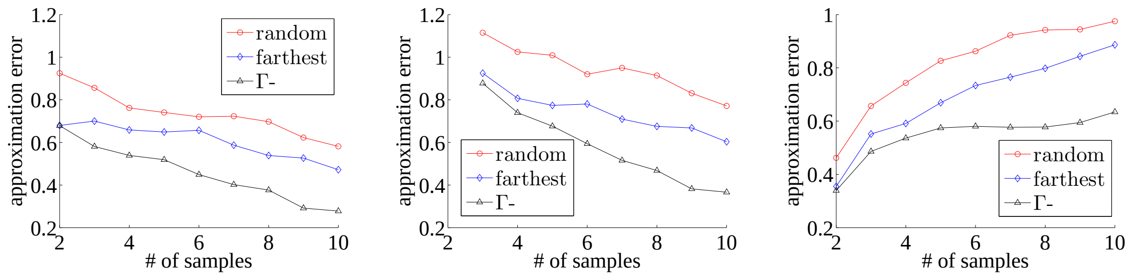

(a) for 2nd eigenvector (b) for 3rd eigenvector (c) for all eigenvectors

Figure 5.5: Approximation quality of eigenvectors via different sub-sampling methods. The approximation error is measured as the L2 norm of the difference between the original and the approximate eigenvectors, up to sign flips.

The approximation quality of extrapolated eigenvectors through the Nyström method is also influenced by the tightness of clustering present in a point cloud. This phenomenon is demonstrated in Figure 5.6. In this test, we build three point clouds in 2D shown in the first column, and sample three points for each case. Each point cloud consists of three Gaussian clusters centered at $(0, 0)$, $(10, 0)$, and $(10, 10)$. Three levels of clustering tightness are introduced by setting the deviations along x-axis and y-axis in each point cloud to 0.1, 1, and 3, respectively. The second (third) column shows, for the corresponding affinity matrix W, the second (third) eigenvectors obtained with and without sub-sampling. It is clear that if the clusters are tight and far apart from each other, the approximation quality is high and vice versa. This is easy to explain according to Proposition 5.1 and Proposition 5.2. For the ideal case in which the three clusters are infinitely far away and the points within each cluster coincide with each other, based on the feature space distance

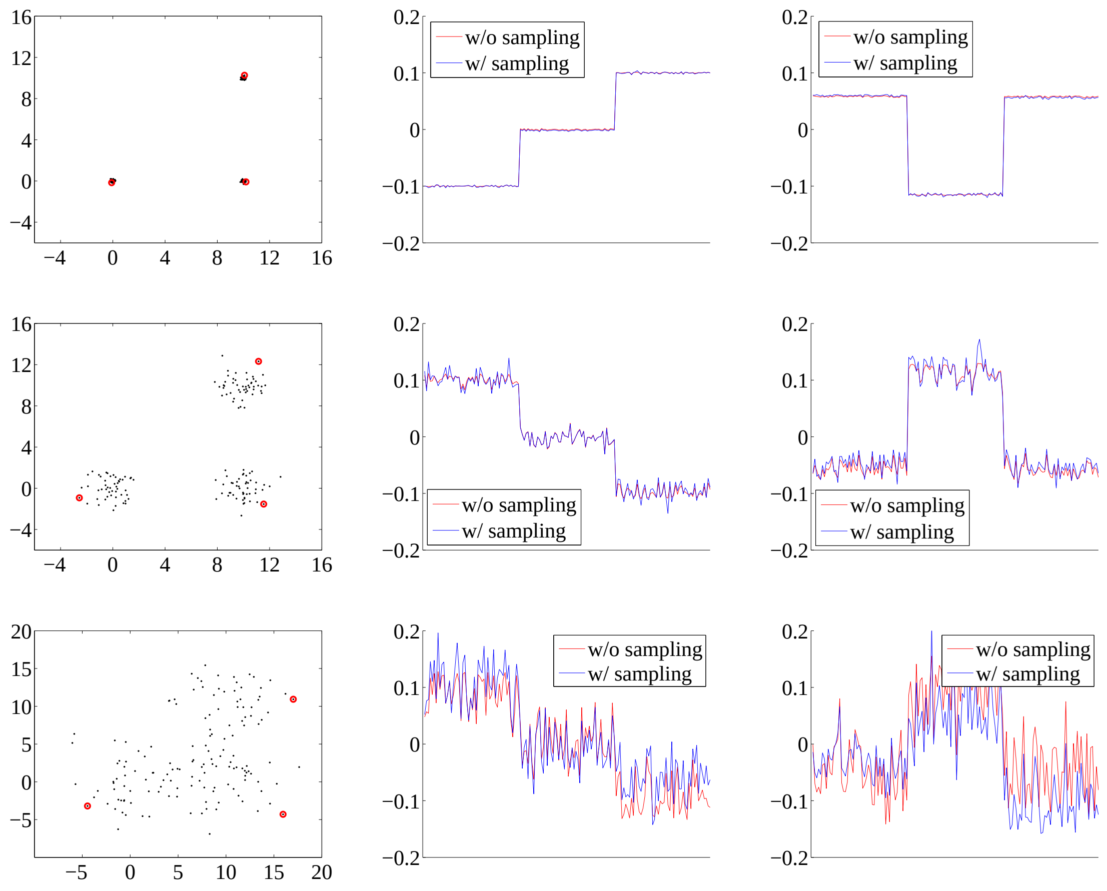

Figure 5.6: Quality of approximate eigenvectors is influenced by the tightness of clustering. In each row, the first plot shows a point cloud with a certain degree of clustering tightness, where the red circles indicate the three sample points chosen by our farthest-point sampling. The second plot and the third plot illustrate the second and the third eigenvectors, respectively, of the affinity matrix W derived from the corresponding point cloud, with and without sub-sampling.

calculation (Equation 4.16), each cluster degenerates to a single point in the feature space $\mathcal{H}$. Therefore the three sample points span the entire space spanned by all the points in $\mathcal{H}$; in other words, we have $\text{Space}\big(\phi(\mathcal{X})\big) = \text{Space}\big(\phi(\mathcal{Y})\big)$. This implies $\Gamma = 0$ and the eigenvector extrapolation is exact. On the other hand, if the clusters are loose and overlap with each other, points will be scattered out in $\mathcal{H}$. Then $\text{Space}\big(\phi(\mathcal{X})\big)$ would tend to occupy only a small subspace of $\text{Space}\big(\phi(\mathcal{Y})\big)$, causing large Γ and lower approximation quality in general. With this being said, a sensitive part-aware metric, as the one described in Chapter 3, not only contributes to a face embedding easy for the K-means algorithm to extract prominent clusters, but also helps the sub-sampling method achieve high accuracy.

Let us now apply the spectral clustering algorithm with sub-sampling to two small meshes used in Section 4.4, and compare the approximate eigenvectors with the accurate ones. In Figure 5.7, the two columns show the segmentation results, the original, and the approximated eigenvectors of the enforcer model and the armadillo model, respectively. Compared with those in Figure 4.7(a) and Figure 4.11(e), almost the same segmentation results are achieved with sub-sampling. For each model, we also see that the extrapolated eigenvectors (blue) approximate the accurate ones (red) reasonably well, which is why the segmentation quality under sub-sampling is not significantly sacrificed. Reminiscent of the analysis for Figure 5.6, the approximation quality of eigenvectors for the enforcer model is higher than that for the armadillo model, since the faces of the enforcer form tighter clusters due to the larger distance changes across the part boundaries. It is worth reiterating that we only set the sample number to $k + 1$ (k is the number of segments) as mentioned in Section 5.5; if we increase the sampling rate, better approximation quality is expected. In practice, we found that such a low sampling rate is sufficient.

Recall the comparison of the distance fields shown in Figure 3.9. Since the three meshes are too large, we were unable to handle them in Chapter 4 before the sub-sampling is introduced. In Figure 5.8, segmentation results on these three meshes via sub-sampling are shown. Again, to demonstrate the effectiveness of VSI distance, we also give in the top row the segmentation results obtained using only geodesic and angular distances ($\alpha = 0.01$, $\beta = 0.99$, and $\gamma = 0$). For example, the fingers of the hand model are better segmented off the palm along the intuitive boundaries in the bottom row. So are the horse's front leg and right ear, and the dragon's left arm and tail. These are the natural consequences of the sudden distance changes across those regions as shown in the bottom row of Figure 3.9.

Finally, more segmentations on a variety of models are reported in Figure 5.9. Note that

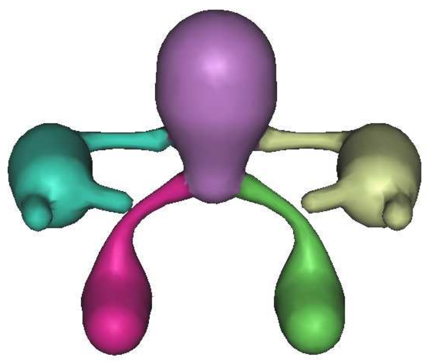
enforcer, 5 parts

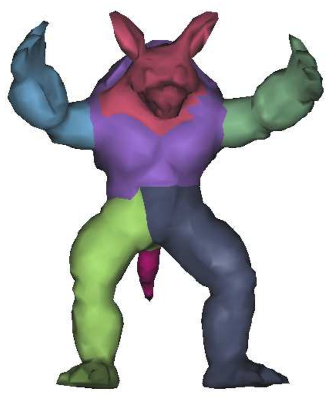
armadillo, 7 parts

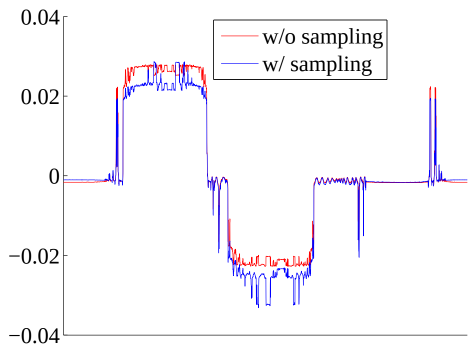

2^{nd} eigenvectors

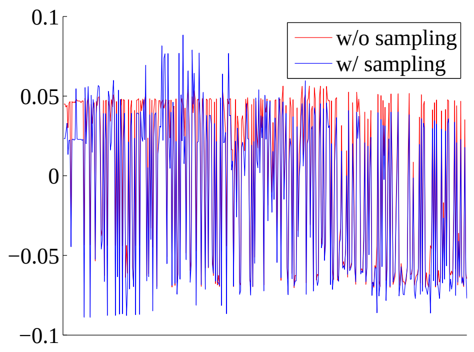

2^{nd} eigenvectors

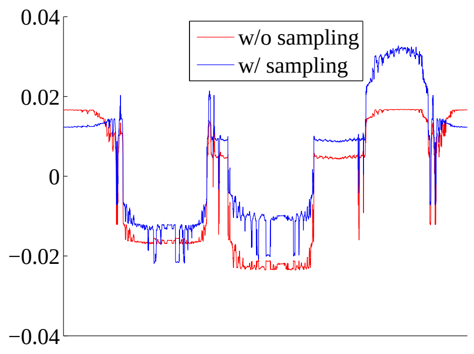

3^{rd} eigenvectors

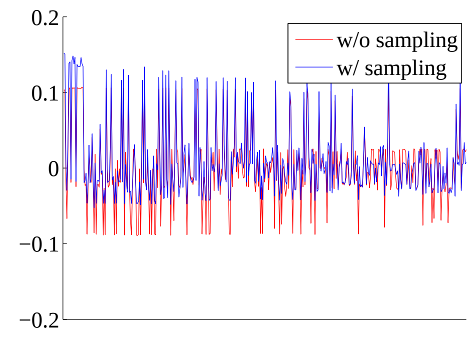

3^{rd} eigenvectors

Figure 5.7: Segmentations of two models via sub-sampling and the eigenvectors. In each column, both the second and the third eigenvectors obtained with (blue) and without (red) sampling are drawn.

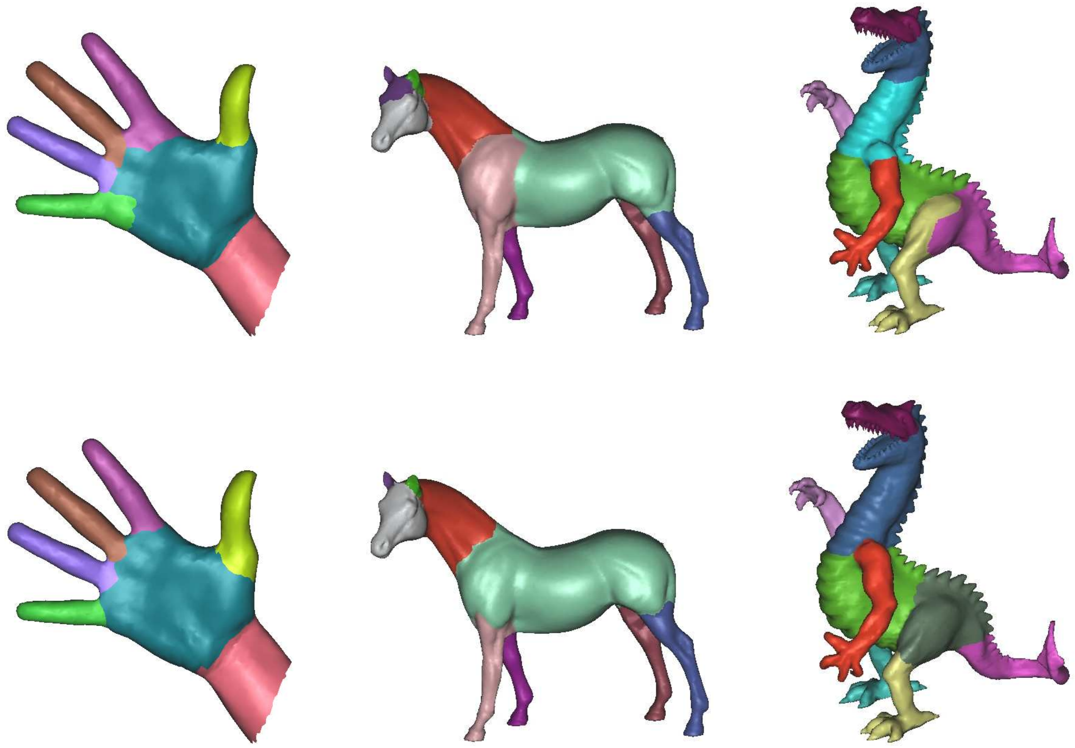
(a) hand, 7 parts (b) horse, 9 parts (c) dragon, 9 parts

Figure 5.8: Segmentation results achieved with (bottom row) and without (top row) VSI distance.

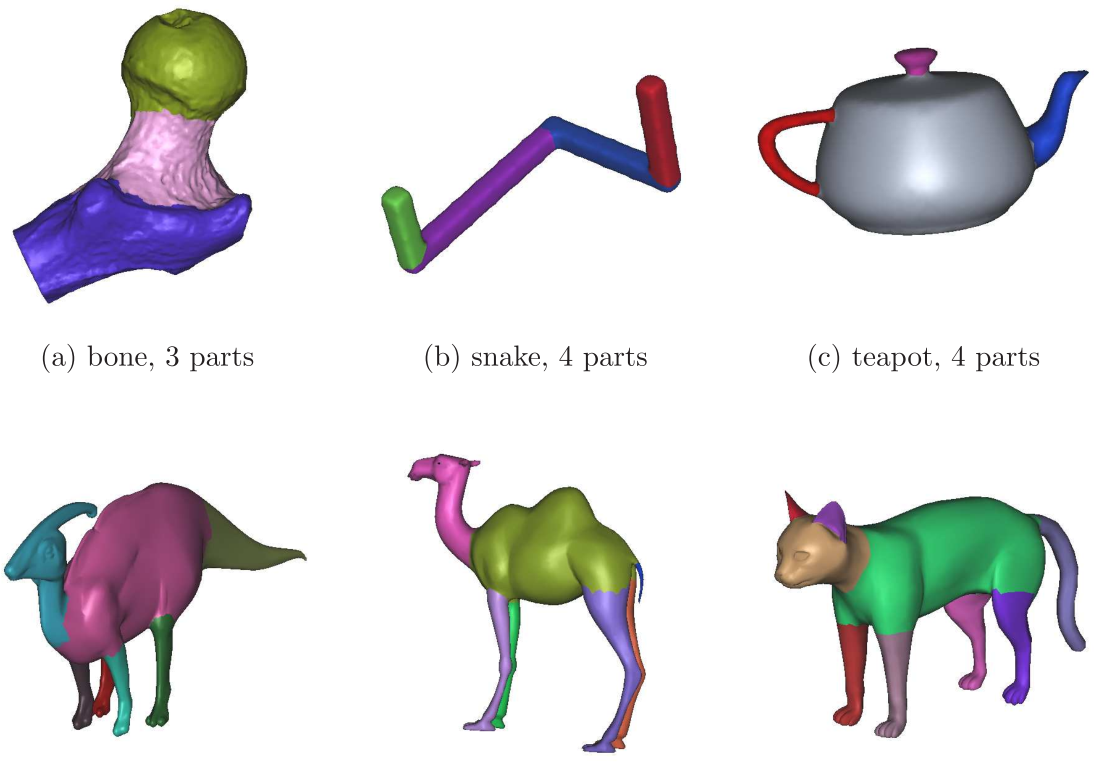

(a) bone, 3 parts (b) snake, 4 parts (c) teapot, 4 parts

(d) dilo, 7 parts (e) camel, 7 parts (f) cat, 9 parts

Figure 5.9: Segmentation results of various models with sub-sampling.

both the teapot and the camel have genus greater than 0. High quality segmentation results are achieved on all these models using a small number of samples. For the dilo model with about $55K$ faces, our algorithm takes only about 4 seconds. If we subdivide the model into $220K$ faces, only 13 seconds are needed.

5.7 Summary

We integrate sub-sampling to the mesh segmentation algorithm described in Chapter 4. The complexity of the new algorithm is significantly reduced from $O(n^2 \log n)$ to $O(ml^2) + O(l \cdot n \log n)$, where l is the number of samples and $m = n - l$. In our application, we set $l = k + 1 \ll n$, with k being the desired number of segments given by users. With such a low sampling rate, the size of meshes that our algorithm can handle increases from several thousands to hundreds of thousands.

Our sub-sampling scheme is based on the Nyström method, a popular technique for computing approximate eigenvectors of a symmetric matrix when only a subset of its rows are available. By examining the geometric meaning of the Nyström method, we propose a function Γ to evaluate the sampling quality. Eventually, a farthest-point sampling scheme is used to optimize for Γ approximately. The experiments have demonstrated that our sub-sampling approach is able to achieve comparable segmentation results with higher efficiency.

We also notice two limitations of the current segmentation algorithms, with and without sub-sampling. First, it requires users to input the number of segments k. Segmentation quality could suffer if k is not set appropriately. Secondly, although the part-aware distance enhances the clusters in the embedding space, prominent parts may still be missed occasionally due to the limitations of the K-means clustering, especially when the desired k is large, such as for those shown in Figure 6.18(f) and Figure 6.19(f). The algorithm proposed in Chapter 6 improves on these issues by incorporating segmentability and salience, but with higher computational cost.

Chapter 6

Segmentation Driven by Segmentability and Salience

6.1 Overview

In this chapter, we improve upon the previous segmentation algorithm by introducing *segmentability* and *salience-driven* cut. Rather than using a simultaneous k-way partitioning, the improved algorithm iteratively bisects mesh parts. In each iteration, a mesh part with the largest surface area is considered. If the mesh part has a segmentability score above a fixed threshold, it is cut into two sub-parts, which are to be considered for further segmentation; otherwise this mesh part is deemed not segmentable and becomes an output part. In order to find the best cut, the faces of the selected mesh part are first sorted into a sequence. Then the algorithm searches through this sequence, measures the salience at each location, and chooses the cut that has the highest salience score. Figure 6.1 illustrates the flow of this algorithm. Such an algorithm has the following merits:

- Segmentability provides a robust quantitative evaluation as to whether a shape contains any parts. Accordingly, our algorithm can fix a segmentability threshold as the stopping criteria for the iterative cut. Note that a single segmentability threshold works for different models, while the number of segments used in the previous algorithm is model-dependent. Thus, the improved algorithm achieves higher autonomy.
- With mesh faces sorted in a sequence, the search space for the best cut is significantly reduced. This makes the salience-driven cut search affordable. Computed carefully,

```
input  : Mesh $\mathcal{M}$.
output: Sub-meshes $\mathcal{O} = \{\mathcal{M}_1, \mathcal{M}_2, ...\}$.
begin
    $\mathcal{O} = \emptyset$, $\mathcal{Q} = \{\mathcal{M}\}$ ;
    $\eta = 0.1$ ;
    while $|\mathcal{Q}| \neq 0$ do
        $\mathcal{M}_c \leftarrow$ the mesh piece in $\mathcal{Q}$ with the largest surface area ;
        $\mathcal{Q} = \mathcal{Q} - \{\mathcal{M}_c\}$ ;
        $S \leftarrow$ Segmentability($\mathcal{M}_c$) ;                          /* Section 6.2 */
        if $S \geq \eta$ then
            $\varrho$ = FaceLinearization($\mathcal{M}_c$) ;                       /* Section 6.3 */
            $\{\mathcal{M}'_s, \overline{\mathcal{M}'_s}\} \leftarrow$ SalienceCut($\mathcal{M}_c$, $\varrho$) ;           /* Section 6.4 */
            $\mathcal{Q} = \mathcal{Q} \bigcup \{\mathcal{M}'_s, \overline{\mathcal{M}'_s}\}$ ;
        else
            $\mathcal{O} = \mathcal{O} \bigcup \{\mathcal{M}_c\}$ ;
        end
    end
end
```

Figure 6.1: Mesh segmentation driven by segmentability and salience.

the sequence also effectively preserves the meaningful cuts.

- By incorporating a salience measure mimicking human intuition for parts into the cut search, the segmentation quality is enhanced.

In Section 6.2, we discuss the concept of segmentability within our context and show how the segmentability analysis is performed. Once a mesh part passes the segmentability test, Section 6.3 studies how to obtain an effective face sequence for the subsequent salience-driven cut search, which is discussed in Section 6.4. Experiments are given in Section 6.5 and Section 6.6 presents the summary.

6.2 Shape Segmentability

Instead of letting users provide the number of segments for each input mesh, it is desirable to have an algorithm that can figure out this information on its own. To fulfill this goal, we want to tell when a mesh has any parts, or, in other words, is segmentable. A key observation we make is that there are two primary factors that can render a shape segmentable. The first one is the *branching* factor. That is, if a shape has branches, then it is segmentable. We refer to the segmentability caused by branching as *structure* segmentability. The second factor is due to concavity over the boundary of a part in the absence of branching, where the induced segmentability is referred to as *geometry* segmentability. Do not confuse these two terms with structural-level and geometrical-level segmentations. In our context, both structure and geometry segmentabilities are for the structural-level segmentation.

Obtaining either the structure or the geometry segmentability information from a 3D mesh is rather difficult and inefficient. As a solution, we project the mesh into 2D and exploit the outer contour of the 2D projection for segmentability analysis. It is not a surprise that a significant amount of information may be lost when going from 3D to 2D. However, by carefully manipulating the projecting procedure, we are able to preserve, and even enhance, the part information useful for the subsequent shape analysis. In our approach, structure and geometry segmentability information are extracted from 3D meshes separately, using two projection operators: L and M. Note that the resulting projections are essentially 2D spectral embeddings. In order to differentiate this operation from the spectral embedding for K-means (Section 4.3), we call these 2D embeddings for segmentability analysis segmentability projections, or simply *projections*. For simplicity, we refer to a projection via L (M) as L-projection (M-projection). We study both projection operators as follows.

6.2.1 Structure Projection

Given an input mesh with n vertices, its graph Laplacian $L \in \mathbb{R}^{n\times n}$ is defined as $L = D - T$, where $T_{ij} = 1$ whenever (i, j) is an edge, otherwise $T_{ij} = 0$; D is a diagonal matrix whose diagonals are row sums of T. Hence the affinity T_{ij} between vertices is determined only by their connectivity. Let $L = \Xi\Lambda\Xi^T$ be the eigenvalue decomposition of L, where the eigenvalues in Λ are in ascending order. It is well known that L is positive semidefinite with the smallest eigenvalue $\lambda_1 = 0$ and the corresponding eigenvector Ξ_1 being a constant vector. Since L is symmetric, its eigenvectors are orthogonal and span the entire space $\mathbb{R}^{n\times n}$.

Suppose the rows of $X \in \mathbb{R}^{n\times 3}$ contain the coordinates of the vertices of the input mesh. Then X can be written as a linear combination of the eigenvectors of L (since the eigenvectors span the entire space). Projecting X into the subspace spanned by the first k eigenvectors of L, we obtain

$$\tilde{X} = \Xi_{[1\ldots k]}\Xi^T_{[1\ldots k]}X,$$

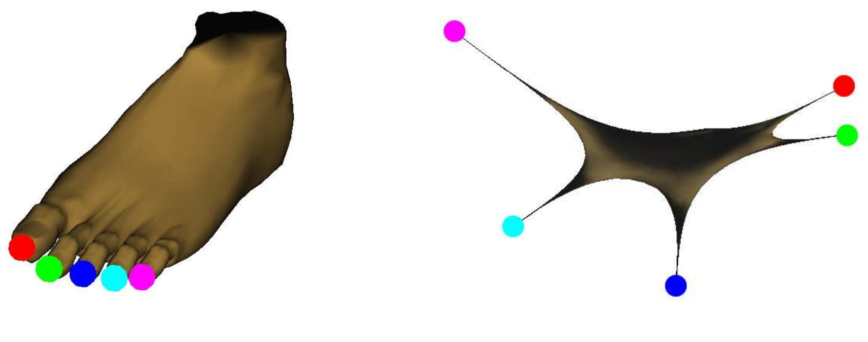

Figure 6.2: L-projection (b) of a foot model (a) with branching structure. Color dots indicate correspondence.

where $\Xi_{[1...k]}$ denotes the first k columns of Ξ. This projection process can also be seen as applying an ideal low-pass filter (only allowing the leading k frequencies to "pass") to the mesh coordinate signal, akin to Laplacian smoothing [123]. Choosing $k = 3$, we obtain a planar shape, since the first eigenvector is a constant vector.

As a result of Laplacian smoothing, high-frequency information, e.g., surface fluctuations, in the original shape is removed, while low-frequency (high-level) shape characteristics, e.g., branching, is retained and even enhanced in the 2D projection. Figure 6.2 illustrates this property. The five toes of the foot mesh, shown in plot (a), form branches. Plot (b) shows its 2D L-projection. As observed, the "toe branches", as a low-frequency structure, is extracted and enhanced in the 2D projection space.

6.2.2 Geometry Projection

Although projecting using the L operator is able to reveal the structure segmentability of a shape, it may fail to capture geometry segmentability information since L is only defined by mesh connectivity. Figure 6.3 depicts such a situation. We see that the original mesh (a) is clearly segmentable due to the concavity between the handle part and the body part. However, since there is no branching structure in place, its L-projection (b) does not exemplify strong segmentability; this could introduce difficulty to the subsequent analysis. To resolve this issue, we design a new Laplacian operator M. M is defined similar to L as $M = D - T$, with the only exception that the entries of T herein need to take into

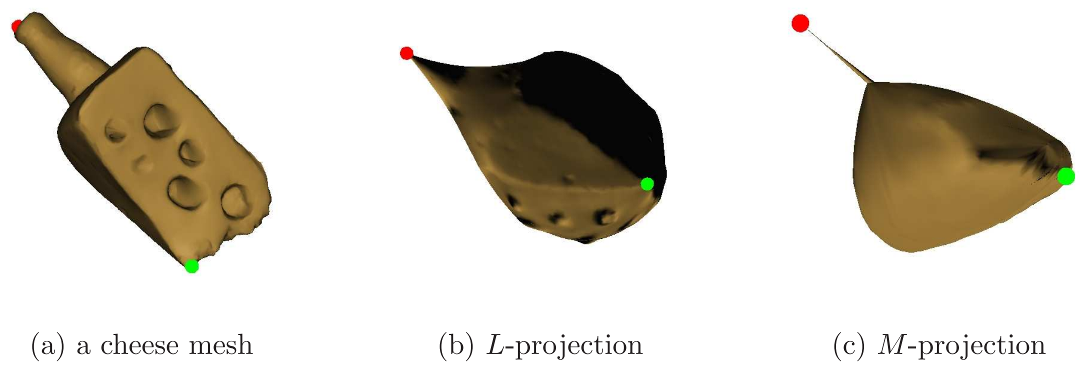
(a) a cheese mesh (b) L-projection (c) M-projection

Figure 6.3: Segmentability of a cheese model is better revealed in the M-projection.

consideration the geometric information of a mesh surface. To this end, we define for edge $e = (i, j)$ its corresponding entry T_{ij} as

$$T_{ij} = \begin{cases} (|\kappa_i| + |\kappa_j|) \cdot |\langle \mathbf{e}, \mathbf{z} \rangle| \cdot l & \text{if } \kappa_i < 0 \text{ or } \kappa_j < 0, \\ \epsilon & \text{otherwise.} \end{cases}$$

κ_i and κ_j, computed as in [26], are the minimal principal curvatures at vertices v_i and v_j, $\mathbf{z}$ is the normalized average of the principal curvature directions of κ_i and κ_j, $\mathbf{e}$ is the normalized direction of e, and l is the length of e divided by the average length of all edges in this mesh. When $\kappa_i \geq 0$ and $\kappa_j \geq 0$, implying local convexity at e, we set $T_{ij} = \epsilon = 0.1$ to simply maintain vertex connectivity information in T. If (i, j) is not an edge, $T_{ij} = 0$. We see that if an edge is roughly aligned up with the local minimal curvature direction and any of the end vertices of this edge has negative minimal curvature, this edge would carry a large weight. We examine the effect of this weighting scheme on the projection as follows.

Consider any matrix $Y \in \mathbb{R}^{n \times k}$, it can be shown that

$$\frac{1}{2} \sum_{ij} T_{ij} ||y_i - y_j||^2 = \mathrm{tr}\big(Y^T (D - T) Y\big) = \mathrm{tr}(Y^T M Y), \tag{6.1}$$

where $Y = [y_1^T | y_2^T | \ldots | y_n^T]^T$ and each y_i, a row vector, is seen as a k-dimensional point. Let $M = \Xi \Lambda \Xi^T$ be the eigenvalue decomposition. The first (smallest) k eigenvectors of Ξ can be denoted, in column and row vector format, by $\Xi_{[1\ldots k]} = [\xi_1 | \xi_2 | \ldots | \xi_k] = [u_1^T | u_2^T | \ldots | u_n^T]^T$. It is known that when $Y = \Xi_{[1\ldots k]}$, i.e., $y_i = u_i, i = 1 \ldots k$, Equation 6.1 is minimized, under the constraint that the columns of Y are of unit length. With a large weight T_{ij}, Equation 6.1 should be minimized with small $||y_i - y_j||^2$. Since u_i and u_j are the minimizers, it induces that $||u_i - u_j||^2$ should be small, given a large T_{ij}.

Similar to Section 6.2.1, we obtain the projection $\tilde{X} = \Xi_{[1...k]}\Xi^T_{[1...k]}X$. It follows that the squared distance between two embedded vertices, $\tilde{x}_i$ and $\tilde{x}_j$ (two rows of $\tilde{X}$), is

$$||\tilde{x}_i - \tilde{x}_j||^2 = ||(u_i - u_j)\Xi^T_{[1...k]}X||^2 \leq ||u_i - u_j||^2||\Xi^T_{[1...k]}X||^2.$$

Given a large T_{ij}, $||u_i - u_j||^2$ is relatively small as reasoned above; therefore $||\tilde{x}_i - \tilde{x}_j||^2$ should also be relatively small, since $||\Xi^T_{[1...k]}X||^2$ is a constant. Thus for each pair of vertices, a larger T_{ij} suggests that their embeddings should be closer to each other. With the way the weights in T are defined, mesh vertices from a concave region are to be pulled closer to each other after the projection, helping form a constriction in the projection space between the two parts. This is illustrated in Figure 6.3(c), where we see that the concavity between the handle part and the body part of the cheese mesh leads to an aggressively constricted region in the M-projection, thus a greatly enhanced segmentability. It is worth pointing out that the concavities from the circular dents in the body part do not contribute to any segmentability, as they are "contained" within the shape and do not influence the resulting outer contour of the M-projection. Therefore, only the handle part, but not the dents, is to be segmented off the body part and this is intuitive (see Figure 6.19(b)).

6.2.3 Contour Extraction and Pre-processing

Our segmentability analysis is based on the outer contour of a 2D L-projection or a M-projection. Therefore we need to extract the contour of a projection first. This is done by rendering in black the faces of the projected mesh against a white background and tracing the outer boundary of the resulting binary image. In our application, we set the image resolution to 200×200. As the mesh is connected, so is the rendered region. Ignoring interior holes, which can be caused by the openings of the mesh piece, we obtain a single continuous outer contour of the 2D projection. Since the traced contour consists of discrete pixels and is usually jaggy, we smooth it first using truncated Fourier descriptors (FDs)[142]. Intuitively, low-frequency FDs correspond to the smooth and approximate shape of the contour, while high-frequency FDs correspond to local noise on the contour. In our smoothing, low-frequency FDs are added one by one until the reconstruction error (measured by the overall distance between corresponding points from the reconstructed contour and the original contour) falls below a threshold, which is set to be 0.5% of the scale of the contour.

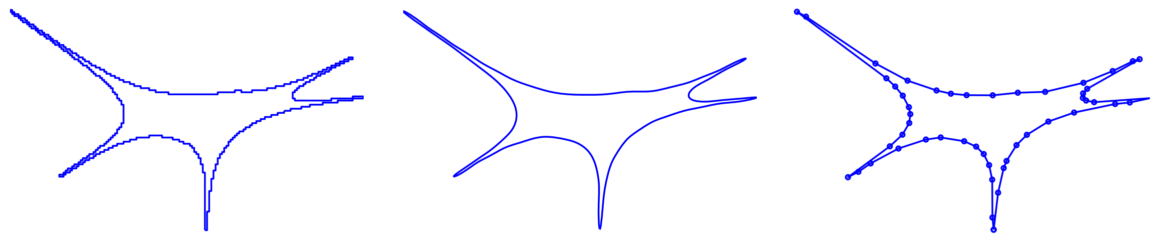

(a) original contour (b) smoothed contour (c) simplified contour

Figure 6.4: Contours obtained from the L-projection of the foot model. Plot (a) shows the original contour with 742 vertices traced from the rendered mesh. The smoothed contour is shown in plot (b). Plot (c) is the simplified contour, with its 50 vertices drawn as small dots for illustration purpose.

The next preprocessing step is to simplify the smoothed contour, in order to reduce the computational cost of the subsequent operations. Many contour simplification algorithms are available. We adopt the greedy algorithm described by Latecki and Lakämper [67]. Roughly speaking, the simplification is done by iteratively removing a contour vertex that changes the shape of the current contour the least. In our application, we always reduce the size of a contour down to 50 vertices. Figure 6.4 shows the contours obtained from the L-projection in Figure 6.2(b).

From now on, we denote the smoothed and simplified contour by ζ.

6.2.4 Segmentability Analysis

Segmentability Score We relate the segmentability of a mesh to the segmentability of the 2D shape enclosed by its corresponding ζ. For a 2D shape, its segmentability is clearly related to its convexity/concavity: the more concave a shape is, the more segmentable it tends to be. Denote by $A(\zeta)$ the area enclosed by a contour ζ; the perimeter and the convex hull are denoted by $P(\zeta)$ and $CH(\zeta)$, respectively. The following convexity measures are well-known and simple to compute:

$$C_1(\zeta) = \frac{A(\zeta)}{A(CH(\zeta))}, \qquad C_2(\zeta) = \frac{P(CH(\zeta))}{P(\zeta)}.$$

It is easy to see that $C_1, C_2 \in (0, 1]$ and they are equal to 1 if and only if ζ is convex. Past research has shown that neither measure provides a completely satisfactory measure of convexity: C_1 struggles with boundary defects that do not impact shape area, and C_2

is sensitive to noise. However, they appear to *complement* each other [149]. Motivated by this, we propose to use the following simple extension as our convexity measure,

$$C(\zeta) = \max\{C_1(\zeta), C_2(\zeta)^{w_{cvx}}\},$$

where the exponent $w_{cvx} \geq 1$ not only ensures that $C \in (0, 1]$ and $C = 1$ if and only if ζ is convex, but also addresses possible differences in scale between C_1 and C_2. Throughout our experiments, we set $w_{cvx} = 4$.

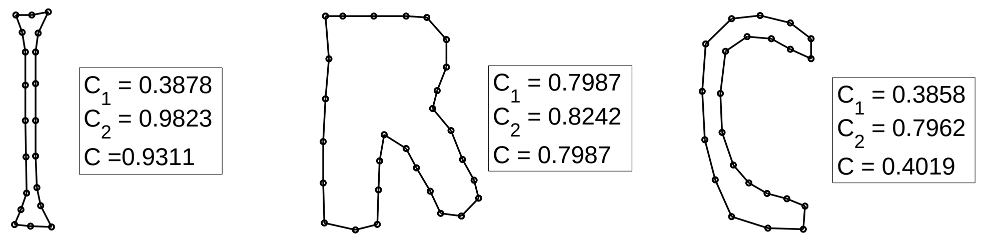

Figure 6.5: Convexity measures of three shapes based on area and perimeter.

For a telling example which illustrates the advantage of our convexity measure, consider the rough outlines of the letters **I** and **R**, shown in Figure 6.5. By C_1, **I** is deemed to be more concave and thus more segmentable than **R**; this is counter-intuitive. With the new measure C, $C_2^{w_{cvx}}$ would prevail over C_1 for **I** and return a more reasonable result. The new measure can also properly rank the convexity between the outlines of the letters **I** and **C**. The potentially large discrepancies between C_1 and C_2, e.g., for **I**, explains our preference of using the max operator over a convex combination. The inability of either C_1 or C_2 to properly capture the convexity of a shape should not diminish the utility of the other.

Finally, with the convexity measure in place, we define the segmentability score, $S(\zeta)$, of a contour ζ as

$$S(\zeta) = 1 - C(\zeta). \tag{6.2}$$

Clearly, $S(\zeta) \in [0, 1)$ and the larger $S(\zeta)$ is, the more segmentable ζ is.

Articulation Invariance Despite a correlation between convexity and segmentability, they are not exactly the same concept. Naturally, the result of structural-level segmentation should be invariant to shape articulation and this should also hold for a segmentability measure. However, the same cannot be said about convexity/concavity. The effect of bending

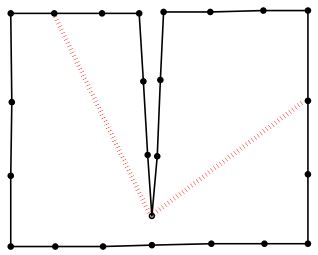

(a) $C = 0.9557$.

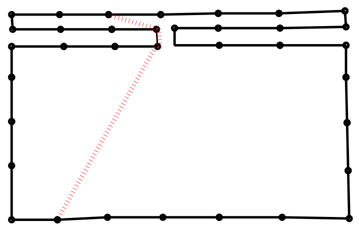

(b) $C = 0.9084$.

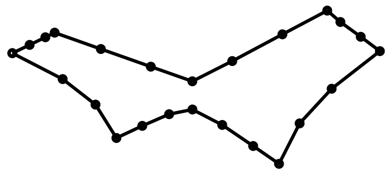

(c) $C = 0.7809$.

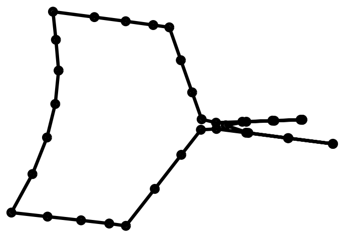

(d) $C = 0.6275$.

Figure 6.6: Use of MDS to enhance the performance of segmentability measure. The shapes in (a) and (b) compromise the effectiveness of C. However, they can be "stretched out" via MDS using inner distances, as shown in (c) and (d), respectively, for more intuitive results.

can compromise the performance of the convexity measure C, and hence the segmentability measure S. The contours illustrated in Figure 6.6(a, b) give two such examples: though the two contours are sufficiently segmentable (due to the deep concavity), their convexity measures are in fact close to 1 (segmentability close to 0).

Our solution to this problem involves normalizing contours with respect to shape articulation, using Multi-Dimensional Scaling (MDS) [27]. Roughly speaking, given pairwise distances between a set of points, MDS embeds the points in Euclidean space, while preserving the original distances through the new Euclidean distances as much as possible. If there is a distance measure between contour vertices that is insensitive to bending, we can use MDS based on this distance measure to re-embed the contour vertices, and the resulting contours are therefore invariant to articulation. We resort to inner distances [77] to achieve this goal. The inner distance between two vertices u and v on a contour ζ is defined as the length of the shortest path between u and v which lies in the interior of ζ.

As shown in Figure 6.6 (a) and (b), the red dotted lines depict the shortest paths between the corresponding contour vertices inside the shape. Ling and Jacob [77] first propose the use of inner distances for the retrieval of articulated shapes and they have shown that inner distances are insensitive to shape articulation.

A natural way to compute pairwise inner distances between n contour vertices is to first construct a visibility graph, where the nodes are the contour vertices and each pair of nodes are connected by an edge if and only if the line segment between them are inside the contour. After the visibility graph is constructed, the inner distance between any two contour vertices is simply their shortest graph distance in the visibility graph. A simple implementation of this method has a complexity of $O(n^3)$, due to the construction of the visibility graph. Theoretically speaking, there is an optimal $O(n)$ scheme for finding inner distances emanating from a vertex, leading to an overall complexity of $O(n^2)$. However, this scheme relies on the linear-time polygon triangulation algorithm of Chazelle [22], which is generally believed to be extremely hard to implement. We have opted to implement the simplistic $O(n^3)$ approach since each contour ζ we need to analyze has only 50 vertices after the contour simplification.

After the pairwise inner distances are computed, we perform MDS to embed the contour onto a plane. The inner distances are approximated by Euclidean distances via MDS and as such, the contour is normalized against bending. Two results of MDS via inner distances are shown in Figure 6.6(c, d). The convexity measure C can then be applied to the normalized contours, successfully recognizing the two shapes with high segmentability scores.

Segmentability Analysis Procedure As illustrated in Figure 6.1, supposing the mesh pieces that have not been classified as output parts are stored in the set $\mathcal{Q}$, our algorithm always selects from $\mathcal{Q}$ the mesh piece $\mathcal{M}_c$ with the largest surface area for the current segmentation. Figure 6.7 recapitulates the segmentability analysis on $\mathcal{M}_c$, where returned value TRUE indicates $\mathcal{M}_c$ is segmentable and vice versa. η $(= 0.1)$ is the segmentability threshold value.

To consider both structure and geometry segmentabilities, we conduct contour analysis on ζ_L and ζ_M in order. For each contour, we also examine its normalized counterpart, ζ_L^* or ζ_M^*, via MDS to achieve articulation invariance. If all the four thresholding tests fail (FALSE returned), $\mathcal{M}_c$ is deemed not segmentable and becomes an output part; otherwise $\mathcal{M}_c$ is to be segmented by our salience-driven cut algorithm, which we discuss next.

1. Compute ζ_L, the contour of the L-projection of $\mathcal{M}_c$. If $S(\zeta_L) > \eta$, return TRUE.
2. Compute the MDS-embedding ζ_L^* of ζ_L via inner distances. If $S(\zeta_L^*) > \eta$, return TRUE.
3. Compute ζ_M, the contour of the M-projection of $\mathcal{M}_c$. If $S(\zeta_M) > \eta$, return TRUE.
4. Compute the MDS-embedding ζ_M^* of ζ_M via inner distances. If $S(\zeta_M^*) > \eta$, return TRUE.
5. return FALSE.

Figure 6.7: Contour segmentability analysis procedure.

6.3 Face Linearization

Once the current mesh piece $\mathcal{M}_c$ is deemed segmentable, it is subject to the actual segmentation. The segmentation procedure has two steps: arrange the faces of $\mathcal{M}_c$ in a sequence, and search through the sequence to obtain the most salient cut. We call the first step face linearization and discuss it in this section. The second step is discussed in Section 6.4.

Recall that we have defined the part-aware graph $\tilde{G}_c$ in Section 3.5 and the induced graph distances have been used for the segmentation algorithm in Chapter 4. Supposing $\tilde{G}_c$ is the corresponding part-aware graph of $\mathcal{M}_c$, we want to use $\tilde{G}_c$ again to derive the face sequence for $\mathcal{M}_c$. However, we cannot construct $\tilde{G}_c$ for $\mathcal{M}_c$ in the same way any more. This is because the current algorithm segments iteratively and the intermediate mesh piece $\mathcal{M}_c$ is open. Since an open mesh in general does not admit a well-defined enclosed volume, the VSI-distance component in $\tilde{G}_c$ is no longer robust. Therefore we only consider the geodesic and angular distances and build the corresponding graph $\tilde{G}'_c$ similarly. Although $\tilde{G}'_c$ is no longer equipped with VSI-distance, the face linearization and salience-driven cut are still able to ensure high quality segmentation results.

In order to linearize the faces effectively so that the meaningful cuts are preserved in the resulting sequence, we first need to find two sample faces which are from two different parts of $\mathcal{M}_c$. We discuss this issue in Section 6.3.3. Assuming we have already obtained $\tilde{G}'_c$ and the two sample faces f_s and f_t, the computation of the sequence per se turns out to be fairly simple. Let's denote by d_{is} and d_{it} the graph distances in $\tilde{G}'_c$ between f_i and f_s, f_i

and f_t, respectively. We then define a vector $\tilde{\mathbf{e}}$, where $\tilde{\mathbf{e}}^{(i)} = d_{is} - d_{it}$. By sorting $\tilde{\mathbf{e}}$,

$$[\tilde{\mathbf{e}}_s, \varrho] = \mathrm{sort}(\tilde{\mathbf{e}}), \tag{6.3}$$

we have $\tilde{\mathbf{e}}_s$ as the sorted vector, say in ascending order, and ϱ as the index vector of $\tilde{\mathbf{e}}_s$. For example, if $\tilde{\mathbf{e}}^{(a)} \leq \tilde{\mathbf{e}}^{(b)}$, a would proceed b in ϱ. ϱ is the face sequence we seek.

Although simple, the sequence ϱ has a variety of nice features that make it suitable to be used for our salience-driven cut search. We discuss this sequence in detail in the following.

6.3.1 Derivation and Properties

In Chapter 5, we have adopted sub-sampling and the Nyström method to compute the approximate eigenvectors of W to reduce complexity. If we sample only two faces, the sub-block A in Equation 5.1 reduces to $[1\ \alpha; \alpha\ 1]$, with $0 \leq \alpha \leq 1$ being the affinity between sample faces f_s and f_t. The sub-block B can be written as

$$B = \begin{bmatrix} \cdots & x_i & \cdots \\ \cdots & y_i & \cdots \end{bmatrix}, \tag{6.4}$$

where x_i (y_i) is the affinity between f_i and f_s (f_t). For the simplicity of notation, we assume that the faces are re-indexed so that f_s and f_t are the first two faces and f_i, $3 \leq i \leq n$, is an un-sampled face. Note that this does not affect the properties of ϱ.

Following the formula in Equation 5.2, it is not hard to show that the two approximated eigenvectors using only two samples are

$$\tilde{E} = \frac{1}{2} \begin{bmatrix} 1 & -1 \\ 1 & 1 \\ \cdots & \cdots \\ \frac{y_i + x_i}{1+\alpha} & \frac{y_i - x_i}{1-\alpha} \\ \cdots & \cdots \end{bmatrix}. \tag{6.5}$$

So the component-wise ratio of the second eigenvector ($\tilde{E}_{\cdot 2}$) to the first eigenvector ($\tilde{E}_{\cdot 1}$) is

$$\mathbf{e} = \left[-1,\ 1,\ \ldots,\ \left(\frac{y_i - x_i}{y_i + x_i} \cdot \frac{1+\alpha}{1-\alpha} \right), \ldots \right]. \tag{6.6}$$

If we consider $\mathbf{e}$ as a 1D embedding of the mesh faces, we have $\mathbf{e}(f_s) = -1$, $\mathbf{e}(f_t) = 1$, and $\mathbf{e}(f_i) = \frac{y_i - x_i}{y_i + x_i} \cdot \frac{1+\alpha}{1-\alpha}$. Let's write the affinities between the faces based on their distances as $\alpha = e^{-d_{st}/2\sigma^2}$, $x_i = e^{-d_{is}/2\sigma^2}$, and $y_i = e^{-d_{it}/2\sigma^2}$, where d_{is} and d_{it} are mentioned above, and d_{st} is the graph distance between sample faces f_s and f_t. We prove two properties of $\mathbf{e}$.

Proposition 6.1. $\forall f_i, \mathbf{e}(f_s) \le \mathbf{e}(f_i) \le \mathbf{e}(f_t)$. *This means that the embeddings of the two sample faces f_s and f_t are at the two ends of* $\mathbf{e}$.

Proof. We only prove $\mathbf{e}(f_i) \le \mathbf{e}(f_t)$. $\mathbf{e}(f_s) \le \mathbf{e}(f_i)$ can be proved similarly.

$$\begin{aligned}
\mathbf{e}(f_i) \le \mathbf{e}(f_t) &\Leftrightarrow \frac{y_i - x_i}{y_i + x_i} \cdot \frac{1+\alpha}{1-\alpha} \le 1 \\
&\Leftrightarrow (y_i - x_i)(1+\alpha) \le (y_i + x_i)(1-\alpha) \\
&\Leftrightarrow \alpha y_i - x_i \le -\alpha y_i + x_i \\
&\Leftrightarrow \alpha \le \frac{x_i}{y_i} \\
&\Leftrightarrow e^{-d_{st}/2\sigma^2} \le e^{(d_{it}-d_{is})/2\sigma^2} \\
&\Leftrightarrow -d_{st} \le d_{it} - d_{is} \\
&\Leftrightarrow d_{is} \le d_{it} + d_{st}.
\end{aligned}$$

Since the graph distance in $\tilde{G}'_c$ is a metric, satisfying the triangle inequality, the last inequality holds. This concludes our proof. □

Proposition 6.2. *Sorting vectors* $\mathbf{e}$ *or* $\tilde{\mathbf{e}}$ *produces the same face sequence.*

Proof. For $\mathbf{e}$, let's denote $F(f_i) = \frac{y_i - x_i}{y_i + x_i} \cdot \frac{1+\alpha}{1-\alpha}$. Representing $\beta = x_i/y_i$, we can also write $F(\beta) = \frac{1+\alpha}{1-\alpha} \cdot (1 - \frac{2}{1/\beta+1})$. Clearly $F(\beta)$ is monotone and inversely proportional to β. Meanwhile, as $\beta = e^{-d_{is}/2\sigma^2}/e^{-d_{it}/2\sigma^2} = e^{-(d_{is}-d_{it})/2\sigma^2}$, β is monotone and inversely proportional to $(d_{is} - d_{it})$. Therefore F is monotone and proportional to $(d_{is} - d_{it})$. This implies that except for the two sample faces, the face sequences obtained by sorting $\mathbf{e}$ and $\tilde{\mathbf{e}}$ are identical. Due to the triangle inequality, it is easy to see that $(d_{is} - d_{it})$ is minimized when $i = s$ and maximized when $i = t$. As a result, the two sample faces are sitting at the two ends of $\tilde{\mathbf{e}}$. Plus Proposition 6.1, we prove that the two sequences are the same. Note that we have assumed that neither $\mathbf{e}$ nor $\tilde{\mathbf{e}}$ has equal entries. If they do, we can mandate that the sorting algorithm be stable to ensure the same sequence. □

With Proposition 6.1 and Proposition 6.2, we have:

- f_s and f_t are always at the two ends of sequence ϱ, and
- the sequence ϱ from Equation 6.3 is the same with the sequence obtained by sorting $\mathbf{e}$ from Equation 6.6.

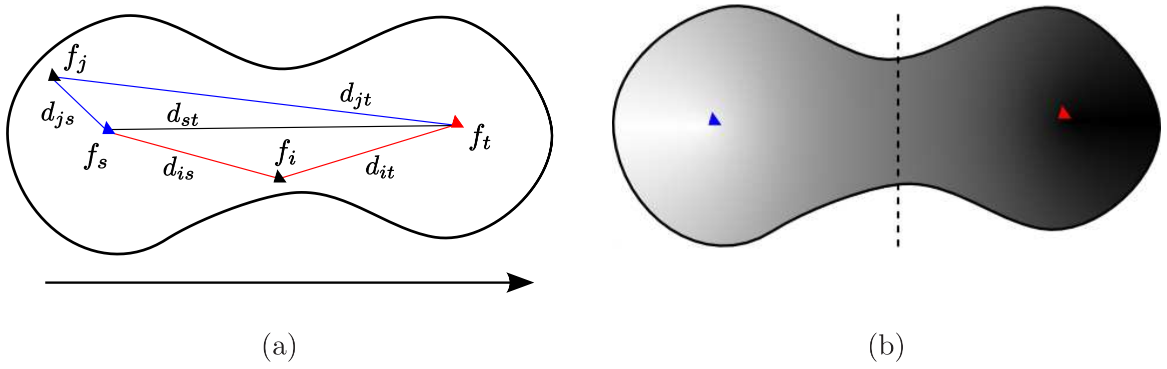

Figure 6.8: Characteristics of a face sequence produced for a synthetic 2D shape. Plot (a) shows the shortest paths between faces f_i, f_j and the sample faces f_s and f_t, where the arrow at the bottom indicates the rough direction of the corresponding face sequence. In plot (b), the sequence is shown with gray-scale colors: each jump in the sequence causes an equal shift in the color space. The meaningful cut is available in such a sequence, as indicated by the vertical dashed line.

First, this implies that we must select two sample faces from two different parts; otherwise, counter-intuitive results would be produced, since any cut sought from ϱ would have to separate the samples which are at the two ends of ϱ into different parts. Secondly, as $\mathbf{e}$ is spectral-based, ϱ can be considered spectral-based as well.

As a concrete example, Figure 6.8 illustrates how the faces from a synthetic 2D shape are arranged in ϱ, given a sample pair. In this toy example, the distance we use is the inner distance (Section 6.2.4). For faces f_i and f_j as configured in plot (a), it is apparent that $d_{js} - d_{jt} < d_{is} - d_{it}$; therefore f_j is closer to f_s in ϱ than f_i is to f_s. The face sequence roughly follows the order: $f_s \to \ldots \to f_j \to \ldots \to f_i \to \ldots \to f_t$. Plot (b) color-codes the corresponding sequence, where brighter colors indicate positions closer to f_s. The migration of the brightness attests to our analysis.

There is no doubt that arranging faces in ϱ could potentially eliminate some meaningful cuts. However, the cut producing the two parts from which the sample faces were selected are most likely to be well preserved. Figure 6.9 gives an intuitive explanation. In plot (a), let's first presume that the two sample faces f_s and f_t are from the tips of the second and the third fingers, which is what our sampling approach (Section 6.3.3) tends to do. We also assume that the joint region between the second finger and the palm contains a single face f_i. Based on the previous analysis, we know that f_s is at one end of ϱ and, clearly, the faces between f_s and f_i on the surface sit between f_s and f_i in ϱ. We have shown that the position of f_i in ϱ is

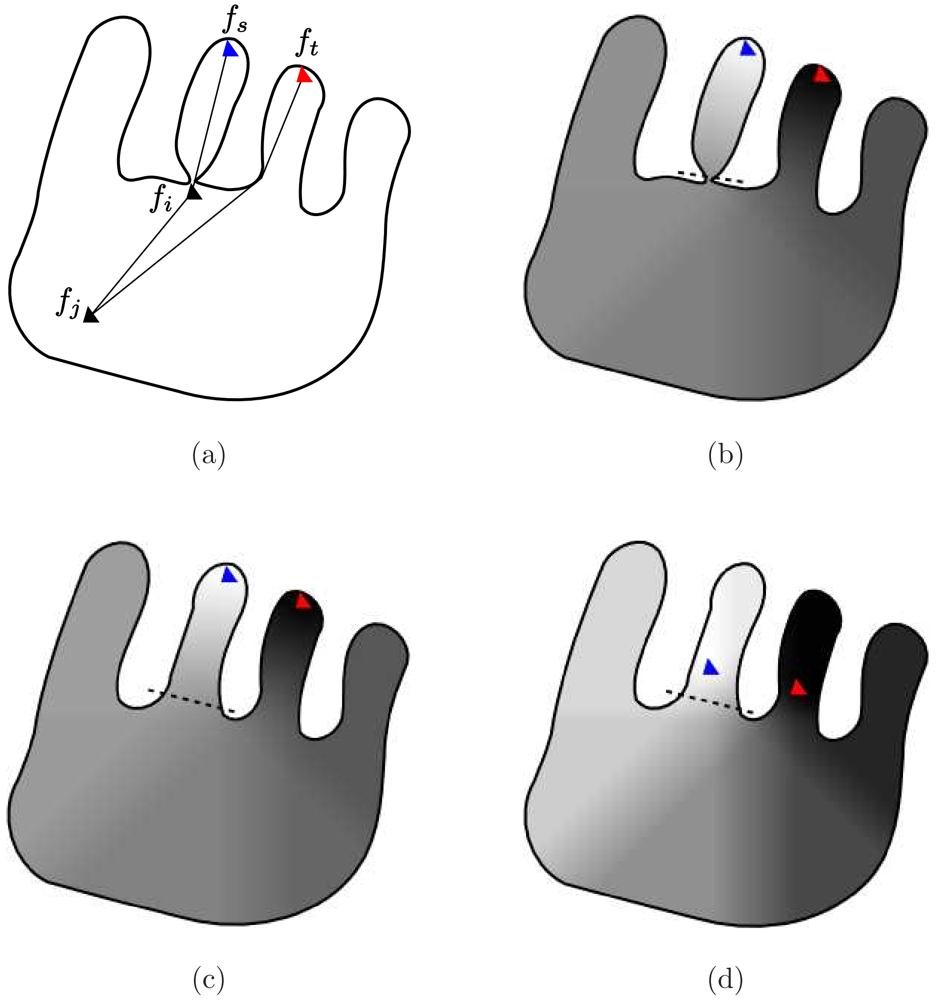

Figure 6.9: The effectiveness of the face sequence in preserving desirable cuts. (a): the shortest paths between faces in an ideal case where the second finger has a one-face joint region with the palm. (b): color coding for the face sequence of the ideal case. (c-d): color coding for the face sequences produced by two sample pairs in a realistic case where the joint region is wide. The dashed lines indicate the meaningful cuts preserved in the corresponding sequences.

determined by $d_{is} - d_{it}$. Since $d_{is} - d_{it} = (d_{is} + d_{ij}) - (d_{it} + d_{ij}) = d_{js} - (d_{it} + d_{ij}) \leq d_{js} - d_{jt}$, where the last step is based on the triangle inequality, i.e., $d_{it} + d_{ij} \geq d_{jt}$, f_j must sit between f_i and f_t in ϱ. This is true for any f_j outside the second finger; therefore, a clean cut which segments the second finger off the palm is guaranteed in ϱ. Plot (b) shows the color coding of ϱ. In reality such an ideal case seldom exists and a joint region between parts is often wide, as shown in plot (c). However, the face ordering from the ideal case can still be well maintained in the resulting sequence from (c), thanks to the use of geodesic distance and the continuity of our distance metric defined on surfaces. This is why a similar color coding is observed in (c). Plot (d) shows the sequence when both sample faces are placed near the part boundaries. It is not hard to similarly verify that the sequence from the blue triangle side does not invade beyond the dashed line into the palm region until the entire second finger is covered. In all these cases, the desirable cuts indicated by the dashed lines are thus always present in the corresponding face sequences.

That being said, the face sequence ϱ can effectively preserve meaningful cuts, provided that the two samples are chosen from two different parts (Section 6.3.3). In our experiments, we have found that such a sequencing technique works quite well. Since part boundaries typically follow concave regions, the shortest path between two faces often travels through the openings (if exist) of concave regions. In other words, concave regions essentially help narrow down the joint regions between parts (similar to the ideal case in Figure 6.9(a)), enhancing the effectiveness of ϱ.

With the face sequence ϱ of the current mesh piece $\mathcal{M}_c$ computed, we discuss how to find the best cut from ϱ to divide $\mathcal{M}_c$ into two parts in Section 6.4. In the next section, we examine how ϱ relates to Normalized Cut. This section can be safely skipped without affecting the understanding of subsequent sections.

6.3.2 Relation to Normalized Cut

Normalized Cut [115] is probably one of the most well-known spectral clustering techniques. In this section, we show the relationship between our face sequence ϱ and the Normalized Cut. As briefed in Section 2.3.1, Normalized Cut seeks the second smallest eigenvector of the generalized eigenvalue problem

$$(D - W)\mathbf{v} = \lambda D\mathbf{v}. \tag{6.7}$$

Recall that D is a diagonal matrix with its diagonals being the row sums of W. Then the entries of this second smallest eigenvector are thresholded to produce two groups: entries with values above the threshold belong to one group and entries with values below the threshold belong to the other group. Weiss [131] defines the normalized affinity matrix as

$$N = D^{-\frac{1}{2}} W D^{-\frac{1}{2}}, \tag{6.8}$$

and it is shown that $\breve{\mathbf{e}}$, the component-wise ratio of the second largest eigenvector to the first largest eigenvector of N, is equal to the second smallest generalized eigenvector of Equation 6.7. Therefore, thresholding $\breve{\mathbf{e}}$ is equivalent to applying the Normalized Cut.

In order to reduce the complexity involved in dealing with N, the Nyström method could also be applied to N as in Section 5. Let's denote by $\hat{\mathbf{e}}$ the approximate eigenvector for $\breve{\mathbf{e}}$. In Appendix A, we prove that sorting $\hat{\mathbf{e}}$ or $\tilde{\mathbf{e}}$ produces the same face sequence, if only two samples are used. Having said that, we make the observation that the face sequence ϱ we derive for the salience-driven cut is the same with that derived from the Normalized Cut under our sampling configuration. From a different perspective this property speaks well for the merit of ϱ. Of course, such a property alone does not guarantee an effective sequence; it is only so when the two samples are selected appropriately.

6.3.3 Sample Selection

We have assumed that the two sample faces f_s and f_t are from two different parts of the mesh piece $\mathcal{M}_c$, so that the face sequence ϱ can preserve the meaningful cuts. We discuss in this section how to find two faces from different parts robustly.

One naive solution is to find two faces which are farthest away in $\tilde{G}'_c$. This can be efficiently carried out approximately through the farthest-point sampling scheme described in Figure 5.3. The rationale behind this is that distant faces tend to reside on different parts. However, this method easily fails in practice because the two samples can be placed in different (deep) concave regions from a single part. Such an example is the cheese model shown in Figure 6.3(a). Because of the deep concavities caused by the circular dents, the two samples farthest apart are actually from two of those dents. However, the two salient parts that we perceive are the handle part and the body part, as segmented out in Figure 6.19(b).

In Figure 6.7, we obtain a contour in each of the first four steps for segmentability analysis. Suppose that the segmentability test passes in one of the four steps and the corresponding contour is ζ. As ζ reveals and enhances the part structure of $\mathcal{M}_c$, our sampling scheme can make use of ζ to find samples from different parts of $\mathcal{M}_c$ robustly. Briefly, we find two contour vertices $\tilde{s}$ and $\tilde{t}$ that are from different parts of ζ and map them back to the surface of $\mathcal{M}_c$ to locate f_s and f_t.

Before describing the details, we first introduce the concept of *integrated bending score* or *IBS* at a vertex along a contour with respect to the whole contour. Given a vertex p on ζ, its IBS is defined as

$$\Omega_p = \int_{q\in\ \zeta-\{p\}} \frac{I_{pq}}{E_{pq}} dq,$$

where E_{pq} and I_{pq} denote the Euclidean and inner distances (Section 6.2.4) between contour vertices p and q, respectively. Note that $\frac{I_{pq}}{E_{pq}} \in [1, +\infty]$, and it roughly describes how much the inner path between p and q bends. Intuitively, if many inner paths emanating from p bend significantly, Ω_p tends to be large, suggesting that p is likely to be on a part separated by concave regions along ζ. Since ζ is piece-wise linear, we compute the above integral per line segment $\overline{ij}$ in ζ, namely, $\Omega_p = \sum_{\overline{ij}\in\zeta} \Omega_p(\overline{ij})$.

To compute $\Omega_p(\overline{ij})$, we first calculate the inner and Euclidean distances from vertex p to vertices i and j; these are I_{pi}, I_{pj}, E_{pi}, and E_{pj}. We rely on a linear interpolation along $\overline{ij}$ to estimate $\Omega_p(\overline{ij})$. Let l be the length of $\overline{ij}$, we have

$$\Omega_p(\overline{ij}) = \int_0^l \frac{I_{pi} + \frac{q}{l}(I_{pj} - I_{pi})}{E_{pi} + \frac{q}{l}(E_{pj} - E_{pi})} dp.$$

After some algebraic derivations, we arrive at

$$\Omega_p(\overline{ij}) = \frac{dbl + (ad - bc)\big(\ln(c + dl) - \ln(c)\big)}{d^2},$$

where $a = I_{pi}l$, $b = I_{pj} - I_{pi}$, $c = E_{pi}l$, and $d = E_{pj} - E_{pi}$.

Ideally, we would want to compute the IBS at a vertex with respect to a contour after the smoothing but before the simplification (Section 6.2.3). Our approach is aimed at achieving efficiency and it can introduce approximation errors of IBS from both contour simplification and linear interpolation. However, our experiments verify that these errors are negligible for the purpose of sampling.

The first sample $\tilde{s}$ is simply selected as the contour vertex which maximizes Ω_p, i.e., $\tilde{s} = \text{argmax}_p\{\Omega_p\}$. This way $\tilde{s}$ tends to reside on a peripheral part that is most isolated from the core of the shape enclosed by ζ. The second sample $\tilde{t} = \text{argmax}_q\{I_{\tilde{s}q}\}$ is selected as the contour vertex with the largest inner distance to the first sample $\tilde{s}$. Figure 6.10 uses

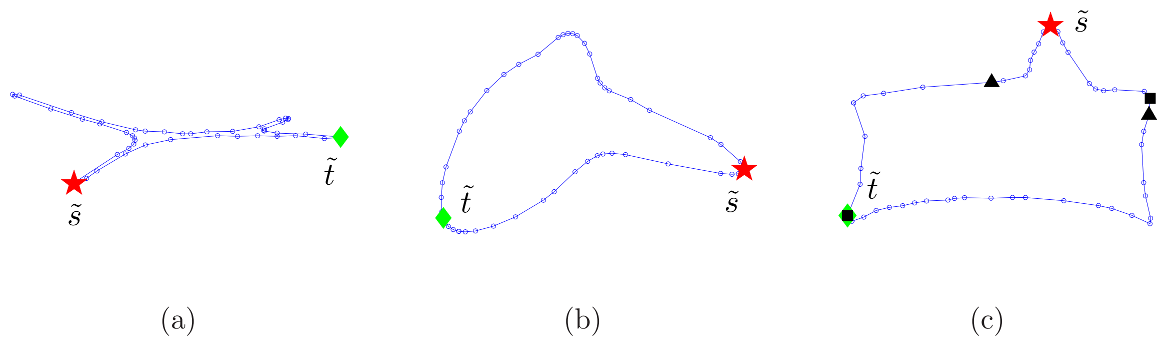

Figure 6.10: Results of IBS-based sampling on 2D contours: samples $\tilde{s}$ and $\tilde{t}$ are marked by stars and diamonds. In (c), we compare our algorithm against two variations of farthest-point sampling. The first one finds two vertices, marked by squares, which are mutually farthest apart in terms of inner distance. The second one picks two vertices, shown as triangles, which have the largest contour distance. The contour distance between two vertices is the sum of the magnitude of negative curvatures along the contour between the two vertices. Since each two vertices divide a contour into two sections, we consider the section giving the smaller distance.

three increasingly harder test cases to show the advantage of our sampling scheme. IBS utilizes global information and robust results are produced.

After $\tilde{s}$ and $\tilde{t}$ are found, they need to be mapped to two faces of $\mathcal{M}_c$. To this end, we find a mesh vertex v that is closest to $\tilde{s}$ in the corresponding 2D projection. Then from the faces incident to v, we select the one whose centroid is closest to v on $\mathcal{M}_c$. This is the first sample face f_s and the other sample face f_t is found similarly. Through this, we locate two faces from two different parts. It is not necessary to find sample faces that "accurately" correspond to $\tilde{s}$ and $\tilde{t}$. Real mapping examples on meshes can be found in Figure 6.15.

6.4 Salient Cut

Finally, we are ready to discuss how to find a good cut from the face sequence ϱ. Simply put, our strategy is to go through ϱ, measure the salience of the cut at each position, and choose the cut with the maximum salience.

6.4.1 Part Salience

The concept of salience has been proposed by Hoffman and Singh [51] to measure the strength of a part in terms of human perception. They conclude that part salience depends

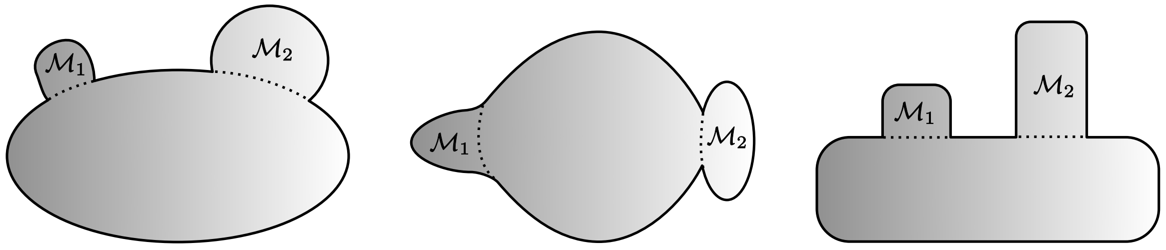

(a) size (b) boundary strength (c) protrusiveness

Figure 6.11: Effect of the three factors of part salience. In each plot, the salience of part $\mathcal{M}_2$ is higher than that of $\mathcal{M}_1$ because $\mathcal{M}_2$ is larger (a), has a more concave boundary (b), and is more protrusive (c).

on three factors: *size*, *boundary strength*, and *protrusiveness*. Figure 6.11 shows the effect of these three factors with 2D illustrations. We discuss how to measure them along with the cut search procedure in the following.

6.4.2 Salience-driven Cut Search

Salience has been utilized previously for mesh segmentation, such as by Lee et al. [69] and Page [93]. However, previous works only use it passively, in the sense that salience is measured to tell whether the computed parts are good enough; if not, the parts are rejected or post-processed somehow (e.g., merged with adjacent ones). Such a passive way of using salience does not make the most of it for segmentation. In our application, we measure salience along ϱ to find the best segmentation. In this sense, our method is salience-driven.

Supposing the current mesh piece $\mathcal{M}_c$ has n faces, there are $n-1$ locations to cut ϱ. Each cut location in ϱ corresponds to a segmentation on $\mathcal{M}_c$, dividing the surface into two regions. We judge the quality of a cut by the salience of the region with smaller size; this region is often a peripheral part that we wish to cut off the core body of $\mathcal{M}_c$. For measuring the size of a region, one may use its enclosed volume. However, as a region is typically open and its enclosed volume is not well-defined in general, we use its surface area to measure size. Denoting by $\mathcal{M}_s$ the region with smaller surface area, we define the salience of $\mathcal{M}_s$ as a weighted sum of the three salience factors:

$$\Upsilon(\mathcal{M}_s) = w_s\Upsilon_s(\mathcal{M}_s) + w_b\Upsilon_b(\mathcal{M}_s) + w_p\Upsilon_p(\mathcal{M}_s), \tag{6.9}$$

where $\Upsilon_s(\mathcal{M}_s), \Upsilon_b(\mathcal{M}_s), \Upsilon_p(\mathcal{M}_s) \in [0,1]$ represent the measures for size, boundary strength, and protrusiveness, respectively; $0 \leq w_s, w_b, w_p \leq 1$ and $w_s + w_b + w_p = 1$.

The size of $\mathcal{M}_s$ is defined relative to the entire $\mathcal{M}_c$, i.e.,

$$\Upsilon_s(\mathcal{M}_s) = \frac{\text{Area}(\mathcal{M}_s)}{\text{Area}(\mathcal{M}_c)}.$$

Letting $\partial\mathcal{M}_s$ be the set of the boundary edges between the two regions, boundary strength $\Upsilon_b(\mathcal{M}_s)$ is accumulated over $\partial\mathcal{M}_s$,

$$\Upsilon_b(\mathcal{M}_s) = \frac{1}{l} \sum_{e_i \in \partial\mathcal{M}_s} l_i \frac{\text{weight}(e_i)}{w_{max}},$$

where l_i is the length of edge e_i, $l = \sum_{e_i \in \partial\mathcal{M}_s} l_i$, weight$(e_i)$ is the edge weight defined as in Equation 4.20, and $w_{max} = \max(\{\text{weight}(e_i) \,|\, \forall e_i \in \partial\mathcal{M}_s\})$. Intuitively, if a boundary contains long edges from concave regions, then its strength is high. In order to achieve efficiency when searching through ϱ, we need to update the salience factors in constant time as a face is inserted to or removed from $\mathcal{M}_s$. By tracking faces and their edges during the searching, $\partial\mathcal{M}_s$, $\Upsilon_s(\mathcal{M}_s)$, and $\Upsilon_b(\mathcal{M}_s)$ can all be updated in constant time. Clearly, both $\Upsilon_s(\mathcal{M}_s)$ and $\Upsilon_b(\mathcal{M}_s)$ are in the range $[0, 1]$.

Following Hoffman and Singh [51], we use the surface area and the base area of $\mathcal{M}_s$ to measure its protrusiveness. The base area of $\mathcal{M}_s$ is the area subtended by $\partial\mathcal{M}_s$; we denote it by Area$(\partial\mathcal{M}_s)$. To update Area$(\partial\mathcal{M}_s)$ in constant when searching through ϱ, we follow the strategy from [93] to approximate Area$(\partial\mathcal{M}_s)$ and measure the protrusiveness of $\mathcal{M}_s$ as

$$\Upsilon_p(\mathcal{M}_s) = 1 - \frac{\text{Area}(\partial\mathcal{M}_s)}{\text{Area}(\mathcal{M}_s)} \approx 1 - \frac{4\sqrt{\lambda_1\lambda_2}}{\text{Area}(\mathcal{M}_s)}.$$

Area$(\partial\mathcal{M}_s)$ is approximated by $4\sqrt{\lambda_1\lambda_2}$, where λ_1 and λ_2 are the largest two eigenvalues of the covariance matrix of the mesh vertices contained in $\partial\mathcal{M}_s$. This means that Area$(\partial\mathcal{M}_s)$ is approximated by the area of the bounding box of the boundary vertices. Good approximation is achieved when the vertices in $\partial\mathcal{M}_s$ are coplanar. Notice that constant time update for $\Upsilon_p(\mathcal{M}_s)$ is possible since both the mean and the covariance matrix of a point set can be updated in $O(1)$ time after the insertion or deletion of a point. Specifically, let μ and Σ be the mean and covariance matrix of m points. When a new point p is added (deletion is similar), the mean and covariance matrix can be updated as

$$\mu' = \frac{m\mu + p}{m + 1}, \;\; \Sigma' = \Sigma + pp^T + m\mu\mu^T - (m + 1)\mu'\mu'^T.$$

Most of the time, $\mathrm{Area}(\partial\mathcal{M}_s) \leq \mathrm{Area}(\mathcal{M}_s)$. When a counter case happens, we simply set $\Upsilon_p(\mathcal{M}_s)$ to 0, since such cases are typically caused by sufficiently flat $\mathcal{M}_s$. Clearly, we have $\Upsilon_p(\mathcal{M}_s)$ also in the range $[0, 1]$.

The cut search procedure starts from one end of ϱ and visits one face at a time sequentially. The salience score in Equation 6.9 is updated along the way. Once the area of $\mathcal{M}_s$ becomes larger than half of the area of $\mathcal{M}_c$, $\mathcal{M}_s$ switches to its complement region. During the search, $\mathcal{M}_s$ is most likely to form a single component (a component refers to a connected surface region) as the graph distance from $\tilde{G}'_c$ used to derive ϱ is continuous. To address the problem that $\mathcal{M}_s$ may consist of disconnected regions, we could maintain a connected "meta" patch, and only work on this meta patch rather than work on all the faces of $\mathcal{M}_s$. In practice, however, we found this unnecessary. This is because disconnected faces in fact rarely emerge, and even if they do, their population is negligible. For better efficiency, we simply treat $\mathcal{M}_s$ as a single component and this does not affect the segmentation quality at all. Upon finishing searching, we select the cut that generates the largest salience score and split $\mathcal{M}_c$ into two parts. We denote these two parts by $\mathcal{M}'_s$ and $\overline{\mathcal{M}'_s}$, where $\mathcal{M}'_s \bigcap \overline{\mathcal{M}'_s} = \emptyset$ and $\mathcal{M}_c = \mathcal{M}'_s + \overline{\mathcal{M}'_s}$.

Figure 6.12 gives an example salience-driven cut search on a bird model, where the two samples are located at the tips of the two wings. Plot (a) shows the curves of the three equally weighted salience factors and the combined salience. The size curve is like a hat function because we always consider the smaller region when computing the salience. There are three major peaks along the salience (red) curve, all corresponding to meaningful cuts on the bird model as shown in plots (b-d). Since the largest salience, 0.71, is achieved at position 11116 in ϱ, the segmentation result shown in (d) is returned. In this particular example, the boundary strength factor plays the dominant role in determining the cut position.

Empirically, the edge boundary between $\mathcal{M}'_s$ and $\overline{\mathcal{M}'_s}$ could contain certain local artifacts. Before the actual splitting, we therefore add a boundary enhancement step to smooth the boundary locally, which is described in the next section. This smoothing operation is also capable of making both $\mathcal{M}'_s$ and $\overline{\mathcal{M}'_s}$ contain a single component, if they do not initially after the cut search procedure. We have never encountered a single case in which either of them consists of multiple components after the boundary enhancement step.

The final question about the cut search procedure is how to weight the three salience factors in Equation 6.9. Through experimental study, we observe that the size factor should take the least weight. Depending on whether it is the outer contour of an L-projection or

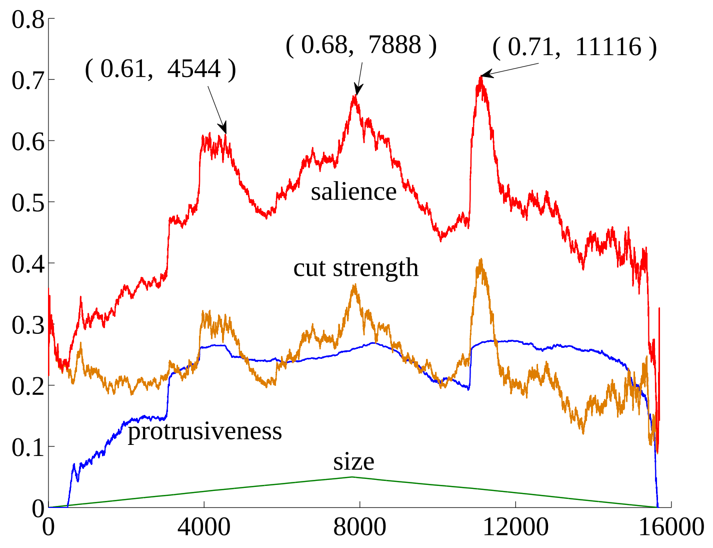

(a) salience curves

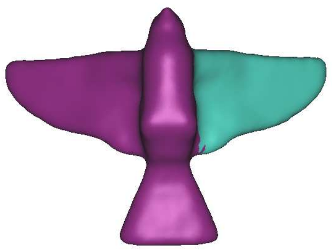

(b) position 4544

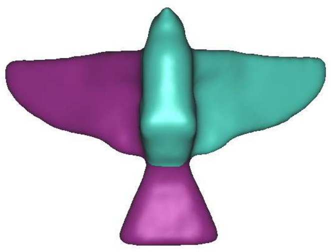

(c) position 7888

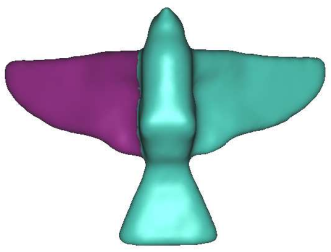

(d) position 11116

Figure 6.12: An example of salience-driven cut search. In plot (a), the curves of the three salience factors and the combined salience are shown, where the x-axis is the position in the face sequence ϱ and y-axis is the salience score. We identify three major peaks indicated by the arrows; their salience scores and positions are given in the brackets. Plots (b-d) show the three segmentations on the mesh surface with respect to the three peaks identified.

an M-projection that has passed the segmentability test (see Figure 6.7), either w_p or w_b should be emphasized more. Specifically, if ζ is considered segmentable via an M-projection (L-projection), it implies that the current segmentability is mainly caused by concavity (protrusion), therefore w_b (w_p) should assume more weight.

6.4.3 Boundary Enhancement

The initial salient cuts found in the previous section often demonstrate high quality. Sometimes, however, local artifacts may be present along the boundary between $\mathcal{M}'_s$ and $\overline{\mathcal{M}'_s}$. We utilize morphological operations to fix such local artifacts.

Mathematical morphology has been studied in image processing for a long time. One is referred to [48] for more details. In our application, we are only interested in two basic morphological operations: *erosion* and *dilation*. Let $\mathcal{I}$ be an integer grid, $\mathcal{A}$ a binary image on $\mathcal{I}$, and $\mathcal{B}$ a structuring element, the erosion of $\mathcal{A}$ by $\mathcal{B}$ is defined as

$$\mathcal{A} \ominus \mathcal{B} = \{z \in \mathcal{I} \mid \mathcal{B}_z \subseteq \mathcal{A}\}, \tag{6.10}$$

where $\mathcal{B}_z$ is the translation of $\mathcal{B}$ by a vector z, i.e., $\mathcal{B}_z = \{b + z | b \in \mathcal{B}\}$, $\forall z \in \mathcal{I}$. Intuitively, the erosion can be understood as the set of all grid points that the center of the structuring element $\mathcal{B}$ can reach while it moves and is completely contained inside $\mathcal{A}$. The dilation of $\mathcal{A}$ by $\mathcal{B}$ is defined as

$$\mathcal{A} \oplus \mathcal{B} = \bigcup_{b \in \mathcal{B}} \mathcal{A}_b, \tag{6.11}$$

where $\mathcal{A}_b = \{a + b | a \in \mathcal{A}\}$. Similarly, the dilation can be thought as the set of all grid points that are covered by $\mathcal{B}$ when the center of $\mathcal{B}$ moves inside $\mathcal{A}$. By first running dilation and then erosion (this combination is called *closing*), we could fix some local boundary artifacts. Figure 6.13 illustrates this idea. In plot (a), the boundary (red curve) between the gray region and the white region has a local jaggedness in the middle. After a dilation by a square as the structuring element, the new boundary is shown in plot (b). Finally in (c), an erosion takes away the green elements in the bottom row and pushes the boundary one square up. We see that the boundary in (c) is the same with that in (a), except that the jaggedness in the middle is removed. Note that the four-square hole in the middle is closed in (c) by the green squares, which is why this combination is called a closing.

After an initial cut is returned, we smooth the boundary between the two parts using a closing operation. In our context, the structuring element is a virtual 1-ring circle and two

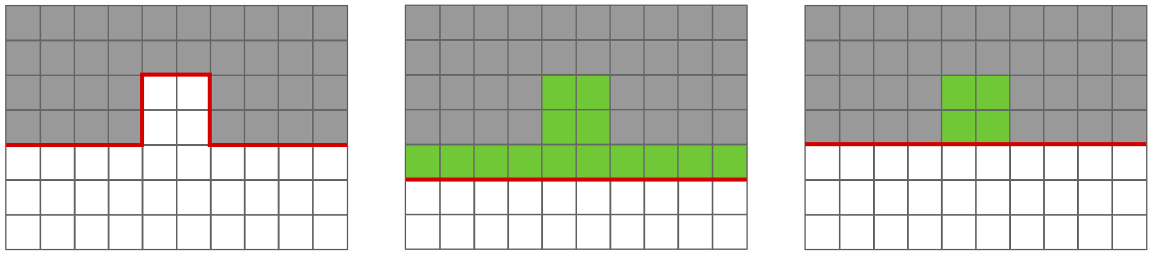
(a) original boundary (b) boundary after dilation (c) boundary after erosion

Figure 6.13: Fixing local artifacts of a boundary via dilation and erosion.

faces are considered neighbors if they share any vertex. Suppose that each face is labeled 1 or 2 to indicate its part membership. We first find the boundary faces within part 1, namely, faces with label 1 and adjacent to any face with label 2. Let us call these faces as part-1-boundary faces. For dilation, we temporarily mark faces from part 2 into part 1 if these faces (e.g., the green squares in Figure 6.13(b)) are neighbors of any part-1-boundary face. During erosion, we simply check these temporarily marked faces. For each of them, if it has any neighbor with label 2, it is eroded back into part 2; otherwise, it stays in part 1 (e.g., the four green squares in Figure 6.13(c)).

Note that smoothing results may be different depending on the working region of a closing operation. For Figure 6.13, we work on the gray region. It is easy to verify that if we work on the white region: first dilate from the white region into the gray region and then erode, the boundary would stay unchanged. Therefore, in practice we do a closing operation from either side separately, and choose the result that causes more membership swaps. This implies that the local artifacts along a boundary are better fixed. Also, we first smooth with larger structuring element (3-ring circle), and then smooth with smaller structuring element (1-ring circle). Through this, not only can relatively large local artifacts be fixed, but a boundary is also smoothed with fine granularity. We found that this produces better boundaries than using a single structuring element. Figure 6.14 shows how the morphology-based smoothing enhances the boundary between the wing and the body of the bird model (segmentation result for the entire model is shown in Figure 6.19(a)). We notice that several local jaggedness are eliminated. Since we do not allow boundaries to cross faces, a final boundary may not be completely smooth due to tessellation artifacts. This is a limitation of our smoothing scheme.

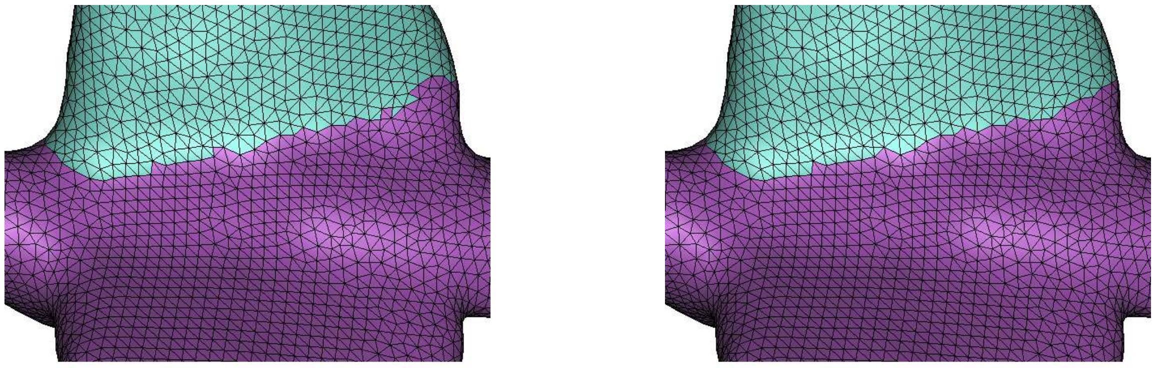

Figure 6.14: An example of boundary smoothing based on morphology.

6.5 Experimental Results

Complexity In each iteration, the complexity of the cut search is linear as the salience factors can be updated in constant time at each position. The morphological operation for boundary enhancement is also no more complex than linear. Therefore the complexity of the whole algorithm is dominated by the operations before a face sequence is computed. For obtaining L- or M-projections, we apply ACE [60], a multi-level method, to compute the second and third smallest eigenvectors of L and M. Since the asymptotic complexity of ACE is not reported by the authors, we denote it by $O(C_{ace})$. The complexities associated with contour extraction, pre-processing, and face sampling are all negligible. Computing a sequence ϱ in Equation 6.3 has a complexity of $O(n \log n)$. Supposing that the mesh is eventually segmented into k parts, $k-1$ iterations are needed and the entire complexity is roughly $O\big((k-1) \cdot C_{ace}\big) + O\big((k-1)n \log n\big)$. Empirically, ACE runs efficiently, especially for L-projections when only integers are involved in L.

Overview of experiments In this section, we first give a concrete example of our algorithm in iterations. After that, we present another two examples to show the merits of using L-projections or M-projections. Then we test our algorithm on a wide range of models followed by discussions about the limitations of our algorithm.

In the following experiments, we fix all the free parameters unless otherwise stated explicitly. We set $\eta = 0.1$ as the threshold value for segmentability tests and $w_{cvx} = 4$ for convexity measure C. The weights for the salience factors are: $w_s = 0.1$, $w_b = 0.3$, $w_p = 0.6$,

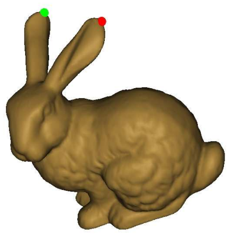
(a) 1 part

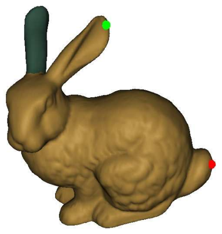
(b) 2 parts

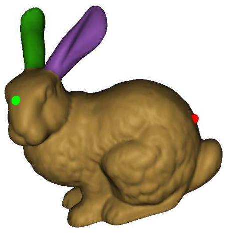
(c) 3 parts

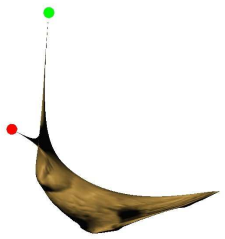
(a$'$) L, 0.45

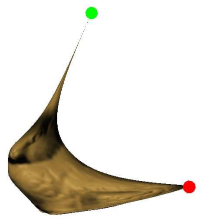
(b$'$) L, 0.35

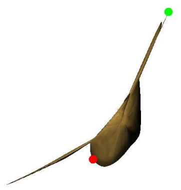
(c$'$) M, 0.24

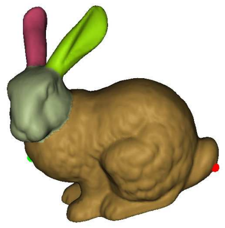
(d) 4 parts

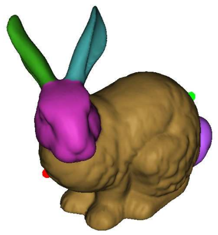
(e) 5 parts

(f) L, 0.006

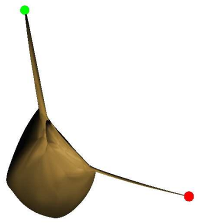
(d$'$) M, 0.28

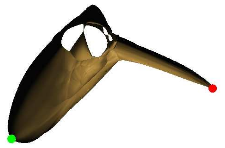
(e$'$) M, 0.21

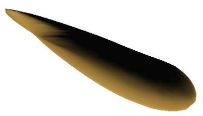
(g) M, 0.0008

Figure 6.15: Four iterations of salience-driven cut on the bunny model. The color dots represent the sample faces f_s and f_t, on the mesh piece to segment. Segmentation results are given in plots (a-e) and the corresponding projections are in plots (a$'$-e$'$). The projections are via either L or M, as indicated, along with the final segmentability score. Plots (f) and (g) show the projections of the left ear using L and M, both failing the segmentability test.

when an L-projection passes the segmentability test, or $w_s = 0.1$, $w_b = 0.6$, $w_p = 0.3$ when an M-projection passes the segmentability test.

Let's illustrate our algorithm at work in iterations for the bunny model in Figure 6.15. Plots (a-e) show the obtained parts in different colors. The brownish part in each plot is the current mesh piece ($\mathcal{M}_c$) to segment. Plots (a′-e′) show the 2D projections of the corresponding current mesh pieces, i.e., (a′) is the projection of the current mesh piece in (a). Plots (f) and (g) are the L- and M-projections of the bunny's left ear. As neither of them passes the segmentability test, the ear is not segmented. The final result is shown in Figure 6.19(d).

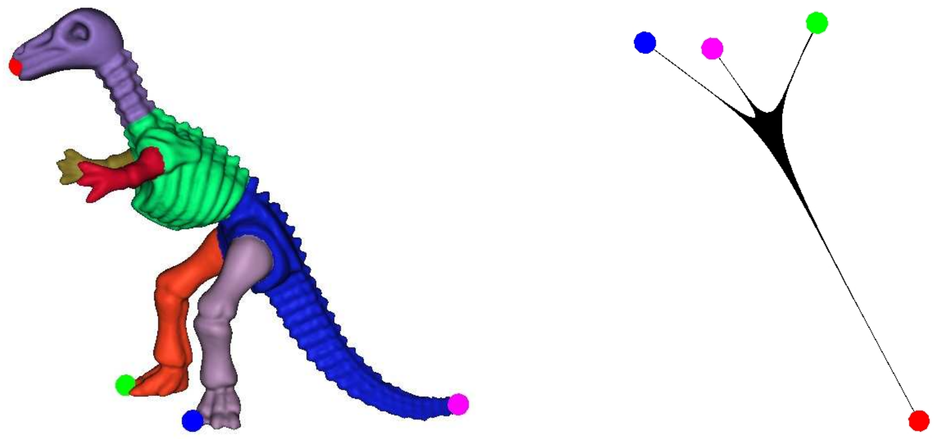

Figure 6.16: Low-frequency segmentation of the dinosaur model using L-projections. Shown on the right is the projection in the first iteration, where the color dots show the correspondence between 2D and 3D. Note that the upper limbs of the dinosaur are "absorbed" into the body in the first projection, but they will stand out in later iterations.

In certain cases, it is desirable to only focus on the "low-frequency" branching information reflected by L-projections, such as the one shown in Figure 6.16. It is counter-intuitive to segment the dinosaur model along all the concavities over its surface. If we only use L-projection for structure segmentability detection, the segmentation stops as shown in the figure. Note that in this test the protrusion and boundary strength salience factors, ω_p and ω_b, need to be tuned to obtain such a result. On the other hand, M-projections have their own merits too. Figure 6.17(a) shows the segmentation result using L-projection only. The brownish part fails the segmentability test since its projection, shown in plot (b), has a low

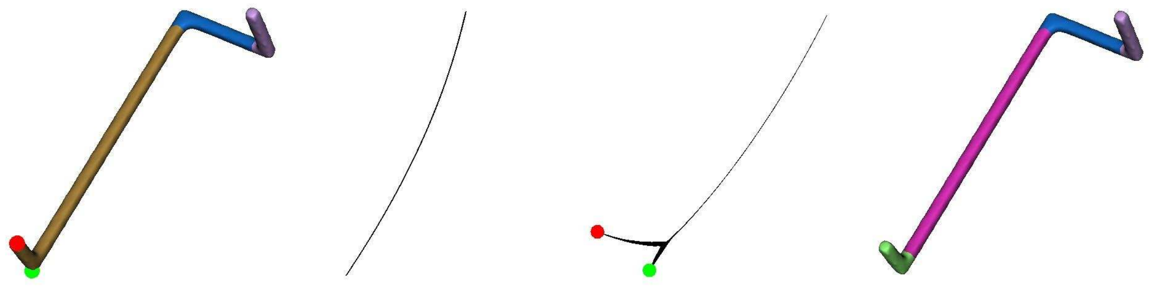

Figure 6.17: Segmentations of the snake model using L-projections and M-projections. The brownish part in (a) is not segmentable via the L-projection (b). When the M-projection (c) is considered, the part is further segmented, as shown in (d).

segmentability score. However, its M-projection enhances the bending and manifests itself with strong segmentability, resulting in a better segmentation shown in plot (d).

An interesting question one may ask is — can we set a salience threshold as a stopping criterion to substitute for segmentability? If so, we are able to remove the use of segmentability and only resort to salience for both stopping tests and locating meaningful cuts. In fact, we have tried this idea but the results were not robust because of the limitations of the current salience measure. Let's take the dinosaur model from Figure 6.16 as an example. Due to many concavities over the surface, salience scores measured for the face sequences are likely to be high (close to 1) and thus many spurious parts are to be produced if the stopping criterion is tested against a salience threshold. Segmentability is more suitable for this task as it better characterizes the two factors (see Section 6.2) that render a shape segmentable. Instead, the salience works better to rank the cuts based on their quality.

More segmentation results are available in Figure 6.18 and Figure 6.19. In Figure 6.18, models are segmented only through L-projections, where the goal is to show structure segmentability at work. Note that for the children model, the skirt in green would have been segmented by schemes relying on concavity, e.g., when our M-projection is considered; this is due to the presence of concavities, but it does not appeal to our intuition. With our algorithm, there is the option of focusing on structure segmentability only which may lead to a stopping configuration that better reflects shape semantics. Note also that the trident tines in the Neptune model are not considered segmentable as they are relatively short compared with the whole trident, thus not segmented out as a significant "low-frequency" structure. For the man model, however, the toes and fingers are all detected properly, as

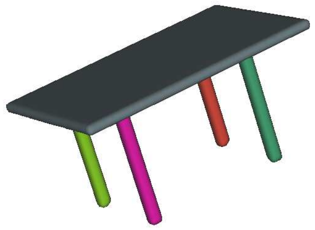
(a) table, 5 parts

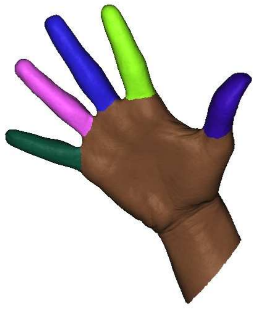
(b) hand, 6 parts

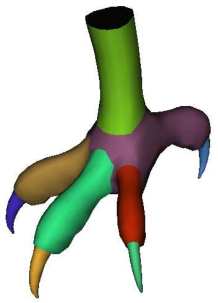
(c) claw, 9 parts

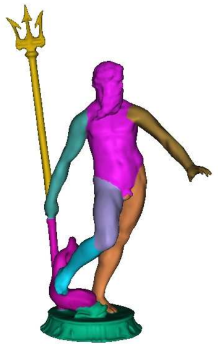
(d) Neptune, 9 parts

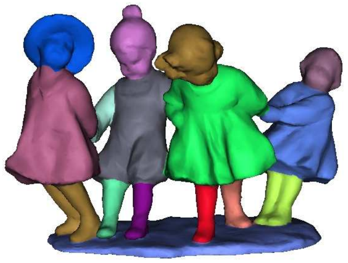
(e) children, 16 parts

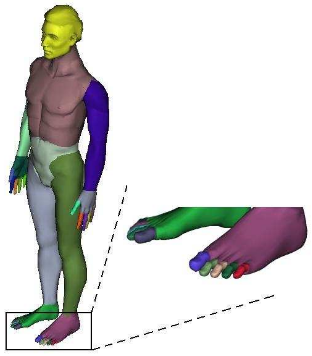
(f) man, 31 parts

Figure 6.18: Segmentation results using only L-projections.

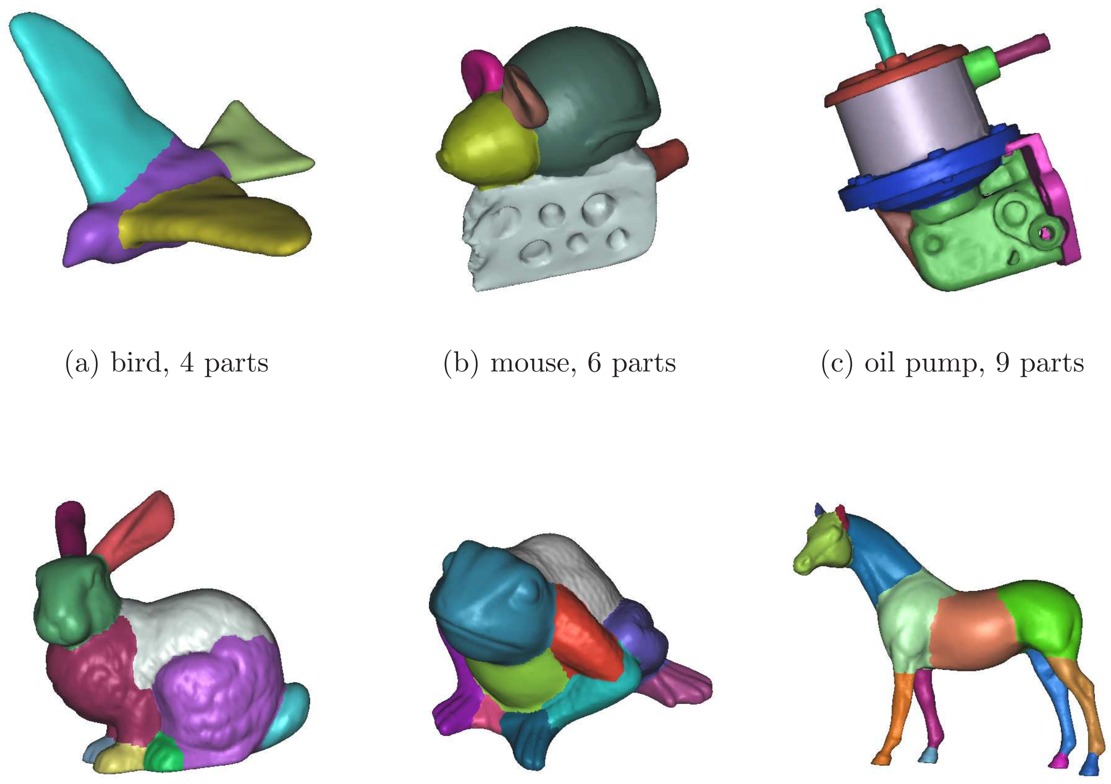

(a) bird, 4 parts (b) mouse, 6 parts (c) oil pump, 9 parts

(d) bunny, 13 parts (e) frog, 14 parts (f) horse, 14 parts

Figure 6.19: Segmentation results using both L-projections and M-projections.

they are relatively large in their own subparts. Compared with the result via the k-way spectral clustering shown in the lower plot of Figure 5.8(a) , the segmentation on the hand model in plot (b) has better boundaries between the fingers and the palm. This improvement is thanks to the merits of the salience-driven cut. But the palm is not segmented off the lower arm as the L-projection of the dark brown part does not pass the segmentability test.

Models in Figure 6.19 are segmented using both L-projections and M-projections. As a result, salient parts caused by concavities are also segmented out. As our algorithm is top-down, it is less likely to produce over-segmentation, which is typically caused by schemes based on local optimization, e.g., region growing. This can be understood from the torso of the bunny and the cheese part in the mouse model, where many local concavities exist. In practice, we have not observed that high genus would necessarily pose a problem for our algorithm. In Figure 6.18 and Figure 6.19, the Neptune, children, and oil pump models all have genus greater than 0 and our algorithm works robustly on them. Timing-wise, segmenting the frog model with about $100K$ faces into 14 parts takes 86 seconds, where 47 seconds are spent computing the eigenvectors using ACE for the projections.

Limitations A single segmentability threshold η may not always produce completely satisfactory results. For example, for the oil pump model in Figure 6.19(c), the big green part is not adequately segmented. Similarly, the eyes of the frog, in Figure 6.19(e), do not pass the segmentability test either. However, by fine tuning the segmentability threshold η, our algorithm is able to produce desirable segmentations. The test results on the frog model and a rabbit model are given in Figure 6.20. In the first column, the original results are shown. In the second column, we are able to achieve more meaningful results by relaxing η appropriately. To illustrate the robustness of our sampling algorithm, we show, in the third column, the working mesh pieces and the outer contours of their M-projections, respectively. The red and green dots mark the samples on the contours and their corresponding faces on the original mesh found by our sampling algorithm. We see that the samples are located from different parts of each working mesh piece. Although the use of segmentability scores has led to a better control than simply specifying a number of segments which is model-dependent, we realize that the current segmentability measure still requires further study for higher robustness.

The current salience measure also leaves room for improvement. The segmentation result on the Igea model in Figure 6.21 gives such an example. Due to the bumpy hair region,

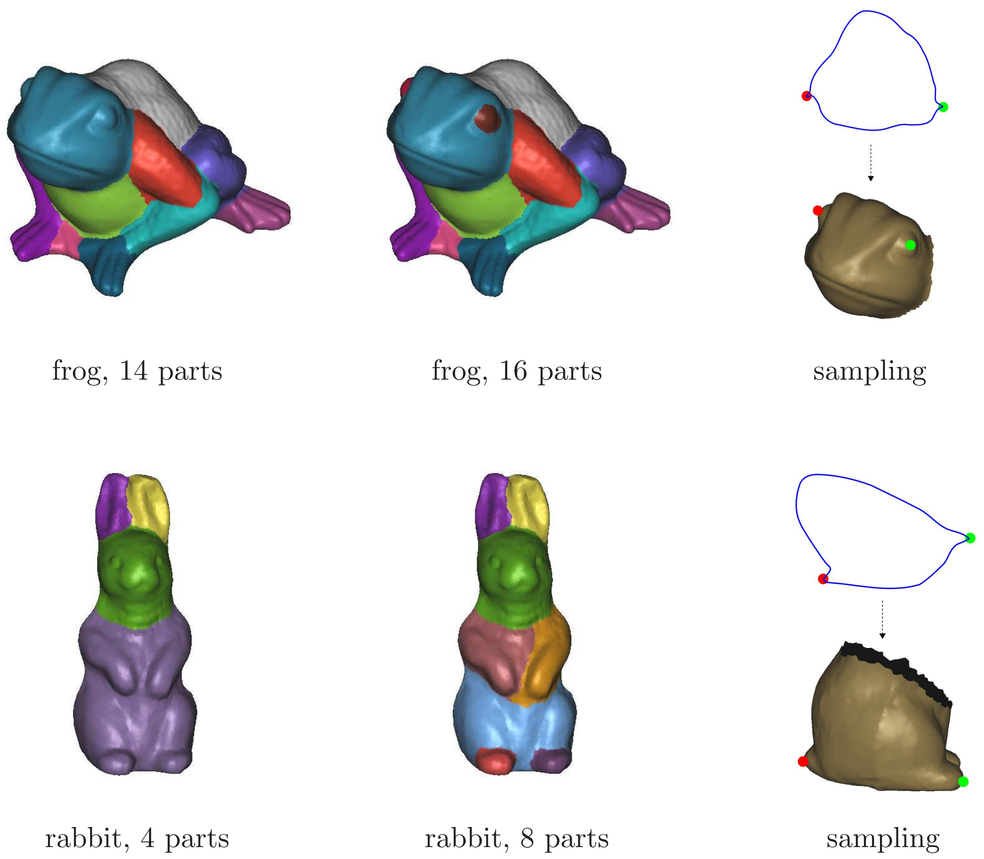

Figure 6.20: Segmentabilty threshold tuning could help produce more meaningful results. The first column shows the original segmentations with the default threshold; while the second column shows better results with relaxed threshold. In the last column, we show the working mesh pieces, their M-projections, and the two samples marked by the red and green dots.

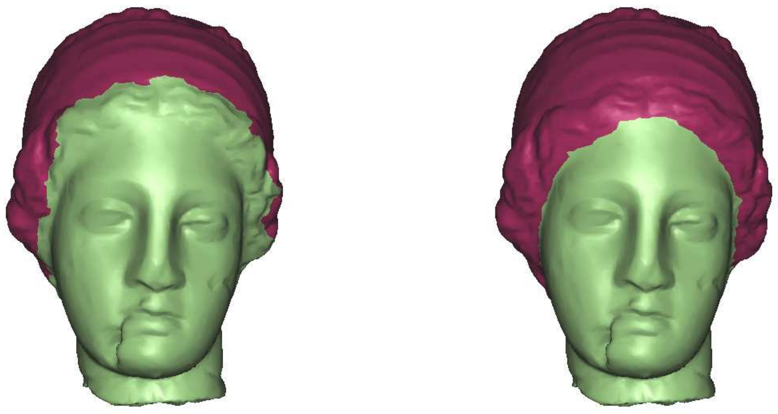

(a) automatic cut (b) best cut existent

Figure 6.21: The automatic cut and the best cut from the face sequence of Igea model.

our algorithm produces a sub-optimal result as shown in plot (a). However, a much better cut actually exists as shown in plot (b). This attests to the fact that the face sequence ϱ is effective in terms of preserving meaningful cuts; however, a fully robust algorithm able to automatically find the most meaningful cut is still to be worked on.

6.6 Summary

We improve upon our k-way spectral segmentation algorithm through recursive 2-way cuts, equipped with segmentability analysis and salience-driven cut search. Although there are a few free parameters to set, a set of fixed values have enabled us to produce meaningful parts for a variety of mesh models with different geometric properties. Our algorithm relies on spectral embeddings and it is driven by segmentability and salience.

Defining a robust stopping criterion for structural-level mesh segmentation is challenging, as it relates to quantifying how humans perceive parts and this is non-trivial. Our segmentability analysis copes with this difficulty, via measuring segmentability scores for outer contours of 2D spectral embeddings (projections). In such 2D embeddings, parts of 3D shapes are revealed and enhanced for easy investigation. Assisted with inner distance and Multi-Dimensional Scaling (also a spectral approach), our segmentability analysis achieves robust model-independent stopping criterion.

Once a mesh piece is considered segmentable by the segmentability analysis, it is divided into two parts using a salience-driven cut search. Our use of salience differs from previous algorithms in that we exploit salience actively by incorporating it into the search for parts. Previous algorithms are unable to do this because it is not clear how to make use of salience in the large search space for parts. We linearize the faces of a mesh piece in a sequence to reduce the search space significantly, while still manage to maintain the meaningful cuts in the sequence. This is made possible by a robust sampling scheme to find two faces from different parts of the given mesh piece and a linearization scheme with spectral properties. Our linearization scheme is theoretically sound and its realization turns out to be simple.

Driven by segmentability and salience, this improved algorithm produces robust and superior segmentation results.

Chapter 7

Conclusion

7.1 Summary

Mesh segmentation is an important research topic in geometry processing and analysis. It has seen a rapid increase in published works recently. This dissertation studies structural-level mesh segmentation via the spectral approach. Through the spectral approach, we model our problems globally using affinity matrices and their eigenvectors and eigenvalues are utilized to build optimal low-dimensional embeddings, in which our problem is solved efficiently and effectively. Our algorithms are automatic and work in a top-down manner. We recapitulate our works as follows.

As a crucial prerequisite for applying the spectral approach, we need to encode part information into an affinity matrix. To this end, we build a surface metric (Chapter 3) that is able to capture the part information of a shape. A part-aware metric is helpful since the segmentation quality benefits not only from a sound segmentation scheme, but also from an informative part characterization. The design of this metric is based on the observation that visible regions measured from within a shape change more rapidly across part boundaries. To the best of our knowledge, our metric is the first that can effectively capture part information. Besides, our part-aware metric, as a general tool, is demonstrated to be useful for a variety of other geometry processing applications, including sampling, registration, and retrieval.

With the part-aware metric that defines distances between mesh faces, we adapt spectral clustering to compute shape parts (Chapter 4). This algorithm is made effective by addressing several questions related to spectral embedding and K-means in our context.

Due to the algorithm's high computational complexity which restricts its use, we resort to sub-sampling (Chapter 5) based on the Nyström method. Through a geometric interpretation of the Nyström method, we propose a practical function to measure the sampling quality, which suggests a farthest-point sampling scheme to be employed in practice. Our sub-sampling approach substantially reduces the complexity of the spectral clustering algorithm without significantly sacrificing segmentation quality.

We further improve the autonomy and quality of our segmentation algorithm through a segmentability measure and a salience-driven cut search procedure (Chapter 6). We identify two factors that contribute to prominent parts of a shape, or in other words, make a shape segmentable. Since the two factors are difficult to measure on the original mesh, we propose spectral methods to transform the problem into the 2D domain, where the two factors are enhanced and readily measured. This leads to a segmentability score and we use a fixed threshold value against it to define a stopping criterion. Without letting users provide a different number of segments for each input model, this stopping criterion is model-independent and hence improves the autonomy of the algorithm. We also incorporate part salience into the search for parts to enhance segmentation quality. To this end, we arrange mesh faces into a sequence with spectral properties. Thanks to the substantially reduced search space for parts, we are able to realize a salience-driven segmentation through a line search, which would otherwise be too expensive to execute. Meanwhile, our sampling scheme ensures that the desirable cuts are well preserved in the sequence. This improved algorithm works via recursive 2-way cuts. Although this improved algorithm in general achieves higher autonomy and segmentation quality, the first one using K-means is more efficient as it obtains all the parts simultaneously. In addition, a user may sometimes want to have direct control over the number of segments, for example, when models need to be segmented into the same number of segments for correspondence analysis.

We believe that the effectiveness of a mesh segmentation algorithm can be attributed to two factors: robust measures for the characteristics of the desired segments and a well-designed procedure to compute such segments with the specified characteristics. In our case, we have a part-aware metric, as well as segmentability and salience to specify the characteristics of the parts we seek from different perspectives, and they are utilized effectively based on spectral techniques. When designing their own algorithms, readers could consider how to make their algorithms perform well on these two factors. As our algorithms are modular, a reader could reuse or improve upon some components of our algorithms. For example, a user can take our spectral embedding method using the part-aware metric, but make use of other clustering algorithms, e.g., the mean shift clustering [138], or adopt our line search procedure with their own part measures incorporated rather than the salience measure.

The segmentation algorithms developed in this thesis have been demonstrated to work effectively on a variety of models. When a mesh is noisy, our distance measures, especially the angular distance, may not reflect the part structures truthfully. In such cases, we can first apply a few iterations of Laplacian smoothing [123]. As our algorithms count on distances between faces measured across mesh surfaces via mesh dual graphs, inferior mesh connectivities could hinder the performance of our algorithms, especially around boundary regions. In addition, even if two parts are only connected by a few triangle, the distances between the faces from the two parts may be significantly reduced. Imagine two fingers from two arms touching each other. In this case, our algorithms may produce less than ideal segmentation results. We plan to look into this issue in the future. Other than this, we point out another three interesting future research directions in the following.

7.2 Future Directions

Enhanced Salience Measurement The robustness of the salience measure directly affects the segmentation quality of our recursive 2-way algorithm. In Figure 6.21, we have seen that there is still room to improve upon the current salience measure. We see two aspects for improvement. First, it is desirable to assess the three salience factors more accurately. It might not be the best to use surface area for the size salience factor and average edge concavity for the boundary strength salience factor. The protrusiveness ought to be further refined as well; currently only a rough estimation through the bounding volume is used. Note that an accurate salience estimation is challenging due to the efficiency constraint. When searching through the face sequence, salience measures have to be computed with sub-linear complexity; otherwise quadratic complexity would be incurred, which is not acceptable for large meshes.

Secondly, one can investigate how to utilize the three salience factors in a better way. Figure 6.12(a) gives an example cut search procedure for a particular mesh. We suspect that segmentation quality in general can benefit from enhancing the salience curves. For example, one may search through the face sequence in the first round simply for obtaining the three salience curves. The curves are then smoothed and fed to the second round for seeking the best cut. Such a strategy may help alleviate the influence of local inaccuracies. Besides, we currently use only two sets of weights for the salience factors, one for the L-projection and the other for the M-projection. It is worth studying the properties of the salience curves to help fine-tune their weights accordingly. For example, if one salience curve has a much larger variation than the other two, it may imply that the corresponding salience factor dominates the overall part salience. Therefore, a larger weight should be given to this salience factor. However, the implementation of such a strategy is likely to incur intensive user studies.

Supervised Segmentation The segmentation algorithms proposed in this thesis are unsupervised approaches: no prior information is used and the segmentation result is obtained based on the input mesh alone. Supervised segmentation has been considered for images [49, 52, 129] and it is natural to extend it to mesh segmentation.

In order to apply supervised segmentation, test models for an algorithm should bear similar geometric properties with the training models. For example, if an algorithm is trained to segment articulated shapes, such as human beings and animals, the algorithm should only be expected to work well on articulated shapes. A more interesting but challenging task is to train an algorithm to "understand" the meaning of a part so that it can work on generic shapes. Although it is not immediately clear to us how such a generic training can be realized systematically, there are two places in our recursive 2-way algorithm that may be investigated for such a generic training. One is for setting the weights for the salience factors, and the other is for the segmentability analysis based on the outer contours of mesh projections. For the salience weights, it is interesting to study how to build a correlation between the characteristics of the salience curves and their ideal weights. This may be achieved by training an algorithm with suitable salience curves and the ideal corresponding weights set by users. For the segmentability analysis, we can manually label a sufficient number of ground-truth contours as segmentable or not. By combining such labels with the characteristics of the contours, we may be able to predict whether a mesh piece is segmentable with higher accuracy.

Also, supervised techniques might help achieve the functional-level segmentation mentioned in Section 1.1.4. Recall that the resulting segments at the functional level reflect certain higher order information about the object represented by a mesh. This requires an algorithm to understand the functional properties of the object, which in general cannot be obtained only from the geometry of the input mesh. Therefore, a supervised algorithm becomes necessary.

Segmentation Benchmark An important missing piece for the current mesh segmentation research is a benchmark for evaluating segmentation results objectively. Currently, segmentation results, especially those at the structural level, are only judged subjectively. They are illustrated via color plots; it is the users' responsibility to judge the segmentation quality. A systematic and effective benchmark is hence called for.

Building such a benchmark involves a large amount of tedious manual segmentation work on many meshes. This also has to be done by a sufficient number of users to avoid biased input. Therefore, a handy interactive segmentation tool ought to be available to assist users navigating on mesh surfaces and making cuts easily. It would be desirable to have the tool automatically change the view point based on the current cut sketch and occlusion considerations. The tool should also be able to connect broken sketches to form continuous boundaries. Of course, functionalities including boundary smoothing and editing are useful as well.

In addition, how to appropriately measure the difference between ground-truth boundaries and those produced by algorithms is intricate. Simply counting how many vertices coincide is unlikely to work robustly, e.g., an algorithm may generate good segments but with all boundary vertices off the ground-truth by a small shift. Another complication emerges when hierarchy considerations come in, since it is meaningful to evaluate segmentation results in a hierarchical manner.

Appendix A

Face Sequence

As in Equation 5.1, we denote the affinity matrix $W = [A\ B; B^T\ C]$. Suppose the two sampled rows are

$$[A\ B] = \begin{bmatrix} 1 & \alpha & \dots & x_i & \dots \\ \alpha & 1 & \dots & y_i & \dots \end{bmatrix}, \tag{A.1}$$

with $A = [1\ \alpha; \alpha\ 1]$ and α being the affinity between the two sample faces. Note that as the samples occupy the first two indices, i is in range $[3, n]$. With only $[A\ B]$, the two approximated eigenvectors of W via the Nyström method are given in Equation 6.5. In Equation 6.8, the normalized affinity matrix N is defined when entire W is known. The question is how to apply the Nyström method to compute the approximate eigenvectors of N when only the entries in $[A\ B]$ are available.

We can similarly write $N = [A'\ B'; B'^T\ C']$ and the entries of the first two rows are

$$[A'\ B'] = \begin{bmatrix} \frac{1}{s_1} & \frac{\alpha}{\sqrt{s_1 s_2}} & \dots & \frac{x_i}{\sqrt{s_1 s_i}} & \dots \\ \frac{\alpha}{\sqrt{s_2 s_1}} & \frac{1}{s_2} & \dots & \frac{y_i}{\sqrt{s_2 s_i}} & \dots \end{bmatrix}, \tag{A.2}$$

where s_i is the sum of the i-th row of W. Let $A' = E'\Delta' E'^T$ be the eigenvalue decomposition, it is derived that

$$\Delta' = \begin{bmatrix} \lambda_1 & 0 \\ 0 & \lambda_2 \end{bmatrix} = \begin{bmatrix} \frac{(Q+J)}{2s_1 s_2} & 0 \\ 0 & \frac{(Q-J)}{2s_1 s_2} \end{bmatrix}, \tag{A.3}$$

and

$$E' = \begin{bmatrix} e_{11} & e_{12} \\ e_{21} & e_{22} \end{bmatrix} = \begin{bmatrix} \frac{P+J}{2\alpha\sqrt{s_1 s_2}} & \frac{P-J}{2\alpha\sqrt{s_1 s_2}} \\ 1 & 1 \end{bmatrix}, \tag{A.4}$$

where $P = s_2 - s_1$, $Q = s_2 + s_1$, and $J = \sqrt{(s_2 - s_1)^2 + 4\alpha^2 s_1 s_2}$. Based on the approximation formula in Equation 5.2, the approximated eigenvectors of N are

$$\tilde{E}' = \begin{bmatrix} E' \\ B'^T E' \Delta'^{-1} \end{bmatrix} = \begin{bmatrix} \frac{P+J}{2\alpha\sqrt{s_1 s_2}} & \frac{P-J}{2\alpha\sqrt{s_1 s_2}} \\ 1 & 1 \\ \cdots & \cdots \\ \frac{1}{\lambda_1 \sqrt{s_i}}\left(\frac{x_i e_{11}}{\sqrt{s_1}} + \frac{y_i e_{21}}{\sqrt{s_2}}\right) & \frac{1}{\lambda_2 \sqrt{s_i}}\left(\frac{x_i e_{12}}{\sqrt{s_1}} + \frac{y_i e_{22}}{\sqrt{s_2}}\right) \\ \cdots & \cdots \end{bmatrix}. \tag{A.5}$$

Then the component-wise ratio of the second eigenvector to the first eigenvector is

$$\hat{\mathbf{e}} = \left[\frac{P-J}{P+J},\ 1,\ \ldots,\ \frac{\lambda_1}{\lambda_2} \cdot \left(\frac{\sqrt{s_2} x_i e_{12} + \sqrt{s_1} y_i e_{22}}{\sqrt{s_2} x_i e_{11} + \sqrt{s_1} y_i e_{21}}\right) \ldots\right]. \tag{A.6}$$

Note that the unknown value s_i is canceled out.

In Section 6.3.1, we have shown that the face sequences obtained by sorting $\tilde{\mathbf{e}}$ (Equation 6.3) and $\mathbf{e}$ (Equation 6.6) are the same. In the following, we prove that the sequences obtained by sorting $\tilde{\mathbf{e}}$ and $\hat{\mathbf{e}}$ are also the same in a similar way.

Proposition A.1. $\forall f_i, \hat{\mathbf{e}}(f_s) \leq \hat{\mathbf{e}}(f_i) \leq \hat{\mathbf{e}}(f_t)$. *This means that the embeddings of the two sample faces f_s and f_t are at the two ends of $\hat{\mathbf{e}}$.*

Proof. Assume $\hat{\mathbf{e}}(f_i) = \frac{P-J}{P+J}$ and $\hat{\mathbf{e}}(f_t) = 1$. We only prove $\hat{\mathbf{e}}(f_s) \leq \hat{\mathbf{e}}(f_i)$. $\hat{\mathbf{e}}(f_i) \leq \hat{\mathbf{e}}(f_t)$ can be proved similarly.

$$\begin{aligned}
\hat{\mathbf{e}}(f_s) \leq \hat{\mathbf{e}}(f_i) &\Leftrightarrow \frac{P-J}{P+J} \leq \frac{\lambda_1}{\lambda_2} \cdot \left(\frac{\sqrt{s_2} x_i e_{12} + \sqrt{s_1} y_i e_{22}}{\sqrt{s_2} x_i e_{11} + \sqrt{s_1} y_i e_{21}}\right) \\
&\Leftrightarrow \frac{P-J}{P+J} \leq \frac{Q+J}{Q-J} \cdot \frac{(P-J)x_i + 2\alpha s_1 y_i}{(P+J)x_i + 2\alpha s_1 y_i} \\
&\Leftrightarrow \ldots \\
&\Leftrightarrow (PQ + J^2)x_i \leq (P+Q)(Px_i + 2\alpha s_1 y_i) \\
&\Leftrightarrow \ldots \\
&\Leftrightarrow \alpha \leq \frac{y_i}{x_i} \\
&\Leftrightarrow e^{-d_{st}/2\sigma^2} \leq e^{(d_{is} - d_{it})/2\sigma^2} \\
&\Leftrightarrow -d_{st} \leq d_{is} - d_{it} \\
&\Leftrightarrow d_{it} \leq d_{is} + d_{st}.
\end{aligned}$$

Recall that $\alpha = e^{-d_{st}/2\sigma^2}$, $x_i = e^{-d_{is}/2\sigma^2}$, and $y_i = e^{-d_{it}/2\sigma^2}$, where d denotes the graph distance between two faces. Since the graph distance is a metric, satisfying the triangle inequality, the last inequality holds. This concludes our proof. $\square$

Proposition A.2. *Sorting vectors* $\tilde{\mathbf{e}}$ *or* $\hat{\mathbf{e}}$ *produces the same face sequence.*

Proof. For $\hat{\mathbf{e}}$, we denote $F'(f_i) = \frac{\lambda_1}{\lambda_2} \cdot \left(\frac{\sqrt{s_2}x_i e_{12} + \sqrt{s_1}y_i e_{22}}{\sqrt{s_2}x_i e_{11} + \sqrt{s_1}y_i e_{21}} \right)$. Representing $\beta = x_i/y_i$, we can also write $F'(\beta) = \frac{Q+J}{Q-J}\left(1 - \frac{2J}{(P+J)+2s_1\alpha/\beta}\right)$; note that Q, J, P, s_1, and α are all independent of β. Clearly $F'(\beta)$ is monotone and inversely proportional to β. Meanwhile, as $\beta = e^{-d_{is}/2\sigma^2}/e^{-d_{it}/2\sigma^2} = e^{-(d_{is}-d_{it})/2\sigma^2}$, β is monotone and inversely (exponentially) proportional to $(d_{is} - d_{it})$. Therefore F' is monotone and (exponentially) proportional to $(d_{is} - d_{it})$. Except for the two sample faces, this ensures that the face sequences obtained by sorting $\tilde{\mathbf{e}}$ and $\hat{\mathbf{e}}$ are the same. With the same argument used in Proposition 6.2, the two sample faces are sitting at the two ends of $\tilde{\mathbf{e}}$. Plus Proposition A.1, we prove that the two sequences are the same. $\square$

With these being said, the face sequences produced by sorting $\tilde{\mathbf{e}}$, $\mathbf{e}$, or $\hat{\mathbf{e}}$ are all the same.

Bibliography

[1] A.I.M.A.T.S.H.A.P.E. - Advanced and Innovative Models And Tools for the development of Semantic-based systems for Handling, Acquiring, and Processing knowledge Embedded in multidimensional digital objects. http://www.aimatshape.net/.

[2] K. Abe, C. Arcelli, T. Hisajama, and T. Ibaraki. Parts of planar shapes. *Pattern Recognition*, 29(90):1703–1711, 1996.

[3] J. Ahmed, J. Bosworth, and S. T. Acton. Image segmentation techniques for object-based coding. In *Proc. Image Analysis and Interpretation*, pages 41–45, 2000.

[4] M. Attene, B. Falcidieno, and M. Spagnuolo. Hierarchical segmentation based on fitting primitives. *The Visual Computer*, pages 181–193, 2006.

[5] M. Attene, S. Katz, M. Mortara, G. Patane, M. Spagnuolo, and A. Tal. Mesh segmentation - a comparative study. In *Proc. IEEE International Conference on Shape Modeling and Applications*, pages 14–25, 2006.

[6] M. Attene, M. Mortara, M. Spagnuolo, and B. Falcidieno. Hierarchical convex approximation of 3D shapes for fast region selection. *Computer Graphics Forum (Proc. Eurographics Symposium on Geometry Processing)*, 27(5):1323–1333, 2008.

[7] O. K.-C. Au, C.-L. Tai, H.-K. Chu, D. Cohen-Or, and T.-Y. Lee. Skeleton extraction by mesh contraction. *ACM Transactions on Graphics*, 27(3):1–10, 2008.

[8] S. P. Awate, T. Tasdizen, and R. T. Whitaker. Unsupervised texture segmentation with nonparametric neighborhood statistics. In *Proc. European Conference on Computer Vision*, pages 494–507, 2006.

[9] F. Bach and M. Jordan. Learning spectral clustering. Technical Report UCB/CSD-03-1249, University of California Berkeley, June 2003.

[10] C. T. H. Baker. *The Numerical Treatment of Integral Equations.* Oxford: Clarendon Press, 1977.

[11] M. Belkin and P. Niyogi. Laplacian eigenmaps for dimensionality reduction and data representation. *Neural Computation*, 15(6):1373–1396, 2003.

[12] S. Belongie, C. Fowlkes, F. Chung, and J. Malik. Spectral partitioning with indefinite kernels using the nystrm extension. In *Proc. European Conference on Computer Vision*, pages 531–542, 2002.

[13] Y. Bengio, O. Delalleau, N. L. Roux, J.-F. Paiement, P. Vincent, and M. Ouimet. Learning eigenfunctions links spectral embedding and kernel pca. *Neural Computation*, 16(10):2197–2219, 2004.

[14] P. J. Besl and N. D. McKay. A method for registration of 3D shapes. *IEEE Transactions on Pattern Analysis and Machine Intelligence*, 14(2):239–256, 1992.

[15] I. Biederman. Recognition-by components: a theory of human image understanding. *Psychological Review*, 94:115–147, 1987.

[16] S. Bouix, P. Dimitrov, and K. Siddiqi. Physics-based skeletons. In *Proc. Vision Interface*, pages 23–30, 2000.

[17] Y. Boykov, O. Veksler, and R. Zabih. Fast approximate energy minimization via graph cuts. *IEEE Transactions on Pattern Analysis and Machine Intelligence*, 23(11):1222–1239, 2001.

[18] M. Brand and K. Huang. A unifying theorem for spectral embedding and clustering. In *Proc. 9th International Workshop on Artificial Intelligence and Statistics*, 2003.

[19] C. J. C. Burges. A tutorial on support vector machines for pattern recognition. *Data Mining and Knowledge Discovery*, 2(2):121–167, 1998.

[20] J. Canny. A computational approach to edge detection. *IEEE Transactions on Pattern Analysis and Machine Intelligence*, 8:679–698, 1986.

[21] M. Carcassoni and E. R. Hancock. Spectral correspondence for point pattern matching. *Pattern Recognition*, 36:193–204, 2003.

[22] B. Chazelle. Triangulating a simple polygon in linear time. *Discrete Computational Geometry*, 6:485–524, 1991.

[23] B. Chazelle, D. Dobkin, N. Shourhura, and A. Tal. Strategies for polyhedral surface decomposition: An experimental study. *Computational Geometry: Theory and Applications*, 7(4-5):327–342, 1997.

[24] F. R. K. Chung. *Spectral Graph Theory (CBMS Regional Conference Series in Mathematics, No. 92).* American Mathematical Society, 1997.

[25] D. Cohen-Steiner, P. Alliez, and M. Desbrun. Variational shape approximation. *ACM Transactions on Graphics*, 23(3):905–914, 2004.

[26] D. Cohen-Steiner and J.-M. Morvan. Restricted delaunay triangulations and normal cycle. In *Proc. 19th annual Symposium on Computational Geometry*, pages 312–321, 2003.

[27] M. Cox and T. Cox. *Multidimensional Scaling.* Chapman and Hall, 1994.

[28] T. Culver, J. Keyser, and D. Manocha. Accurate computation of the medial axis of a polyhedron. In *Proc. 5th ACM symposium on Solid modeling and applications*, pages 179–190, 1999.

[29] E. de Aguiar, C. Theobalt, S. Thrun, and H.-P. Seidel. Automatic Conversion of Mesh Animations into Skeleton-based Animations. *Computer Graphics Forum (Proc. Eurographics)*, 27(2):389–397, 4 2008.

[30] F. de Goes, S. Goldenstein, and L. Velho. A hierarchical segmentation of articulated bodies. *Computer Graphics Forum (Proc. Symposium on Geometry Processing)*, 27(5):1349–1356, 2008.

[31] T. K. Dey, J. Giesen, and S. Goswami. Shape segmentation and matching with flow discretization. In *Proc. Workshop Algorithms Data Structures*, pages 25–36, 2003.

[32] T. K. Dey and W. Zhao. Approximate medial axis as a voronoi subcomplex. In *Proc. ACM symposium on Solid modeling and applications*, pages 356–366, 2002.

[33] A. Elad and R. Kimmel. On bending invariant signatures for surfaces. *IEEE Transactions on Pattern Analysis and Machine Intelligence*, 25(10):1285–1295, 2003.

[34] Y. Eldar, M. Lindenbaum, M. Porat, and Y. Y. Zeevi. The farthest point strategy for progressive image sampling. *IEEE Transactions on Image Processing*, 6(9):1305–1315, 1997.

[35] M. Fiedler. Algebraic connectivity of graphs. *Czech Mathematical Journal*, 23:298–305, 1973.

[36] M. Filippone, F. Camastra, F. Masulli, and S. Rovetta. A survey of kernel and spectral methods for clustering. *Pattern Recognition*, 41(1):176–190, 2008.

[37] I. Fischer and J. Poland. New methods for spectral clustering. Technical Report IDSIA-12-04, Dalle Molle Institute for Artificial Intelligence, Jun. 2004.

[38] C. Fowlkes, S. Belongie, F. Chung, and J. Malik. Spectral grouping using the Nyström method. *IEEE Transactions on Pattern Analysis and Machine Intelligence*, 26:214–225, 2004.

[39] T. Funkhouser, M. Kazhdan, P. Shilane, P. Min, W. Kiefer, A. Tal, S. Rusinkiewicz, and D. Dobkin. Modeling by example. *ACM Transactions on Graphics*, 23(3):652–663, 2004.

[40] M. Garland, A. Willmott, and P. Heckbert. Hierarchical face clustering on polygonal surfaces. In *Proc. ACM Symposium on Interactive 3D Graphics*, pages 49–58, 2001.

[41] N. Gelfand and L. Guibas. Shape segmentation using local slippage analysis. In *Proc. Eurographics Symposium on Geometry Processing*, pages 214–223, 2004.

[42] A. Golovinskiy and T. Funkhouser. Randomized cuts for 3D mesh analysis. *ACM Transactions on Graphics (Proc. SIGGRAPH ASIA)*, 27(5):1–12, 2008.

[43] S. Goswami, T. K. Dey, and C. L. Bajaj. Identifying flat and tubular regions of a shape by unstable manifolds. In *Proc. ACM Symposium on Solid and Physical Modeling*, pages 27–37, 2006.

[44] L. Grady. Random walks for image segmentation. *IEEE Transactions on Pattern Analysis and Machine Intelligence*, 28(11):1768–1783, 2006.

[45] W. Guan, J. Cai, J. Zheng, and C. W. Chen. Segmentation based view-dependent 3D graphics model transmission. *IEEE Transactions on Multimedia*, 10(5):724–734, 2008.

[46] G. Hamarneh, R. Abugharbieh, and T. McInerney. Medial profiles for modeling deformation and statistical analysis of shape and their use in medical image segmentation. *International Journal of Shape Modeling*, 10(2):187–209, 2004.

[47] R. M. Haralick and L. G. Shapiro. Image segmentation techniques. *Computer Vision, Graphics, Image Processing*, 29:100–132, 1985.

[48] R. M. Haralick, S. Sternberg, and X. Zhuang. Image analysis using mathematical morphology. *IEEE Transactions on Pattern Analysis and Machine Intelligence*, 9(4):532–550, 1987.

[49] X. He, R. S. Zemel, and M. A. Carreira-Perpinan. Multiscale conditional random fields for image labeling. In *Proc. IEEE Conference on Computer Vision and Pattern Recognition*, pages 695–702, 2004.

[50] D. D. Hoffman and W. A. Richards. Parts of recognition. *Cognition*, 18:65–96, 1984.

[51] D. D. Hoffman and M. Singh. Salience of visual parts. *Cognition*, 63:29–78, 1997.

[52] D. Hoiem, A. A. Efros, and M. Hebert. Recovering surface layout from an image. *International Journal of Computer Vision*, 75(1), 2007.

[53] V. Jain, H. Zhang, and O. van Kaick. Non-rigid spectral correspondence of triangle meshes. *International Journal on Shape Modeling*, 13(1):101–124, 2007.

[54] A. Jaklic, A. Leonardis, and F. Solina. *Segmentation and recovery of superquadrics.* Kluwer Academic Publishers, 2000.

[55] Z. Ji, L. Liu, Z. Chen, and G. Wang. Easy mesh cutting. In *Proc. Eurographics*, volume 25, pages 283–291, 2006.

[56] D. Julius, V. Kraevoy, and A. Sheffer. D-charts: Quasi-developable mesh segmentation. In *Computer Graphics Forum (Proc. Eurographics)*, volume 24, pages 581–590, 2005.

[57] F. Kanehara, S. Satoh, and T. Hamada. Shape decomposition based on erosion model. In *Proc. Physics-Based Modeling in Computer Vision*, pages 128–134, 1995.

[58] Z. Karni and C. Gotsman. Spectral compression of mesh geometry. In *Proc. SIGGRAPH*, pages 279–286, 2000.

[59] S. Katz and A. Tal. Hierarchical mesh decomposition using fuzzy clustering and cuts. *ACM Transactions on Graphics*, 22(3):954–961, 2003.

[60] Y. Koren. On spectral graph drawing. In *Proc. International Computing and Combinatorics Conference*, 2003.

[61] V. Kraevoy, D. Julius, and A. Sheffer. Shuffler: Modeling with interchangeable parts. In *Proc. Pacific Grahpics*, 2007.

[62] S. Kumar, S. H. Ong, S. Ranganath, T. C. Ong, and F. T. Chew. A rule-based approach for robust clump splitting. *Pattern Recognition*, 39(6):1088–1098, 2006.

[63] J. O. Lachaud and A. Montanvert. Deformable meshes with automated topology changes for coarse-to-fine three-dimensional surface extraction. *Journal of Medical Image Analysis*, 3(1):1–21, 1999.

[64] Y.-K. Lai, S.-M. Hu, R. R. Martin, and P. L. Rosin. Fast mesh segmentation using random walks. In *Proc. ACM Symposium on Solid and Physical Modeling*, pages 183–191, 2008.

[65] Y. K. Lai, Q. Y. Zhou, S. M. Hu, and R. R. Martin. Feature sensitive mesh segmentation. In *Proc. ACM Symposium on Solid and Physical Modeling*, pages 17–26, 2006.

[66] Y.-K. Lai, Q.-Y. Zhou, S.-M. Hu, J. Wallner, and H. Pottmann. Robust feature classification and editing. *IEEE Transactions on Visualization and Computer Graphics*, 13(1):34–45, 2007.

[67] L. J. Latecki and R. Lakämper. Convexity rule for shape decomposition based on discrete contour evolution. *Computer Vision and Image Understanding*, 73(3):441–454, 1999.

[68] G. Lavoué, F. Dupont, and A. Baskurt. A new CAD mesh segmentation method, based on curvature tensor analysis. *Computer-Aided Design*, 37(10):975–987, 2005.

[69] Y. Lee, S. Lee, A. Shamir, D. Cohen-Or, and H.-P. Seidel. Mesh scissoring with minimal rule and part salience. *Computer Aided Geometric Design*, 22:444–465, 2005.

[70] R. B. Lehoucq, D. C. Sorensen, and P. Vu. ARPACK: An implementation of the implicitly re-started Arnoldi iteration that computes some of the eigenvalues and eigenvectors of a large sparse matrix. http://www.caam.rice.edu/software/arpack/.

[71] J. E. Lengyel. Compression of time-dependent geometry. In *Proc. the 1999 symposium on Interactive 3D graphics*, pages 89–95, 1999.

[72] B. Lévy, S. Petitjean, N. Ray, and J. Maillot. Least squares conformal maps for automatic texture atlas generation. *ACM Transactions on Graphics*, 21(3):362–371, 2002.

[73] M. Leyton. *A Generative Theory of Shape (Lecture Notes in Computer Science, 2145)*. Springer, November 2001.

[74] X. Li, T. Toon, T. Tan, and Z. Huang. Decomposing polygon meshes for interactive applications. In *Proc. Symposium on Interactive 3D Graphics*, pages 35–42, 2001.

[75] J. Lien and N. Amato. Simultaneous shape decomposition and skeletonization using approximate convex decomposition. Technical Report TR05-015, Texas A&M University, Dec. 2005.

[76] J.-M. Lien and N. M. Amato. Approximate convex decomposition of polyhedra. In *Proc. ACM Symposium on Solid and Physical Modeling*, pages 121–131, 2007.

[77] H. Ling and D. W. Jacobs. Using the inner-distance for classification of articulated shapes. In *Proc. Computer Vision and Pattern Recognition*, volume 2, pages 719–726, 2005.

[78] S. Lloyd. Least square quantization in PCM. *IEEE Transaction on Information Theory*, 28(2):129–137, 1982.

[79] L. Lu, Y.-K. Choi, W. Wang, and M.-S. Kim. Variational 3D shape segmentation for bounding volume computation. *Computer Graphics Forum (Proc. Eurographics)*, 26:329–338, 2007.

[80] J. B. MacQueen. Some methods for classification and analysis of multivariate observations. In *Proc. 5-th Berkeley Symposium on Mathematical Statistics and Probability*, pages 281–297. University of California Press, 1967.

[81] M. Mahmoudi and G. Sapiro. Three-dimensional point cloud recognition via distributions of geometric distances. In *Proc. IEEE Conference on Computer Vision and Pattern Recognition*, pages 1–8, 2008.

[82] A. P. Mangan and R. T. Whitaker. Partitioning 3D surface meshes using watershed segmentation. *IEEE Transactions on Visualization and Computer Graphics*, 5(4):308–321, 1999.

[83] L. Manor and P. Perona. Self-tuning spectral clustering. In *Proc. Advances in Neural Information Processing Systems*, pages 1601–1608, 2004.

[84] D. R. Martin, C. C. Fowlkes, and J. Malik. Learning to detect natural image boundaries using local brightness, color, and texture cues. *IEEE Transactions on Pattern Analysis and Machine Intelligence*, 26(5):530–549, 2004.

[85] B. Micusik and A. Hanbury. Template patch driven image segmentation. In *Proc. British Machine Vision Conference*, pages II:819–829, 2006.

[86] J. V. Miller, D. E. Breen, W. E. Lorensen, R. M. O'Bara, and M. J. Wozny. Geometrically deformed models: a method for extracting closed geometric models form volume data. In *Proc. SIGGRAPH*, pages 217–226, New York, NY, USA, 1991. ACM.

[87] N. J. Mitra, L. Guibas, and M. Pauly. Partial and approximate symmetry detection for 3D geometry. *ACM Transactions on Graphics*, 25(3):560–568, 2006.

[88] P. Moore and C. Fitz. Gestalt theory and instructional design. *Journal of Technical Writing and Communication*, 23(2):137–157, 1993.

[89] M. Mortara, G. Patane, M. Spagnuolo, B. Falcidieno, and J. Rossignac. Plumber: a multi-scale decomposition of 3D shapes into tubular primitives and bodies. In *Proc. ninth ACM Symposium on Solid Modeling and Applications*, pages 139–158, 2004.

[90] A. Y. Ng, M. I. Jordan, and Y. Weiss. On spectral clustering: analysis and an algorithm. In *Proc. Advances in Neural Information Processing Systems*, pages 857–864, 2002.

[91] R. Osada, T. Funkhouser, B. Chazelle, and D. Dobkin. Shape distributions. *ACM Transactions on Graphics*, 21(4):807–832, 2002.

[92] D. Page, A. Koschan, and M. Abidi. Linking feature lines on 3D triangle meshes with artificial potential fields. In *Proc. IEEE 3rd International Symposium on 3D Data Processing, Visualization and Transmission*, pages 358–364, 2006.

[93] D. L. Page. *Part decomposition of 3D surfaces.* PhD thesis, University of Tennessee, Knoxville, 2003. Major Professor-Mongi A. Abidi.

[94] D. L. Page, A. F. Koschan, and M. A. Abidi. Perception-based 3D triangle mesh segmentation using fast marching watershed. In *Proc. IEEE Conference on Computer Vision and Pattern Recognition*, pages 27–32, 2003.

[95] N. R. Pal and S. K. Pal. A review on image segmentation techniques. *Pattern Recognition*, 26:1277–1294, 1993.

[96] N. Paragios and R. Deriche. Geodesic active regions and level set methods for supervised texture segmentation. *International Journal of Computer Vision*, 46(3):223–247, 2002.

[97] P. Perona and W. Freeman. A factorization approach to grouping. In *Proc. European Conference on Computer Vision*, pages 655–670, 1998.

[98] G. Peyre and L. Cohen. Surface segmentation using geodesic centroidal tesselation. In *Proc. 3D Data Processing, Visualization, and Transmission, 2nd International Symposium*, pages 995–1002, 2004.

[99] D. L. Pham, C. Xu, and J. L. Prince. Current methods in medical image segmentation. *Annual Review of Biomedical Engineering*, 2:315–337, 2000.

[100] J. Podolak, P. Shilane, A. Golovinskiy, S. Rusinkiewicz, and T. Funkhouser. A planar-reflective symmetry transform for 3D shapes. *ACM Transactions on Graphics*, 25(3):549–559, 2006.

[101] E. Praun, W. Sweldens, and P. Schröder. Consistent mesh parameterizations. In *Proc. SIGGRAPH*, pages 179–184, 2001.

[102] A. Razdan and M. Bae. A hybrid approach to feature segmentation of 3-dimensional meshes. *Computer-Aided Design*, 35(9):783–789, 2002.

[103] X. Ren and J. Malik. A probabilistic multi-scale model for contour completion based on image statistics. In *Proc. European Conference on Computer Vision*, pages 312–327. Springer-Verlag, 2002.

[104] D. Reniers and A. Telea. Skeleton-based hierarchical shape segmentation. In *Proc. IEEE International Conference on Shape Modeling and Applications*, pages 179–188, 2007.

[105] E. Rosin. Shape partitioning by convexity. *IEEE Transactions on Systems, Man and Cybernetics*, 30:202–210, 2000.

[106] S. T. Roweis and L. K. Saul. Nonlinear dimensionality reduction by locally linear embedding. *Science*, 290(5500):2323–2326, December 2000.

[107] P. Sander, J. Snyder, S. Gortler, and H. Hoppe. Texture mapping progressive meshes. In *Proc. SIGGRAPH*, pages 409–416, 2001.

[108] P. V. Sander, Z. J. Wood, S. J. Gortler, J. Snyder, and H. Hoppe. Multi-chart geometry images. In *Proc. Eurographics Symposium on Geometry Processing*, pages 146–155, 2003.

[109] B. Schölkopf, A. Smola, and K.-R. Müller. Nonlinear component analysis as a kernel eigenvalue problem. *Neural Computation*, 10(5):1299–1319, 1998.

[110] S. Shalom, L. Shapira, A. Shamir, and D. Cohen-Or. Part analogies in sets of objects. In *Proc. Eurographics Symposium on 3D Object Retrieval*, pages 33–40, 2008.

[111] A. Shamir. Segmentation and shape extraction of 3D boundary meshes. In *State-of-the-Art Report, Proc. Eurographics*, pages 137–149, 2006.

[112] L. Shapira, A. Shamir, and D. Cohen-Or. Consistent mesh partitioning and skeletonisation using the shape diameter function. *Visual Computer*, 24(4):249–259, 2008.

[113] A. Sheffer. Model simplification for meshing using face clustering. *Computer-Aided Design*, 33:925–934, 2001.

[114] A. Sheffer, E. Praun, and K. Rose. Mesh parameterization methods and their applications. *Foundations and Trends in Computer Graphics and Vision*, 2(2):105–171, 2006.

[115] J. Shi and J. Malik. Normalized cuts and image segmentation. In *IEEE Conference on Computer Vision and Pattern Recognition*, pages 731–737, 1997.

[116] S. Shlafman, A. Tal, and S. Katz. Metamorphosis of polyhedral surfaces using decomposition. *Computer Graphics Forum*, 21(3):219–228, 2002.

[117] K. Siddiqi and B. B. Kimia. Parts of visual form: Computational aspects. *IEEE Transactions on Pattern Analysis and Machine Intelligence*, 17(3):239–251, 1995.

[118] P. Simari, E. Kalogerakis, and K. Singh. Folding meshes: Mierarchical mesh segmentation based on planar symmetry. In *Proc. Eurographics Symposium on Geometry Processing*, 2006.

[119] P. D. Simari and K. Singh. Extraction and remeshing of ellipsoidal representations from mesh data. In *Proc. Graphics Interface*, pages 161–168, 2005.

[120] J. Smola and B. Schölkopf. Sparse greedy matrix approximation for machine learning. In *Proc. 17th International Conference on Machine Learning*, pages 911–918, 2000.

[121] O. Sorkine, D. Cohen-Or, R. Goldenthal, and D. Lischinski. Bounded-distortion piecewise mesh parameterization. In *Proc. Conference on Visualization*, pages 355–362, 2002.

[122] V. Surazhsky, T. Surazhsky, D. Kirsanov, S. J. Gortler, and H. Hoppe. Fast exact and approximate geodesics on meshes. *ACM Transactions on Graphics*, 24(3):553–560, 2005.

[123] G. Taubin. A signal processing approach to fair surface design. In *ACM SIGGRAPH*, pages 351–358, 1995.

[124] C. J. Taylor, D. H. Cooper, and J. Graham. Training models of shape from sets of examples. In *Proc. British Machine Vision Conference*, pages 9–18, 1992.

[125] J. B. Tenenbaum, V. de Silva, and J. C. Langford. A global geometric framework for nonlinear dimensionality reduction. *Science*, 290(5500):2319–2323, December 2000.

[126] J. Tierny, J.-P. Vandeborre, and M. Daoudi. Topology driven 3D mesh hierarchical segmentation. In *Proc. IEEE International Conference on Shape Modeling and Applications*, pages 215–220, 2007.

[127] Z. Tu, S. Zhu, and H. Shum. Image segmentation by data driven Markov chain Monte Carlo. In *Proc. International Conference on Computer Vision*, volume 2, pages 131–138, 2001.

[128] L. M. Vaina and S. S. Zlateva. The largest convex patches: a boundary-based method for obtaining object parts. *Biological Cybernetics*, 62(3):225–236, 1990.

[129] J. Verbeek and B. Triggs. Region classification with markov field aspect models. In *Proc. IEEE Conference on Computer Vision and Pattern Recognition*, pages 1–8, 2007.

[130] R. Wang, K. Zhou, J. Snyder, X. Liu, H. Bao, Q. Peng, and B. Guo. Variational sphere set approximation for solid objects. *Visual Computer*, 22(9):612–621, 2006.

[131] Y. Weiss. Segmentation using eigenvectors: a unifying view. In *IEEE International Conference on Computer Vision*, pages 975–982, 1999.

[132] C. K. I. Williams and M. Seeger. Using the Nyström method to speed up kernel machines. In *Proc. Advances in Neural Information Processing Systems*, pages 682–688, 2001.

[133] L. R. Williams and D. W. Jacobs. Stochastic completion fields: a neural model of illusory contour shape and salience. *Neural Computation*, 9(4):837–858, 1997.

[134] J. Wu and L. Kobbelt. Structure recovery via hybrid variational surface approximation. *Computer Graphics Forum (Proc. Eurographics)*, 24(3):277–284, 2005.

[135] Y. Xiao, N. Werghi, and P. Siebert. A topological approach for segmenting human body shape. In *Proc. 12th International Conference on Image Analysis and Processing*, page 82, 2003.

[136] Y. Xu, , P. Duygulu, E. Saber, A. M. Tekalp, and F. T. Yarman-Vural. Object-based image labeling through learning by example and multi-level segmentation. *Pattern Recognition*, 36(6):1407–1423, 2003.

[137] H. Yamauchi, S. Gumhold, R. Zayer, and H.-P. Seidel. Mesh segmentation driven by Gaussian curvature. *Visual Computer*, 21(8-10):649–658, 2005.

[138] H. Yamauchi, S. Lee, Y. Lee, Y. Ohtake, A. Belyaev, and H.-P. Seidel. Feature sensitive mesh segmentation with mean shift. In *Proc. IEEE International Conference on Shape Modeling and Applications*, pages 238–245, 2005.

[139] D. Yan, Y. Liu, and W. Wang. Quadric surface extraction by variational shape approximation. In *Proc. Geometric Modeling and Processing*, pages 73–86, 2006.

[140] Z. Yan, S. Kumar, and C. C. J. Kuo. Mesh segmentation schemes for error resilient coding of 3D graphic models. *IEEE Transactions on Circuits and Systems for Video Technology*, 15:138–144, 2005.

[141] S. Yang, C.-S. Kim, and C. C. J. Kuo. A progressive view-dependent technique for interactive 3D mesh transmission. *IEEE Transactions on Circuits and Systems for Video Technology*, 14:1249–1264, 2004.

[142] C. Zahn and R. Roskies. Fourier descriptors for plane closed curves. *IEEE Transactions on Computers*, 21(3):269–281, 1972.

[143] H. Zha, X. He, C. Ding, H. Simon, and M. Gu. Spectral relaxation for k-means clustering. In *Proc. Advances in Neural Information Processing Systems*, pages 1057–1064, 2001.

[144] C. Zhang, N. Zhang, C. Li, and G. Wang. Marker-controlled perception-based mesh segmentation. In *Proc. 3rd International Conference on Image and Graphics*, pages 390–393, 2004.

[145] E. Zhang, K. Mischaikow, and G. Turk. Feature-based surface parameterization and texture mapping. *ACM Transactions on Graphics*, 24(1):1–27, 2005.

[146] Y. Zhang, J. Paik, A. Koschan, M. Abidi, and D. Gorsich. A simple and efficient algorithm for part decoposition of 3D triangulated models based on curvature analysis. In *Proc. International Conference on Image Processing*, pages 273–276, 2002.

[147] Y. Zhou and Z. Huang. Decomposing polygon meshes by means of critical points. In *Proc. Conference on Multimedia Modeling*, pages 187–195, 2004.

[148] E. Zuckerberger, A. Tal, and S. Shlafman. Polyhedral surface decomposition with applications. *Computer and Graphics*, 26:733–743, 2002.

[149] J. Zunic and P. Rosin. A new convexity measure for polygons. *IEEE Transactions on Pattern Analysis and Machine Intelligence*, 26(7):923–934, 2004.